Experimentele studie en conceptuele modellering van asymmetrische samenvloeiingen

Experimental Study and Conceptual Modelling of Asymmetrical Confluences

Stéphan Creëlle

Promotor: prof. dr. ir. T. De Mulder
Proefschrift ingediend tot het behalen van de graad van
Doctor in de ingenieurswetenschappen: bouwkunde

UNIVERSITEIT
GENT

Vakgroep Civiele Techniek
Voorzitter: prof. dr. ir. P. Troch
Faculteit Ingenieurswetenschappen en Architectuur
Academiejaar 2016 - 2017

ISBN 978-94-6355-018-5
NUR 955, 956
Wettelijk depot: D/2017/10.500/53

Examination board

Supervisor:

prof. dr. ir. Tom De Mulder

Hydraulics Laboratory
Department of Civil Engineering
Faculty of Engineering and Architecture
Ghent University
Sint-Pietersnieuwstraat 41,
B-9000 Ghent, Belgium

Voting members:

prof. dr. ir. Luc Taerwe (chairman, Ghent University, Belgium)
prof. dr. ir. Didier Bousmar (UCL, Louvain and SPW, Châtelet, Belgium)
prof. dr. ir. Bart Merci (Ghent University, Belgium)
prof. dr. ir. Emmanuel Mignot (LMFA-INSA Lyon, France)
prof. dr. ir. Peter Troch (secretary, Ghent University, Belgium)

Internal defence: 23 May 2017
Public defence: 4 July 2017

Funding

This research was funded by the Special Research fund of Ghent University (BOF).

Acknowledgements

The path to writing this manuscript has been a nice personal opportunity, and has been enriching in many different ways. Aside from the opportunity to delve into a specific subject for so long, also a lot of other challenges and experiences have made the past years a very fruitful experience. However, the most crucial part in all these years were the people around me, because without them it would not have been possible. By supporting me in all kinds of ways, they helped me to realize the research for and writing of this manuscript.

First, and foremost, I would like to thank my promotor, prof. Tom De Mulder. While it is the job and duty of every promotor to mentor and guide his researchers trough their path, you exceeded those basic duties by far. You were a mentor in so many ways, and it is with the utmost respect I thank you for guiding me and working with me during my years at the laboratory. The appreciation you showed, and the freedom you created for me to find my own way, allowed me to develop myself in so many ways. The constant input and feedback led me to reach results and learn certain skills I would never have deemed myself capable of. The discussions over lunch, coffee, or just meeting each other in the hallway created a very open and intensive collaboration, which I dare to call very unique and I greatly treasured. It also made me feel very connected with the work we did, and I hope that work can grow to be a successful story in the future. And although I like to take on challenges, and the change in environment I will experience now will certainly be a whole new experience, it is with deep regret I leave the laboratory. Thanks for everything, and I think the biggest compliment I can give you is to stress again how many things I learned over the years. Thanks, for everything.

I would also like to thank the member of my examination committee: prof. Taerwe, prof. Bousmar, prof. Merci, prof. Mignot and prof. Troch. The very open discussion during the internal defense was inspiring, and I enjoyed the amount of interaction on the topic of my manuscript. The remarks made have allowed me to improve the manuscript. I would like to express special gratitude towards prof. Mignot, for being so enthusiastic to discuss about the topic from the moment we met, and inviting me to stay at his laboratory for a month. I appreciated the very warm and open welcome, and the vigour with respect to science and research. Furthermore, I also want to specifically thank prof. Troch, for offering me the possibility to start my path at university after graduating before I had the possibility to work on the PhD funding of Prof. De Mulder.

Working in a University environment of course also a lot more colleagues should be thanked. To start, I would like to thank Laurent Schindfessel. Sharing an office, and working on very similar subjects, the amount of interaction is interweaved in the entire outcome of the work. The support and discussions of working together allowed us to start up a new line of research, which would have not been what it is today without the interaction. Furthermore, I also want to thank Lukas, Pedro and Thomas for the intensive collaboration and the many conversations, both work and non-work related. And although they left the laboratory before me, I would also like to thank Anke, Boudewijn, Dieter and Sieglien for the warm welcome when I arrived at the laboratory, the many tips and tricks, as well as the discussions over lunch or in the hallway.

Many thanks also goes out to the fixed staff of the laboratory, providing crucial support and knowhow about the laboratory, measurement equipment, administration, IT, etc. Jens and Stefaan, thanks for all the constructive brainstorming, practical help and work in the workshop. The many constructions, improvements and changes in the laboratory setups and equipment would not have been possible without your work and the interaction on what would be a good, practical solution for a certain problem. Yvan, thanks for all the support from your side on IT-related affairs, and for helping me figure out some basics in electronics, which helped me a lot in some of the projects I realized. Kathleen, thanks for all the efforts in figuring out administrative regulations, and general support during the years.

Of course, although in all those years a lot of hours were spent at University, the people around me were a great support, for which I also want to express my gratitude. The many hours spent doing sports with the water polo team, making stuff with the people from Nerdlab, and having drinks and dinners with close friends were a welcome variation in the weekly schedule. I wish to explicitly thank my parents, for raising me to be independent, and critically reflect on the world around me. For providing me with everything I needed, when I needed it. For giving me the opportunity to study, and to find my own way. I also want to thank my brother and sister, for being there when I needed them, for practical or other issues. I also want to thank my parents-in-law, for all the care and support they offered me during the years at University.

Finally, I want to thank my wife, Febe. For being there, all the time, every time. Good days, bad days, holidays and days before a paper deadline. For supporting me in the pursuit of getting my PhD, for sometimes giving in, for missing me when I was abroad, or again spending an evening behind my desk. For surviving the weeks of electronics on the kitchen table and the missed social events because I sometimes was too busy. For all the love and understanding, and the great amount of care. I cannot imagine how I would have finished this work without you, and I am forever grateful.
While my name is the only one on the cover of this manuscript, you all were instrumental to the research I performed, and the final completion of this work.

Contents

List of symbols

Symbols

α	($^\circ$)	Flow angle at the TCS
β	(-)	Momentum correction coefficient
δ	(m)	Mixing layer width
Δt	(s)	Time interval
κ	(-)	Dimensionless streamline curvature
λ	($\frac{1}{m}$)	Curvature adaption length
μ	(-)	Contraction coefficient
ν	($\frac{m^2}{s}$)	Kinematic viscosity
ϕ	(-)	Ratio of downstream corner to MCS velocity
ρ	($\frac{kg}{m^3}$)	Density
θ	$^\circ$	Geometrical confluence angle
A	(m^2)	Area
d	(m)	Distance of the upstream corner
Fr	(-)	Froude number
g	($\frac{m}{s^2}$)	Gravitational acceleration
h	(m)	Water depth
h_c	(m)	Critical water depth
H	(m)	Energy head
L_s	(m)	Length of the separation zone
L_{W_s}	(m)	Length to maximum width of separation zone
M	(N)	Momentum flux term
N	(m)	Distance from the central streamline along the normal
P	(N)	Pressure force
q	(-)	Flow ratio ($\frac{Q_{TUS}}{Q_{MUS}}$)

Q	$(\frac{m^3}{s})$	Flow rate
$\mathbb{R}$	(m)	Hydraulic radius
R	(m)	Radius of curvature of the streamlines
Re	(-)	Reynolds number
S	(m)	Streamline distance
u, v	$(\frac{m}{s})$	(local) velocity
U, V	$(\frac{m}{s})$	Section averaged velocity
W	(m)	Channel width
W_s	(m)	Width of the separation zone
x, y	(m)	Cartesian axis frame coordinates
Y	(-)	Ratio of up to downstream water depth

Acronyms

ADV	Accoustic Doppler Velocitymeter
CHZ	Confluence Hydrodynamic Zone
LES	Large Eddy Simulation
$LSPIV$	Large Scale Particle Image Velocimetry
MCS	Main channel most-Contracted Section
MDS	Main channel Downstream Section
MIW	Main channel Inner Wall
MM	Mixing layer at Main channel side
MOW	Main channel Outer Wall
MS	Mixing layer of the Separation zone
MSS	Main channel Separation Section
MT	Mixing layer at Tributary side
MUS	Main channel Upstream Section
PIV	Particle Image Velocimetry
$(S)PTV$	(Surface) Particle Tracking Velocimetry
$RANS$	Reynolds-Averaged Navier Stokes
TCS	Tributary Confluence Section
TDS	Tributary Downstream Section
TIW	Tributary Inner Wall
TOW	Tributary Outer Wall

Abstract

The watercourse network is one of the vital functions of the planet. The network takes care of the conveyance of water towards the seas, transports substantial amounts of sediments, and fulfils crucial ecological and economical functions. One of the important elements of this network are the confluences where two streams meet. By the technological advancements, the possibility to engineer these junctions, some control can be exerted over how the confluence fulfils some of the functions in the network. However, this requires insight in how different interventions influence the confluence flow, and engineering formulations to calculate the effects.

The main objectives of this work are twofold. First, to advance the state-of-the-art insights, experiments are performed to quantify the important hydrodynamic features at the confluence (separation zone, stagnation zone, mixing layers). Second, these experiments are used to present a new conceptual model, and an analytical low-dimensional engineering model for network calculations.

The experiments performed consist of two sets of measurement efforts, one of velocity measurements in an existing flume (low Froude number, 0.05), and one of water depth measurements in a purpose-built new flume (moderate Froude number, 0.37), that can be employed for this as well as future work. Both flumes have a 90° geometrical angle, concordant beds, and a schematized cross-sectional shape. Both sets of experiments are performed for a range of different ratios of tributary to total flow rate, since the literature suggests this is one of the most important influential parameters on the confluence flow.
In the existing flume, Surface Particle Tracking Velocimetry has been applied to obtain the (surface) velocity field, since the acquired velocity data should have ample resolution for a subsequent quantitative analysis of the

flow features. The application of this technique allowed to obtain high resolution data over a large domain, covering the confluence from upstream to a significant distance downstream. Once processed, the measurements provided a comprehensive data set that is available for numerical modellers, as well as for further analysis of the flow features.

Based upon the obtained (surface) velocity measurements, the different hydrodynamic features of the confluence were analysed. The main focus lies on the stagnation zone (zone of low flow velocities near the upstream confluence corner) and the separation zone (the zone of flow separation downstream of the downstream confluence corner). Subsequently, the central mixing layer (between the two incoming flows) and the separation mixing layer (between the contracted flow and the separation zone) are studied.

First the geometrical properties of the separation zone were studied. Contrary to the commonly applied technique of dye injection, the outline of the separation zone could be determined based on the high resolution velocity field. With the outlines of the separation zone available, width, length and shape index of the separation zone could be studied. While most of the results were in line with observations in the literature, some differences were observed. Most remarkably, the lengths obtained in the current work were shorter than in the literature. This should probably be attributed to the new definition of the separation zone based on the velocity fields, rather than the dye injections.

Based upon the aforementioned high resolution velocity fields, for the first time, a quantitative determination of the location of the stagnation zone around the upstream confluence corner was performed. This location was found to be highly dependent on the flow ratio, moving towards the branch with the lowest flow rate. In good agreement with predictions made from the solution of potential flow theory, the stagnation zone was found to be at the upstream corner for a case where 60 percent of the total flow rate is coming from the tributary.

Subsequently, the different mixing layers in the confluence were studied. Because the flow within the confluence zone is highly curved, the mixing layers are analysed in the natural coordinate system (Streamline and Normals to the streamlines). This allowed to calculate typical quantifying parameters associated with straight mixing layers such as the velocity

difference over the mixing layer, maximum gradient, mixing layer width etc. Analysis showed that at the upstream end, the central mixing layer actually comprises two mixing layers, one at each side of the stagnation zone. This corresponds to the so-called wake mode of the central mixing layer. Further into the confluence, one of the mixing layers disappears, and the other one continues as the central mixing layer, indicative of the mixing layer mode. This observation was done at a flow rate where normally the mixing layer mode would be expected. Findings of the current analysis show that wake mode and mixing layer mode probably co-exist, and that the relative importance depends on the flow ratio. For the highly asymmetrical confluence geometry adopted, the separation mixing layer is found to be even more pronounced than the central mixing layer. The central mixing layer quickly disappears because of the flow contraction, whereas the separation zone shows a high initial velocity difference, and is observed to persist several widths downstream.

In the new flume, a set of experiments obtaining water depths over the confluence is performed. While in the literature a lot of experiments have focussed on velocity information, water depth measurements have been mainly focussed on obtaining the backwater effects, but not on the local influence of the free surface onto the confluence flow. To this end, a new flume has been constructed, that is designed to facilitate a wide range of experimental conditions that could be tested in the future. To obtain the high accuracy measurements with a fine spatial resolution, an automated gauging needle on a traverse system has been built, that allowed fully automated measurements of the water depths in the new flume. The obtained water depths were found to be highly accurate, and because of the fine measurement detail, the importance of the local gradients of the free surface on the overall confluence hydrodynamics was illustrated. This shows that when performing numerical simulations at (moderately) high Froude numbers, sufficient attention should be given towards the model choices for the free surface.

Finally, an analytical engineering model to calculate confluence head losses (backwater effects) was conceived out of the obtained insights, and validated with data from the literature as well as the experimental data gathered in this work. By expressing the momentum balance over a control volume, the tributary momentum contribution appeared to be the key term to obtain accurate predictions of the head losses. In the case of a 90° angled confluence, the tributary momentum contribution was found

to be caused by upstream effects in the tributary, where the streamlines contract towards the downstream corner, causing a local surface depression, while a surface super-elevation (linked with the stagnation zone) is present near the upstream corner. While some empirical models existed in the literature, no theoretical model for the tributary momentum contribution was available. This model has been developed, based on modelling the velocity profiles in the tributary as a free vortex profile. By application of a reduction of flow curvature originating from the flow upstream of open channel bends, and the conservation of head and mass, the water depths in the tributary were modelled. Integration of these water depths then leads to the desired expression of the tributary momentum contribution.

Comparison with reported tributary streamlines, velocity profiles, water depths along the tributary walls and more, the model was found to accurately predict the different hydrodynamic parameters in the tributary. Application of the model for a wide array of measurements performed in different conditions and experimental flumes indicated that the obtained accuracy of the model is comparable to the accuracy of a 2D hydrodynamic model, which shows that the added value of the model to calculate backwater effects for engineering network modelling is present.

Samenvatting

Het netwerk van waterlopen en rivieren is een van de cruciale onderdelen van onze planeet. Het netwerk voert water af naar de zee, draagt grote hoeveelheden sedimenten met zich mee, en vervult cruciale ecologische en economische functies. Belangrijke onderdelen van dit netwerk zijn de samenvloeiingen, waar twee stromen elkaar ontmoeten. Door de technische vooruitgang is de mogelijkheid ontstaan om deze vorm te geven, en zo controle uit te oefenen op hoe de samenvloeiing haar verschillende functies vervult. Echter, om dit gecontroleerd te doen is inzicht nodig in hoe verschillende ingrepen de stroming beïnvloeden, en zijn er ontwerpformules nodig om effecten van een bepaalde keuze te berekenen.

In dit werk zijn er twee hoofddoelstellingen. Een eerste is om de huidige inzichten te verruimen, door experimenten uit te voeren die de belangrijke hydrodynamische kenmerken van de samenvloeiing (separatiezone, stagnatiezone, menglagen) kwantificeren. Een tweede doel is om de resultaten van deze experimenten te gebruiken om een nieuw conceptueel model en een analytisch model van lage complexiteit te ontwikkelen, om ontwerpberekeningen uit te voeren.

De experimenten bestaan uit twee sets van meetinspanningen, elk in een aparte stroomgoot. De eerste set metingen zijn snelheidsmetingen, uitgevoerd in een bestaande goot (laag getal van Froude, 0.05). De tweede set bestaat uit waterhoogtemetingen, in een nieuw-ontworpen goot (getal van Froude 0.37). Hoewel deze goot werd gebouwd voor de huidige metingen is bij het ontwerp rekening gehouden om een breed gamma aan onderzoeksmogelijkheden te faciliteren. Beide goten hebben een geometrische hoek van 90 graden, hebben een gelijk horizontaal bodempeil, en een schematische dwarsdoorsnede. Voor beide sets werd een brede range aan verhoudingen van debiet uit de zijtak tot totaal debiet getest, aangezien dit in de literatuur beschreven is als een van de meest invloedrijke parameters voor de stroming in de samenvloeiing. In de bestaande goot is *Surface*

Particle Tracking Velocimetry (Snelheidsmetingen a.d.h.v. deeltjes op het oppervlak) toegepast om de (oppervlakte-) snelheidsdata te verzamelen. Door de toepassing van deze techniek konden data met voldoende resolutie en nauwkeurigheid bekomen worden over een groot meetdomein (van opwaarts van de samenvloeiing tot een significante afstand afwaarts), om zo een kwantitatieve analyse toe te laten. Na de verwerking resulteerden de metingen in een uitgebreide dataset, die kan worden gebruikt voor de validatie van numerieke modellering, alsook voor de verdere analyse van de stromingsdynamica.

Startende van de oppervlaktesnelheden, worden de verschillende hydrodynamische kenmerken van de samenvloeiing geanalyseerd. Hierin ligt de focus hoofdzakelijk op de stagnatiezone (zone van lage snelheden nabij de opwaartse hoek) en de separatiezone (zone van loslatende stroming afwaarts van de afwaartse hoek). Ook de centrale menglaag (tussen de inkomende stromingen) en de menglaag van de separatiezone (tussen de gecontracteerde stroming en de separatiezone) worden bestudeerd.

De eerste analyse betreft de studie van de geometrische eigenschappen van de separatiezone. Hierbij wordt niet de conventionele techniek van kleurstofinjecties gebruikt, maar wordt de separatiezone bepaald aan de hand van hoge-resolutie snelheidsvelden. Eens de separatiezone is gekwantificeerd kunnen de (maximale) breedte, lengte en vormindex van de separatie zone worden bestudeerd. Hoewel de meeste resultaten van deze analyse overeenkomen met eerdere observaties in de literatuur, zijn er ook enkele verschillen. Het grootste verschil is dat de lengtes die volgen uit de huidige analyse korter zijn dan deze gerapporteerd in de literatuur. Dit kan waarschijnlijk worden verklaard door de nieuwe definitie van de separatiezone gebaseerd op de snelheidsvelden, i.p.v. aan de hand van kleurstofinjecties.

Op basis van de eerdergenoemde snelheidsvelden kan er ook, voor de eerste keer, een kwantitatieve analyse gebeuren van de locatie van de stagnatiezone rond de opwaartse hoek. Deze locatie blijkt sterk afhankelijk van de verhouding van de inkomende debieten, en verplaatst zich naar de tak met het lagere debiet. In goede overeenkomst met de voorspellingen a.d.h.v. potentiaalstroming blijkt de stagnatiezone op de opwaartse hoek te liggen voor een geval waarbij 60 procent van het debiet van de zijtak komt.

Vervolgens worden de menglagen bestudeerd, die sterk gekromd zijn binnen de samenvloeiing. Voor de eenvoud van de analyse gebeurt deze in een natuurlijk coördinatensysteem (bestaand uit Stroomlijnen en Normalen t.o.v. de stroomlijnen). Dit laat toe om de conventionele pa-

rameters geassocieerd met rechte menglagen (zoals snelheidsverschil over de menglaag, maximale snelheidsgradiënt, breedte van de menglaag) te berekenen in de sterk gekromde stroming in de samenvloeiing. Aan de opwaartse kant van de centrale menglaag wordt waargenomen dat deze eigenlijk uit twee menglagen bestaat, een aan elke zijde van de stagnatiezone. Dit komt overeen met de zog-mode van de centrale menglaag. Verderop, verdwijnt een van beide menglagen en gaat de andere verder, wat overeenkomt met de menglaag-mode. Dit gedrag is geobserveerd voor een geval waarin de zog-mode niet zou worden verwacht op basis van de literatuur. Dit toont aan dat de zog-mode en menglaag-mode samen bestaan, en dat het het relatieve belang is dat afhangt van de verhouding van de inkomende debieten. Voor de asymmetrische geometrie in de huidige studie is de menglaag van de separatie zone echter veel meer uitgesproken dan de centrale menglaag. Verder blijkt de centrale menglaag vrij snel te verdwijnen vanwege de contractie van de stroomlijnen, terwijl de menglaag van de separatiezone een hoog initieel snelheidsverschil vertoont, en over een grote afstand naar afwaarts blijft bestaan.

In de nieuwe goot wordt een set van waterhoogtes gemeten. Terwijl in de literatuur een grote hoeveelheid aan snelheidsmetingen beschikbaar is, beperkten de waterhoogtemetingen zich vaak tot het opmeten van de opstuwing over de samenvloeiing. Om deze metingen uit te voeren in de best mogelijke omstandigheden, is de nieuwe goot gebouwd, die zowel de huidige metingen toelaat, alsook vele verschillende experimentele condities in de toekomst. Om de hoge resolutie metingen met hoge nauwkeurigheid te kunnen verzamelen, is een geautomatiseerde meetnaald ontwikkeld, die door de plaatsing op een aangedreven meetframe volledig autonoom de waterdieptes kan opmeten. Validatie van het meetsysteem toont aan dat de beoogde nauwkeurigheid gehaald kan worden, en daardoor ook de fijne details van het vrij oppervlak kunnen worden opgemeten. Analyse van de resultaten toont dat bij een gemiddeld hoog getal van Froude (=0.37), het vrij oppervlak duidelijke gradiënten vertoont, en correct moet worden behandeld bij het uitvoeren van numerieke simulaties.

Uiteindelijk wordt aan de hand van de vergaarde inzichten een analytisch rekenmodel ontwikkeld voor de berekening van opstuwingseffecten die veroorzaakt worden door de samenvloeiing. A.d.h.v. een impulsbalans over een controlevolume blijkt de bijdrage van de zijtak een cruciale term in het verkrijgen van nauwkeurige voorspellingen. In het geval van een geometrische hoek van 90 graden blijkt de bijdrage van de zijtak te bestaan uit een drukverschil tussen de zijmuren van de zijtak, tengevolge van de contractie van de stroomlijnen naar de afwaartse hoek. Dit veroorza-

akt een depressie van het vrije oppervlak nabij de afwaartse hoek, en een lokale verheffing nabij de opwaartse hoek (stagnatiezone). In de literatuur zijn enkele empirische modellen beschikbaar voor de kracht veroorzaakt door dit drukverschil, maar geen theoretisch model. Startende van de modellering van de snelheidsprofielen in de zijtak aan de hand van het snelheidsprofiel van een vrije wervel, wordt een theoretisch model voor de kracht uit de zijtak ontwikkeld. Door het uitdrukken van de kromming van de stroomlijnen in de zijtak, geïnspireerd op een model uit modellering van stroming in bochten, kan het snelheidsprofiel in de zijtak worden opgesteld. Door het uitdrukken van het behoud van massa en energie in de zijtak, kunnen de waterhoogtes langs de zijmuren van de zijtak worden bekomen. Integratie van de drukverschillen gebaseerd op deze waterdieptes, levert dan de kracht uit de zijtak.

Het model wordt gevalideerd door vergelijking met stroomlijnen, snelheidsprofielen en waterdieptes, zowel uit de literatuur als uit eigen metingen. De vergelijking toont dat het theoretisch model correct de verschillende hydrodynamische gedrag voorspelt, voor het brede bereik aan experimentele condities waarvoor data beschikbaar zijn. Vergelijking van de voorspelling door de opgestelde ontwerpformules toont dat de nauwkeurigheid van het huidige model vergelijkbaar is met deze van een 2D hydrodynamisch model. Dit toont de waarde en de kracht van de opgestelde ontwerpformules, gezien nauwkeurige resultaten kunnen worden bekomen op een reken-efficiënte manier. Dit laat ontwerpers en ingenieurs toe om deze formules toe te passen voor netwerkberekeningen.

Chapter 1

Introduction

Confluences and their role in the open channel network

The water network is one of the vital functions of the earth. Rivers, streams and brooks, as well as the more recent manmade canals form complex networks. Not only do they convey water downstream, but they are also of importance for ecology, transport, recreation and so much more. The ability to engineer waterways is a powerful tool that has been developed, but also one with great responsibilities and repercussions. One of the important components of the network are the nodes where the watercourses join, and continue together towards downstream.

These points of merging flows are confluences, governing important aspects of the flow such as flow mixing, conveyance of water downstream, steering of sediment transport etc (see figure 1.1). To be able to engineer these confluences, fundamental knowledge and understanding of the complex flow at these points is required. Only when designed from a full understanding of the flow and related processes, engineering solutions can be designed optimally. This work investigates the flow behaviour of confluences, in a well defined schematic setting, to be able to isolate certain effects of the flow from the full complexity. By focussing on some very specific aspects and deepening the understanding, it is eventually attempted to contribute to the broad function of confluences, and their role in the network.

Figure 1.1: Confluence of the Mosel and Rhine (Germany). The difference in water color (caused by difference in sediment load) visualises the (central) mixing layer between both confluent flows.

The hydrodynamic features of asymmetrical confluences

Confluences of rivers and/or canals are so abundant that they exist in all configurations imaginable. This is, however, not convenient for the fundamental study, since the full complexity of the encountered configurations is difficult to grasp. Therefore, in an attempt to reduce the degrees of freedom, in theoretical and fundamental studies of the flow of confluences, the confluence conditions are limited to a certain well known configuration. This allows to study the flow patterns in a well defined case, and facilitates the comparison of results and findings. Eventually, after studying the flow dynamics in these more schematic representations, a more profound understanding of the processes is obtained.

In this work, the confluence is chosen to have an asymmetrical geometry, i.e. the main channel is chosen to be straight, and the incoming tributary channel has a certain angle to this main channel. The confluence is chosen to have a concordant, horizontal bed. Furthermore, all the channels are chosen to have a fixed, constant width over the entire depth, and the flow is subcritical throughout. This selection of limitations is in agreement with a lot of cases studied in the literature, and allows for comparison to findings from several different studies. Specific limitations

of the conditions to this work can be found in the Methodology section below.

While studying the flow in the confluence within the restricted set of conditions outlined below greatly simplifies the analysis, the full complexity of the flow is still difficult to grasp. To tackle this problem, Best (1985) introduced a conceptual representation of the confluence flow, that consists out of several flow features. These flow features are identifiable entities within the confluence flow field, which makes it possible to study them separately. This greatly reduces the complexity of the problem, which in turn allows more in depth study of the flow features. The main idea behind this is that by studying the features in depth, and later on trying to understand the interactions of the different features within the confluence, it is possible to understand the confluence flow field in general. Therefore, to familiarize the reader with the most important flow features, a concise overview of it is given below in figure 1.2.. It is in no regard the intention to give an exhaustive overview of the rich literature on the flow features that has been published. Relevant findings from the literature are given in the appropriate chapters, when they are applicable to the subject.

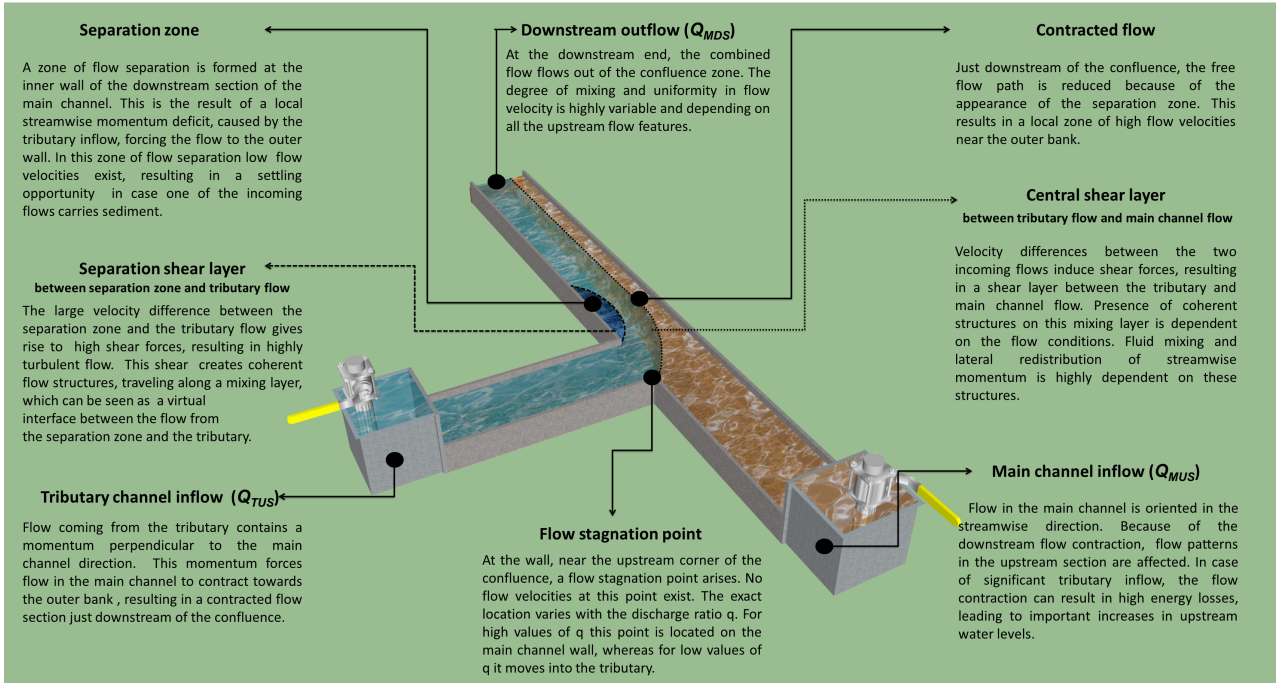

Figure 1.2: Conceptual representation of the different flow features encountered at an asymmetrical confluence (After (Best, 1985)).

Rationale and objectives

Because of the importance of confluences in the river network, a rich literature documenting the flow features identified above exists. Experimental work has been carried out, in both field and laboratory conditions. Complementary, modelling techniques have been developed, with varying degrees of complexity. Different approaches that have been applied range from very simplified, mathematical solutions based on potential flow theory to advanced numerical models using Reynolds-Averaged Navier-Stokes or Large Eddy simulations. Different research methodologies have a different (unique) set of strengths and weaknesses, and it is the combination that has lead to advancements in the state of the art.

Numerical modelling techniques have made significant advancements in the last decades, both due to intense development of the methods and the increase in computational power. Numerous numerical studies have shown the potential of such models to gain insights into the hydrodynamic behaviour of confluence flow. The strengths of numerical modelling are beneficial for a lot of studies of confluences. Since the flow is highly complex, the possibility to extract data on every grid point desired is a big advantage over experimental efforts. Furthermore, since the confluence flow is dependant on a lot of parameters, the possibility to study the confluence flow under different boundary conditions is a prerequisite for a lot of the processes. While in experimental work it is often practically impossible or prohibitively expensive to repeat tests over a large matrix of boundary conditions, numerical models offer this possibility. Finally, and possibly most important, numerical models offer the possibility of flexible, on-demand visualisations of the parameters the researcher desires. This possibility is important since visual representation offers a way to better interpret the results.

However, numerical models, as all the research methodologies, also have some weaknesses that are sometimes overlooked. While the colourful and appealing graphs, figures and animations can aid understanding, they are only useful if they can accurately represent the desired phenomena. In order to check the performance, the numerical model should be validated with reliable data from another source. Non-availability of data sets with adequate resolution and spatial coverage often results in conclusions drawn solely based on simulation results of numerical models that have been applied without adequate validation.

The **first objective** of this thesis is therefore the acquisition of several data sets of sufficient quality to serve as benchmark data sets for validation of numerical models to be validated against.

Availability of large data sets, whether it originates from numerical simulations or experimental results, does not necessarily result in advancements in understanding or knowledge creation. Evidently raw data is useful when a very specific question is at hand. This can e.g. be the question whether a certain parameter exceeds a certain threshold value for direct design purposes (e.g. a critical shear stress). Abstracting general, fundamental knowledge and insight is however different. Because of the amount of data and high complexity of the flow, it is impossible to analyse the data without simplifying it into more understandable representations. As mentioned in the previous paragraph data visualisation can be of great importance in this process. Another approach is the introduction of conceptual models. Instead of trying to grasp the hydrodynamics of the confluence completely, it is subdivided into different large scale features. These features are then interpreted as building blocks that can be studied as separate entities, but together describe the confluence hydrodynamics. This is helpful, because features can be identified and quantified, and then studied separately. The conceptual model introduced by Best (1985) is such a model, and it has been used in numerous studies since the introduction. The usage of the features introduced such as the stagnation zone and separation zone, both with their respective shear layers, has provided researchers and engineers with a nomenclature to express and discuss results. The separation zone has been qualitatively described in many publications. This mainly concerns the size and shape, and how it changes with different influencing parameters. Description of the stagnation zone and the observed shear layers is however less abundant. Although several studies describe the evolution of the location of the stagnation zone around the confluence corner, quantitative data is scarce. Study of the combined flow shear layer is widely available, but often focussed on the description of the turbulent structures and mixing. In stark contrast, the separation zone shear layer is often overlooked, while in sharp angled geometries is clearly present.
Therefore, the **second objective** is to quantify and localise the different flow features encountered in an open channel confluence. This should contribute to the understanding of the confluence flow on a conceptual level, and as such help researchers and engineers grasp the complex flow patterns.

As indicated earlier, application of three-dimensional process based numerical models for engineering purposes becomes more and more feasible. However, depending on the question at hand, the additional computational efficiency of analytical models of reduced complexity can be preferred over highly detailed calculations. Analytical models simplify the complex hydrodynamics to a set of basic equations. This allows very efficient calculations compared to advanced numerical models, but also introduces simplifying assumptions. For a lot of the engineering questions the high degree of detail is, however, not required, and analytical models are preferred. Furthermore, the analytical models can be used in a first design stage, performing calculations over a parameter matrix. A set of well performing designs can then be selected to be modelled more intensively with detailed higher-dimensional numerical simulations.

Because of the practical importance of these analytical models, the **third objective** of this thesis is to contribute to the analytical modelling of confluence hydrodynamics.

In summary, the **objectives (O)** of this thesis are:

(O1) gather data sets for the validation of state-of-the-art numerical packages and the study of confluence hydrodynamics.

(O2) provide qualitative and quantitative descriptions to advance the state of the art, deepening understanding of the different hydrodynamic flow features identified in conceptual confluence models.

(O3) contribute to the analytical modelling of confluence hydrodynamics with simplified models for computationally efficient engineering models.

Methodology

Experimental methodology

In this section, the applied methodology to reach the outlined objectives is presented. Within this thesis, the properties of the confluence conditions studied are restricted to allow fundamental research. Because the amount of influencing parameters of confluence hydrodynamics is so high, some of them are fixed to allow in-depth analysis. While this facilitates the research into specific properties of the flow, the introduction of these choices should be considered well throughout the work and when generalising results. Some scale effects or changes of e.g. the width-to-depth ratio can have effects on the flow field, and potentially influence the results, by changes in the secondary flow structures for example. If well considered, these limitations are not a problem, as long as they are clearly defined and considered in the interpretation of the results. For this study, the adopted choices are outlined below.

The geometry of the confluence is limited to 90° angled asymmetrical planforms with sharp corners. While confluences with widely varying confluence angles are found in real life situations, a case with a 90° angle is interesting because of the very high lateral disturbance of the incoming tributary flow. Furthermore, the confluence is chosen to have a fixed bed and a schematized cross-sectional shape. The bed elevation of the entire confluence is chosen to be horizontal. These geometrical constraints in the methodology allow a thorough study by limiting the amount of variable parameters. Without these constraints, the variability in conditions is so high that it hinders fundamental insight. In the literature it is however well known that geometrical conditions also greatly affect the confluence hydrodynamics. Therefore, when interpreting the results of the current work in other geometries, the effects of the changes in geometry should be considered.

To obtain the required data set for numerical model validation **(O1)** and analysis and quantification of the different flow features **(O2)**, several experiments are performed.
A first set of experiments is performed in an existing flume, to obtain velocity data sets. To be of adequate use for model validation, the anticipated velocity fields coverthe entire region of flow that is influenced by the presence of the confluence, from up to downstream. Since the envisioned data resolution should be comparable to numerical modelling efforts, traditional point measurements are cumbersome. Optical mea-

surement techniques such as Particle Image Velocimetry (PIV) can provide both the desired data density and time scales. In the existing flume this is, however, not possible because of the large spatial scale, and the lack of optical access. While Large Scale Surface PIV could resolve some of these issues, eventually Surface Particle Tracking Velocimetry (SPTV) is applied. Since floating particles are used, the applied boundary conditions will necessitate low Froude numbers, since it is implicitly assumed that the free surface is flat. While these SPTV measurements facilitate the acquisition of velocity measurements with a high spatial scale and resolution, they are limited to the surface. When interpreting these results one should be aware that the confluence flow also has 3D flow features, and that the flow field in the water column can differ from the one at the surface.

Analysis of the different shear layers, to meet **(O2)** is performed on the obtained time-averaged fields. Different quantities that have been introduced in the fundamental analysis of straight shear layers are slightly adapted such that they are applicable to the curved shear layers in the confluence flow. Shear layer properties such as the velocity difference over the shear layers and maximum gradients are calculated. By calculating the widths of the shear layers and their trajectories, the regions influenced by the shear layers are determined. This quantitative analysis is performed for a case with relatively high tributary flow, since this amplifies the observed features. Finally, the obtained insights are used to represent the confluence flow features in a new representation of a conceptual model, which could help to gain insight in the interaction of the different shear layers, flow contraction and expansion over the confluence area.

Complementary to the measurements of the free surface velocities, experimental measurements of the free surface are performed. Measurements of the free surface levels are of particular interest for numerical model validation. Since the treatment of the free surface in the numerical models is one of the major design choices, the acquired data could assist the modeller in choosing an appropriate treatment and evaluating the consequences of the adopted choice.

Because of practical limitations in the existing flume, a new flume is designed and constructed. Since this flume should serve future research broader than the one in this thesis, adequate attention is given towards functionality and possibilities for all kinds of experimental endeavours.

To allow adequate spatial resolution and measurement accuracy, a new measurement system is conceived and built. It consists of an electronically sampled gauging needle, mounted on a measurement frame that can move the needle to the desired sampling points. While the acquired data set is collected for **(O1)**, the results will also serve as validation data for the analytical model developed for **(O3)**, as clarified in the following paragraph.
Based on the results of the experimental measurements and the following analysis, the observed features are represented in a simplified way in an analytical model. These efforts are focussed specifically on the improvement of analytical formulations for the calculation of head losses over an open channel confluence. This is done by replacing the modelling of flow features that are currently still of empirical nature by an analytical description. While gaining accuracy, the incorporation of the analytical model also allows practitioners to better understand the processes behind the confluence head loss effects on a simplified level.

Naming conventions

To allow clear and efficient reporting, some naming conventions are introduced that will be utilized throughout the work. Within the confluence, important boundaries and sections are identified and named with a three letter abbreviation, as depicted in figure 1.3.

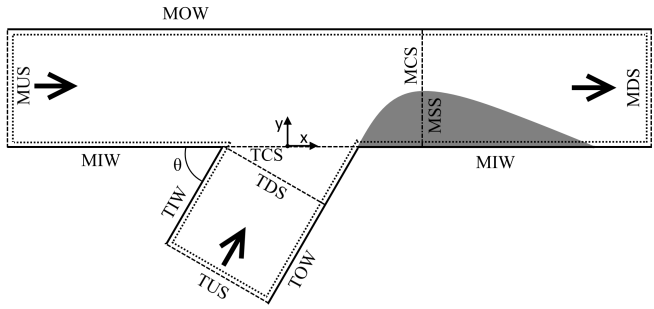

Figure 1.3: Naming convention of the different sections and walls of the confluence.

The boundaries of the confluence area are formed by the Main channel Upstream Section (MUS) and the Tributary Upstream Section (TUS) at the upstream side, and the Main channel Downstream Section (MDS) at the downstream end. The Tributary Confluence Section (TCS) is defined as the interface between the tributary and the main channel, while the Tributary Downstream Section (TDS) is defined as the most downstream cross-section perpendicular to the tributary axis. In the chosen configuration of a 90° confluence, these sections coincide, and will be referred to as the TCS. However, to be able to also discuss results in the literature that are not obtained in a 90° configuration, the naming convention is introduced to be applied where appropriate. The section of the main channel where the separation zone has its maximum width is split into two sections: the Main channel most-Contracted Section (MCS) with a width μW and the Main channel Separation Section (MSS) with a width $(1-\mu)W$, in which W denotes the channel width and μ the contraction coefficient. Lastly, the vertical boundaries of the confluence are named according to the respective channel (M or T) and whether they are at the inner (I) or outer (O) wall (W).
Throughout the work, the introduced abbreviations are used as a subscript to indicate spatially averaged values, where the subscript denotes the applicable section. The two incoming flows, with incoming discharges Q_{MUS} in the MUS and Q_{TUS} in the TUS, combine to a flow with a total discharge Q_{MDS} in the MDS. The dimensionless flow ratio q is defined as:

$$q = \frac{Q_{TUS}}{Q_{MDS}} = \frac{Q_{TUS}}{Q_{TUS} + Q_{MUS}} \tag{1.1}$$

Finally, in figure 1.3, the axis system for all general experimental results is given. The axis system is defined with a right-handed axis system, in the middle of the tributary channel at the TCS. Both the x and y axis are chosen to be positive towards downstream. This axis system is valid for all global experimental results. Only for the development of the theoretical flow model a local axis system is chosen, to obtain an x-axis that is increasing with increasing values of the local radius of curvature.

Structure of the work

Following the introduction, objectives and methodology, the outline of this work is shortly introduced.

The main body of this work is divided into four chapters (also illustrated in figure 1.4):

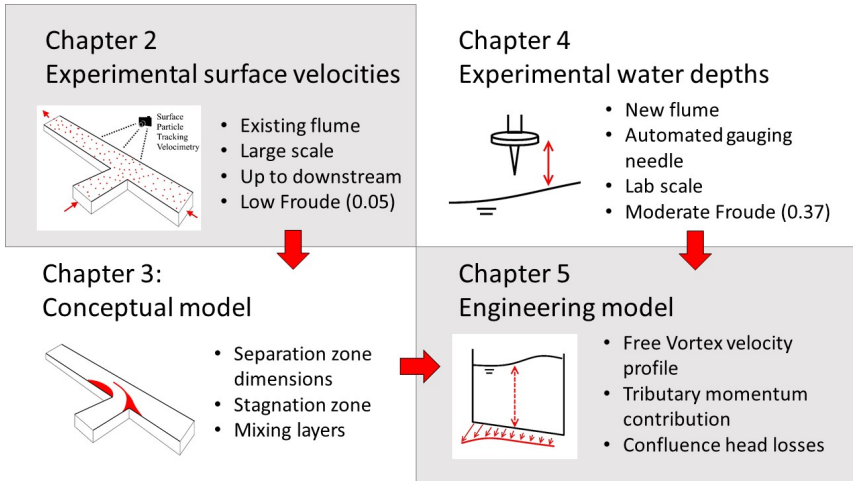

Figure 1.4: Overview of the different chapters in this work.

Chapter 2 presents an experimental investigation of the free surface velocity field of an asymmetrical confluence. After giving a concise overview of the state of the art, the specifications of the existing flume utilized to perform the experiments are outlined. An implementation of surface particle tracking velocimetry is developed and validated. Subsequently, this technique is applied over a large area for different flow ratios, and the obtained data is represented.

In **chapter 3** the surface velocity fields obtained are analysed: the different flow processes (length and width of the separation zone, stagnation zone properties etc.) are identified and where possible quantified using the experimental data. Using a representation in natural coordinates, further

in-depth analysis of the shear layers and contraction is performed.

In **chapter 4** measurements of the free surface are performed with the automated gauge, in a case with higher Froude numbers. First, the details on the newly constructed flume, and the automated level gauging system are introduced. Subsequently, after a brief overview of the importance of surface levels in confluence flow, the experimental results are represented and analysed.

With the information obtained from the experimental studies, **chapter 5** presents the development of a theoretical model of reduced complexity to describe the flow phenomena in the confluence tributary. After giving some modelling conventions and assumptions used to develop the model, a theoretical description of the velocity field in the tributary branch is set up. Utilizing the developed velocity profile, an (engineering) theoretical model for the calculation of head losses induced by an asymmetrical confluence is developed and validated on multiple data sets.

Finally, following the four main chapters, **chapter 6** provides a synthesis of the most important information enclosed within this work. To conclude, some recommendations for further work are given which, given the insights obtained within this work, might be worth investigating further.

Chapter 2

Experimental study of the free surface velocity field at an asymmetrical confluence

2.1 Experimental velocity data in the literature

To study the interaction of the different processes in the confluence hydrodynamics zone (CHZ), a lot of experimental work has been performed throughout the literature. In the light of fundamental study and theoretical modelling of the flow features, mainly water depths and velocity data have been gathered. A concise overview of the most important literature reporting experimentally obtained velocity data is given in this section.
In order to quantify the behaviour of the flow for 1D modelling, a lot of researchers performed a selection of velocity point measurements. Often, the velocity profiles at the up and downstream boundaries of the confluence were studied (Webber and Greated, 1966; Lin and Soong, 1979), as well as velocities in a section with strong flow separation (Hsu et al., 1998; Best and Reid, 1984). Also some more spatially covering efforts have been reported, as e.g. shown in Hager (1989). Since these measurements were

mainly intended for the theoretical modelling of 1D models, often section averaged velocities were measured. While this data is very applicable in theoretical modelling efforts, see also chapter 5, it is not suited for the validation of numerical models.

Complementary, a large selection of studies has performed velocity measurements at field confluences, in an attempt to grasp the (large-scale) processes of (natural) river confluences. Most of the time these studies tried to assess the influence of morphology and sedimentology on the confluence hydrodynamics. On account of velocity data, some notable studies are the multiple extensive measurement campaigns at the confluence of the Copper-Slough and Kaskaskia river(Illinois,USA), where multiple field measurement campaigns have been performed (Rhoads and Kenworthy, 1995, 1998; Rhoads and Sukhodolov, 2001, 2008; Lewis and Rhoads, 2015a,b). Also confluences of very large scales have been examined, often because the researchers were interested in the mixing behaviour of these large scale confluences, such as the studies at the Río Paraná and Río Paraguay (Corrientes,Argentina), as described in Lane et al. (2008), and of the confluence of the Negro and the Solimoes Rivers (Laraque et al., 2009) (Amazonas, Brazil). The previously mentioned works are certainly not an exhaustive overview of the numerous field studies, because the focus of the current work is on data that are applicable for the fundamental study of the hydrodynamic processes in schematized open channel confluences. However, because of the interesting observations, and the relevance of naturally shaped morphologies on confluences in general, the importance of field studies in realistic geometries should be stressed, and therefore mentioned. Some of the most important findings are that morphological effects can greatly influence the spatial heterogeneity of the flow, and that mixing processes are significantly altered.
While the above studies all contain very relevant information about the flow field at a confluence, the data sets are not very suited for the validation of detailed process-based numerical models. For this kind of validation, a more comprehensive data set is required, with highly detailed information about the confluence geometry, as well as a sufficiently dense measurement resolution of the velocity data.

To this end, some noteworthy studies have been undertaken in the literature. A first study to supply a comprehensive data set for validation of a numerical model (Biron et al., 1996), investigates the influence of a bed discordance of a 30° confluence. A selection of transects is sampled by point measurements using a Laser Doppler Anemometer. Although

the study had a small scale, it provided a data set with multiple sampled transects at different depths. However, the scale, data density and control over the inflow conditions (the tributary branch only had a very short adaptation length) render the usage of the data for the validation of numerical packages more difficult. Furthermore, the observed flow cases deviated quite a bit from the popular case of a 90° confluence with equal widths of both upstream and downstream channels used in fundamental laboratory studies. This poses less of a challenge to the numerical models, since the large lateral disturbance and heavy flow contraction are absent.
By performing an extensive measurement campaign, Weber et al. (2001) obtained a complete set of velocity measurements in a 90° large scale confluence flume. For different flow ratios, measurements were taken with an Accoustic Doppler Velocitymeter (ADV) over a selection of transects and at different depths. The resulting velocity data has been used multiple times in the literature for model validation. Several numerical models with different modelling approaches have used the data for model validation. Examples are Reynolds-Averaged Navier-Stokes (RANS) based formulation with a turbulence closure model (e.g. Dorđević (2013); Huang et al. (2002)), whereas others adopted an eddy-resolving approach, like e.g. Large Eddy Simulations, or a hybrid RANS-LES approach (e.g. Zeng and Li (2010)).
Another study that applied point measurements by ADV is described in Birjukova et al. (2014). In that study, a confluence with a tributary incoming at a 70° angle is intensively sampled, with the aim of gathering a reference data set for numerical validation. The bed in this study is concordant, but the incoming channels are not equally wide, the tributary is much smaller than the main channel (that has a constant width from up to downstream). So although some flow contraction will be present, the flow acceleration and associated separation shear layer will be much less intense when compared to 90° confluence of channels of equal widths.
While both previous studies supply a lot of data, both on time-averaged as well as turbulent quantities, the data density is still quite low to evaluate local gradients, typically associated with the central and separation shear layer. For the validation of the (more complex) numerical models this data is required to obtain a full evaluation of the model capabilities. Furthermore, this also hinders direct analysis of the experimental data for shear layers etc.
In a laboratory scale flume, (Mignot et al., 2012) performed a measurement campaign, also by application of ADV measurements. The measurements were performed for a fixed flow ratio $q = 0.5$. A selection of

transects was recorded, at three different depths : near-bed (8% of water depth), near the centre (60% of water depth) and near the surface (92% of water depth). The recorded data were presented, and successfully applied for the validation of a RANS model with k-ϵ turbulence model. Supplementary, in the same flume, Mignot et al. (2014b) measured the velocity field by application of Particle Image Velocimetry (PIV). For two flow ratios ($q = 0.33$ and $q = 0.66$) velocities were recorded in the confluence area (-0.5 < x/W < 0.5) at four different elevations (33, 42, 58 and 66% of the water depth respectively). The data were, however, not gathered with the aim of numerical model validation, but for the analysis of the central mixing layer. To this end, only the velocity field at 66% of the water depth has been presented. Furthermore, the sampling area was limited to the confluence area, and only data for two values of the flow ratio were gathered.
While the existing datasets have been successfully applied multiple times for overall evaluation of numerical model performance or flow analysis, the measurement resolution of the velocity data was not in agreement with the fine resolution of the simulations, or the spatial coverage and availability of the recorded data was not sufficient. In this chapter, the objective **(O1)** is to gather a data set of velocity data that is complementary to existing data in the literature for (numerical) model validation, by recording the surface velocities with a sufficiently high resolution to evaluate local gradients in the velocity field accurately over a large area for multiple flow ratios. The methodology to obtain those data is explained in the following sections.

2.2 Measurement methodology

2.2.1 Existing flume

The first experimental facility used in this work is referred to as the existing flume. This flume is an existing installation at the Hydraulics Laboratory of Ghent University. The flume is part of the feeding and return circuit of the laboratory, and is constructed out of concrete. The confluence angle is 90° , and has a horizontal concordant bed, and a rectangular cross section with chamfered corners. In Figure 2.1 a sketch of the facility with all the important parameters is depicted.

The cross-sectional width $W = 0.98$ m is equal in all three branches, except in the chamfered corners. These chamfers have a 45° inclination,

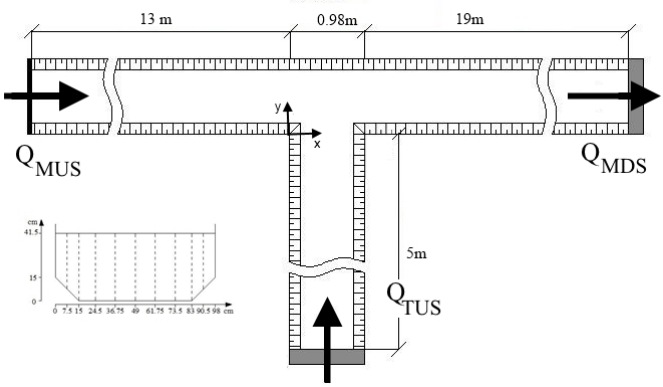

Figure 2.1: Sketch of the experimental facility with indications of Cartesian reference frame and incoming and outgoing discharge. (adapted from Schindfessel (2017))

and a width and height of 0.14 m. At the inlet, honeycomb structures ensure redistribution of the disturbed inlet flow. The inlet structures are constructed out of two perforated stainless steel plates, spaced 0.25 m apart in the stream wise direction, in the cross-sectional shape of the channel (as depicted in the insert in figure 2.1). To be able to fill the space in between, an extra plate is added to the sides to make a box,and filled with lava rock (See figure 2.2).

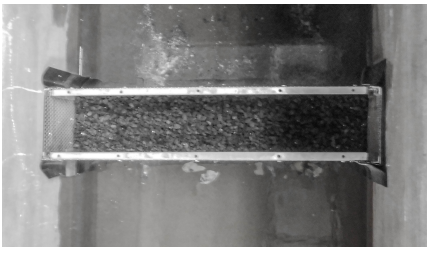

Figure 2.2: Photo of the inlet structure.

By addition of rubber strips to the side of the box, precautions are taken to ensure no leakage along the sides is occurring, and all the flow has to pass through the guidance structure. The incoming velocity profiles were checked 1.5 widths upstream of the confluence at 5 different

elevations above the flume bed. The velocity over the 4 highest elevations was found to be uniform within 2 %.
Well downstream of the confluence, a sharp-crested weir is installed to control the upstream water depths. This weir is required to gain control over the conditions applied in the test area, and to decouple the flume from the downstream pump reservoirs (in the basement of the laboratory) which are subjected to level fluctuations. The weir is constructed out of plywood, and is placed 13 m ($\approx$ 12W) downstream of the confluence zone. As with the inlet structures, also at the edges of the downstream weir rubber strips are added to ensure water tightness.

2.2.2 Surface Particle Tracking Velocimetry (SPTV)

The main objective **(O1)** of this chapter is to obtain and present a high resolution velocity field of the confluence flow. Classical point measurement, such as Acoustic Doppler Velocimetry (ADV), is thus not feasible in the current scope. Performing point measurements with adequate measurement resolution to capture all the local gradients accurately is a prohibitively large effort.

In order to characterize the flow in a confluence on a large spatial scale with high resolution, optical imaging techniques have been successfully applied, such as flow visualization (Fujita and Komura, 1989), PIV (Mignot et al., 2014b) or LSPIV (Lewis and Rhoads, 2015b; Creëlle et al., 2016). In this work, acquisition of velocity fields in the existing flume is foreseen. Because of the concrete walls of the flume, no visual access to the bulk of the flow is possible. Since visual access is required to apply laser lighting, performing regular PIV measurements in the bulk of the flow is impossible. Because of the large scale and difficult access, also workaround solutions mounting artificial lighting at the inside of the flume and looking trough the free surface are difficult. Moreover, since the flume is part of the general laboratory flow circuit, no cutting or drilling operations in the flume walls are possible. As a consequence of these limitations, optical velocimetry with floating particles is retained as the most appropriate measurement technique. This allows to mount the recording cameras above the flume looking from the top, without any issues of refraction that would be associated with looking through the free surface. Furthermore, since the particles are floating, the vertical position of the tracers is known to be fixed and equal to the free surface elevation of the flow. This eliminates the need for a light sheet to selectively illuminate the sampling area. As described by Lewis and Rhoads (2015b), obtaining

fully seeded flow over the entire confluence with floating tracers is challenging because of strong regions of up- and downwelling that might be present. When processing images with an LSPIV methodology, there are some rules on the required seeding density and uniformity. When these rules are violated, the uncertainties on the recorded velocities increase, up to the point where the recorded velocities are unreliable. Since some of the regions that will cause difficulties (separation zone, stagnation zone) are zones of interest for further analysis, precautions should be taken to obtain the best data quality possible. To this end, in this work, surface velocities are recorded with a Surface Particle Tracking Velocimetry (SPTV) technique, instead of LSPIV. Although the principle is the same, using the path of visual particles to obtain velocity data, the working principle and requirements for seeding density and uniformity are different, rendering SPTV more beneficial for the conditions encountered in the confluence flow in the existing flume.

2.2.2.1 Measurement principle of SPTV

SPTV is an optical measurement technique, using the visually tracable path of floating particles that are assumed to follow the flow to infer the velocity field. Tracer particles are seeded upstream of the flow, attempting to obtain a uniform, well seeded flow where the entire region of interest is covered with flow seeding.

In contrast to regular PTV measurements, in SPTV no light sheet is used to illuminate the plane of interest. The tracer particles applied in this study are chosen to be just light enough to float. By choosing the Froude number low enough so that no important variations exist in the free surface levels, the floating particles can be assumed to be all in a horizontal plane, that coincides with the quasi-horizontal free surface. By taking pictures at regular intervals of the moving particles on the free surface, the velocities can be inferred from the particle movement between two consecutive frames. The methodology to deduce the velocities from the obtained images is where LSPIV and (S)PTV differ:

In (LS)PIV, the velocity is calculated by cross-correlating an interrogation area between two consecutive frames taken at t_0 and $t_0 + \Delta t$. The principle is illustrated in figure 2.3. To obtain accurate solutions, the particles should be at least 1.5 times the pixel size, and enough particles should be present in the interrogation area. This is required to eliminate false correlation peaks, since it is the relative pattern of the particles that

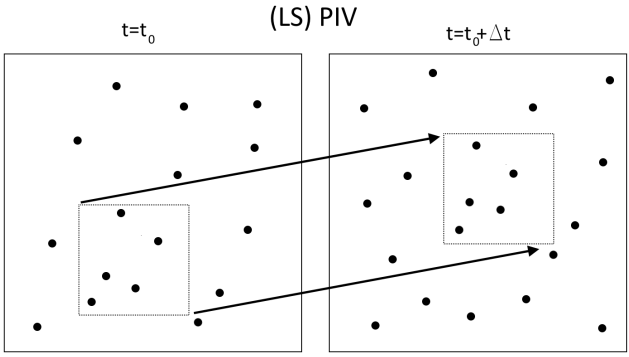

Figure 2.3: Principle of (LS)PIV tracking methodology of particles

is tracked. With increasing particle count in the interrogation area, the uniqueness of the pattern increases, and the likelyhood of obtaining correct correlation peaks is higher.

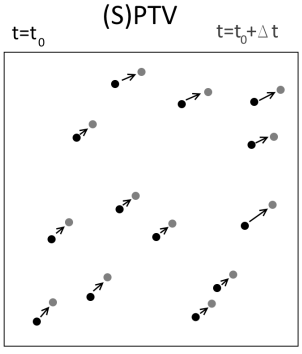

Figure 2.4: Principle of (S)PTV tracking methodology of particles

When processing the obtained images with (S)PTV, each individual particle is tracked throughout the image, as illustrated in figure 2.4. The main issue in particle tracking velocimetry is the linking of the different

observed particles throughout the different frames. The identification of each particle in the following frame is done through a tracking algorithm, that calculates a likelyhood function for each particle in the next frame. The particle with maximum likelyhood is then assumed to be the same particle as the one in the previous frame. Since individual particles are tracked, no shape or arrangement information can be used to link the particles, since they are all identical in appearance. Therefore, it is crucial that the amount of incorrect linkages between particles in different frames is as low as possible.
Particles are linked between frames by evaluation of the tracking function. The tracking function assigns a likelyhood function to each particle at the frame $t + \Delta t$, based on a prescribed set of rules. In case absolutely no information is known about the expected trajectory of the particles (e.g. a random walk is expected) a simple criterion such as shortest distance is implemented. This tracking function assumes that the particle that is observed at $t = t_0 + \Delta t$ the closest to the position of the particle at $t = t_0$ is the most probable candidate. This can result in incorrect tracking of a particle, as illustrated in figure 2.5a. Several precautions can be taken to maximize the correct particle path reconstruction:

Choose the most appropriate tracking function While the closest neighbour tracking can be appropriate for some cases, this can lead to undesired tracking results. Therefore, it is often advisable to apply a more appropriate tracking function, that incorporates some of the knowledge about the behaviour of the tracking particles. A more appropriate tracking function for fluid flows, that is still computationally feasable, is the linear movement tracking. This assumes that the velocity of the particle at $t = t_0$ is a good estimate for the average velocity over the time interval Δt. This results in a predicted location of the particles at $t = t_0 + \Delta t$. This is shown in figure 2.5b. From this predicted location, the nearest neighbour algorithm is applied again, resulting in a better overall tracking accuracy.

Eliminate candidates by expressing additional conditions In a lot of situations, certain limits or conditions can be applied to reduce the amount of potential candidates. Typical constraints that can be used are maximum velocities, limited accelerations or physical boundaries of the flow (i.e a particle can not move through a wall). This is illustrated in figure 2.5c, where by the introduction of the limitation of a solid wall, the

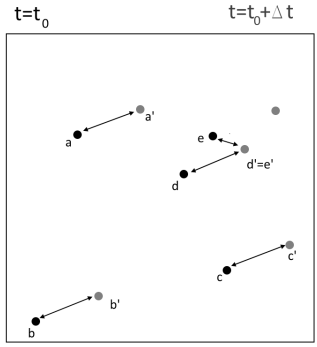

(a) Inaccurate tracking of particle e by closest neighbour

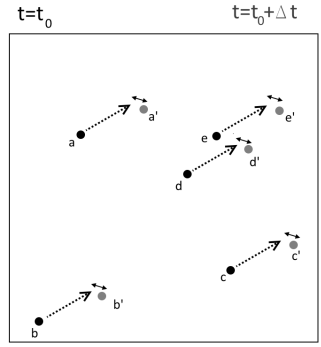

(b) Accurate tracking by linear tracking methodology

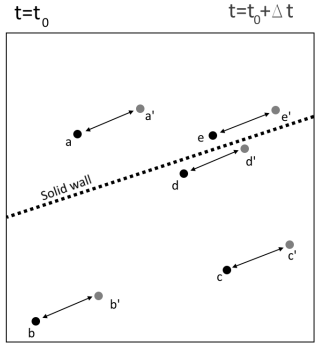

(c) Accurate tracking by physical boundary rule

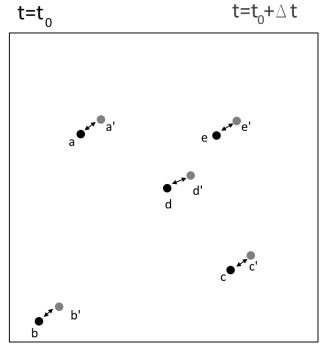

(d) Accurate tracking by reduction of time step

Figure 2.5

particle tracking becomes accurate for particle e, since it can no longer be linked to the image of particle d.

Reduce the time step between consecutive images By reducing the time step between consecutive images, the particle tracking accuracy can be further increased. This is due to a combination of two effects. The first is the increased predictive power of the applied likelyhood function.

The likelyhood function uses the last known information to predict the location of the particles in the following frame. By reducing the time step, the predictive power of the information in the last time step for the following interval is increased, and thus results in a better estimation of the predicted particle location in the following frame. The second effect is that conditions such as maximum velocity pose more strict candidate areas the shorter the time step between two frames is. This results in a reduced set of candidate particles, and thus less chances of incorrect linking. The effect of reduced time between frames is illustrated in figure 2.5d.

Reduce the amount of particles in the image By reducing the amount of particles in the image, the amount of candidates to be linked is smaller. In contrast with the requirements for LSPIV, a reduction of seeding density is beneficial for the accuracy of PTV measurements. However, reduction of the seeding density also results in less particles to observe the velocity, resulting in a reduced spatial coverage of the velocity data. So although a reduction of seeding particles increases the accuracy of the velocity data recorded, it reduces the amount of observations. Since the current study is focussed on obtaining time-averaged information, this issue can be resolved by taking a sufficiently long recording time, to obtain time averaged values. However, if a time-dependent, spatially resolved velocity field (for e.g. the analysis of turbulent structures) is aimed for, this would be an important limitation that should be carefully considered.

2.2.2.2 Practical SPTV implementation

The surface velocity data presented in this work are acquired with a 2D SPTV methodology. The entire measurement methodology with the different steps is summarised in figure 2.6.

Poly-ethylene particles (3 mm maximum diameter with elliptic shape, ρ =930 kg/m^3, shown in figure 2.7a) are manually spread upstream as a floating tracer material. Optical recording of the movement of the tracers is performed by a camera module (1920*1080 pixels) that was mounted on a horizontal frame above the flume (figure 2.7b). The camera is set to take images at a framerate of 30 frames per second (fps) during 180 seconds. For the processing, the framerate is subsampled to 10 fps, since no significant improvement in quality is observed at higher framerates, allowing for an increase in computational efficiency. In the recording setup, additional artificial lighting is applied, in order to maximize the image quality and to ensure no surface reflections caused blind spots in

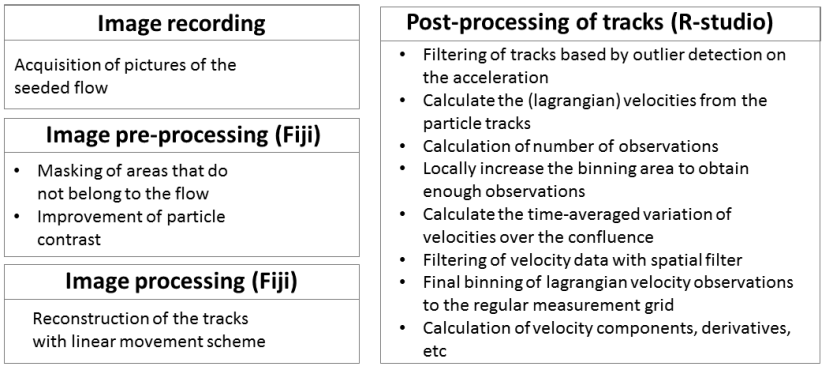

Figure 2.6: Summary of the SPTV workflow.

the recorded images. The obtained image series are first corrected for lens distortion, and pre-processed in order to maximize the contrast of the tracer particles with the background.

(a) Seeding particles for the PTV measurements.

(b) Camera mounted above the flume on the horizontal frame, looking down onto the seeding particles.

Figure 2.7

From the pre-processed image series, the particle tracks are inferred with the Fiji software (Schindelin et al., 2012), more specifically with the Trackmate plugin (Jaqaman et al., 2008). The particle tracks are reconstructed using the linear movement tracing. From the obtained particle tracks, the velocity is calculated using the particle location in the images

and the adopted frame rate. This is done with a custom coded processing methodology implemented in R-studio. The own implementation of the processing of the particle tracks allows to implement additional processing steps, that are found to increase the accuracy of the resulting data. In general, the velocity data (available at the particle locations) is binned on a grid (converting the Lagragian data to the Eulerian grid) with square cells of 2 cm ($\approx W/50$) for each time step. Cells with no observed particles are left blank, and no interpolation of the velocity data is performed.

To obtain a higher quality of the data, several post-processing steps are implemented:

- In order to eliminate remaining erroneous tracks, an outlier detection is performed on the particle acceleration. This is based on the knowledge that the acceleration of the particle in both (horizontal) directions should remain limited. This procedure removes 4% of the data, mostly due to particle mismatch within the tracking algorithm.
- For each location the standard deviation of the observed velocity data is calculated. The obtained spatial field of standard deviation is then smoothed, to reduce the effects of the standard deviation that is not necessarily time-converged. Subsequently, for each time step, the obtained velocity data is interpolated and smoothed. Finally, all of the individual velocity observations are compared to a 98 percent certainty interval with the smoothed (instantaneous) velocity and time-averaged standard deviation. This removes around 1 % of the obtained data.
- To evaluate the sampling time of 180 s, the time convergence of the measurements has been checked over the entire measurement domain. To ensure an adequate amount of samples within each cell of the grid, without having to increase the grid size over the entire confluence, the size of cells with inadequate seeding density is locally enlarged to 6 cm wide ($\approx \frac{3}{50}W$). This procedure is applied to 3% of the cells, mostly near the channel walls and in the stagnation zone.

After the post-processing of the particle tracks, the velocity time series for each cell is averaged in time, to obtain the time-averaged velocity

fields. Since the resolution of the camera utilized is insufficient to cover the entire confluence area with high-resolution recordings, the velocity acquisition is performed by the combination of multiple measurement regions. In the applied set-up, the imaged area covered the entire width of the flume, and a length of about 0.5 m. This results in on average 20 camera mounting positions (and thus 20 recordings of 180 s) per flow ratio. To obtain a single contiguous data set, regions of overlap between two adjacent recordings of about 10 cm are considered and then the overlap is removed during post-processing.

2.2.2.3 Validation of measurement technique

Since the particles are floating, regions of upwelling flow push the particles away from the location of upwelling flow. Since no particles are present in the bulk of the flow, the region does not immediately get filled with new particles. This might result in a bias, since the unavailability of particles can be related to a certain flow feature. Therefore, it is important to validate the SPTV measurements by comparison to more conventional velocity measurements. Furthermore, the premise that the particles exactly follow the flow might be invalid in some of the more turbulent regions. For regular PIV/PTV measurements, the flow tracking potential of tracer particles suspended in the bulk of the flow can be checked by evaluation of the Stokes number. However, for the floating, large particles applied in large scale surface velocimetry, this is not appropriate. As the interest is only in the average velocities, there is no need for the measurements to resolve the smallest scales of the turbulent flow. Furthermore, the pictures are only taken at 10 Hz, which also limits the temporal resolution that can be resolved. While both facts justify the application of the large, floating particles, the need for validation is clear. A final effect that is observed during the measurements is the effect of surface tension, resulting in a tendency of particles to clog together in some zones. This coalescence is undesired, since the particles do not move independently any more, and this might influence the results. Furthermore, because of the small distance between the particles correct particle tracking is more difficult, and results in reduced accuracy of the particle tracking algorithm. At first, a reduction of the capillary forces was attempted by performing a surface treatment of the particles. This was however not very efficient, and not maintained as a viable solution. Since for this study the main interest was in obtaining the time-averaged velocity field, it was chosen to seed more sparse, and in turn ensure that the velocity measurements were still

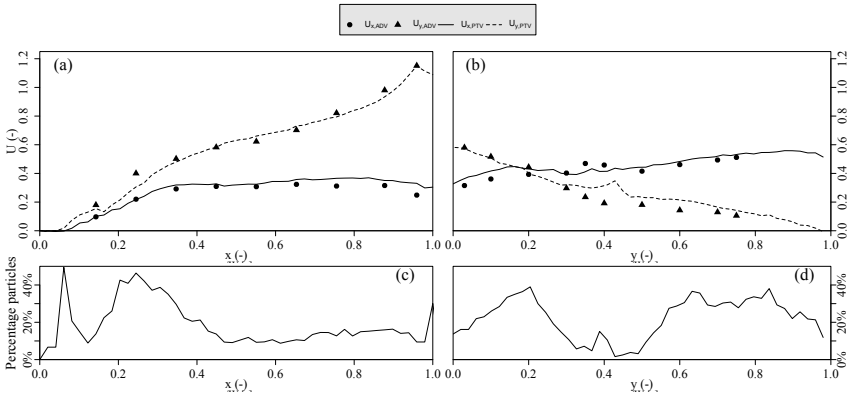

Figure 2.8: Comparison of SPTV and ADV time-averaged 2D velocity measurements and particle coverage at two cross sections y/W =0 (a,c) and x/W =0.4(b,d)

converged. The sparser seeding significantly reduced the issues of coalescence, and the validation step and check of time convergence showed that the applied methodology gives sound results.
For all of the aforementioned reasons, a validation step is required to check the performance of the measurement method. To quantify the accuracy of the SPTV measurements, comparative ADV measurements are performed with a Nortek Vectrino Profiler for $q = 0.75$. Two cross-stream profiles are sampled (at $y/W = 0$ and $x/W = 0.4$), at depths of 1 to 2 cm ($\approx 0.04h$) below the water surface, with the Vectrino profiler in a heads-up position. The resulting velocities profiles are compared in Figure 2.8. The correspondence between the ADV and SPTV measurements is reasonable, realizing that sub-surface velocities (measured with a heads-up mounted ADV) are compared to the surface velocities (measured by SPTV). Repeatability measurements for the ADV measurements gave an estimated accuracy of $\pm 0.02\ m/s$. Zones of significant differences are observed to coincide with zones of low particle counts in the SPTV measurements (percentage of the time a particle is observed in the recorded area), and therefore zones with low particle counts are locally enlarged with the earlier explained procedure.

2.2.3 Experimental flow conditions

The main objective of this chapter **(O1)** is the acquisition of an extensive, high resolution data set of surface velocities for different sets of experimental conditions. The variable under consideration that is varied between the different experimental runs is the flow ratio q. The latter has been found to be one of the major influencing parameters, increasing the disturbance by the tributary inflow with increasing values of q. By fixing the remaining parameters, the influence of changes in flow ratio are isolated, allowing a more fundamental study of the effects. The values of the flow ratio q that are studied in this chapter are $q =$ 0.25 ; 0.33 ; 0.5 ;0.66; 0.75 and 0.95.

In table 2.1 the experimental flow conditions applied in the existing flume are presented. The total discharge in the downstream section is $Q_{MDS} = 0.040\ m^3/s$, measured with electromagnetic flow meters. For this flow rate, the water level upstream of the downstream weir is $h = 0.415\ m$. With A_{MUS} the incoming cross-sectional areas in the main upstream and tributary and main downstream branches respectively, this leads to a downstream velocity of $U_{MDS} = 0.104\ m/s$. Since the downstream Froude number is low, $Fr_{MDS} = 0.05$ (-), head losses over the confluence are very small. This leads to a quasi-horizontal free surface, as required by the SPTV measurement methodology.

Table 2.1: Experimental flow conditions in the existing flume in the downstream section.

Parameter	Value	Unit
h_{MDS}	0.415	(m)
W	0.980	(m)
A_{MDS}	0.385	(m^2)
Q_{MDS}	0.040	$(\frac{m^3}{s})$
U_{MDS}	0.104	$(\frac{m}{s})$
$Re_{MDS} = \frac{U_{MDS} 4R_{MDS}}{\nu}$	98000	$(-)$
$Fr_{MDS} = \frac{U_{MDS}}{\sqrt{gA_{MDS}/W}}$	0.05	$(-)$

2.3 Results for the surface velocity fields

2.3.1 Mean velocity fields

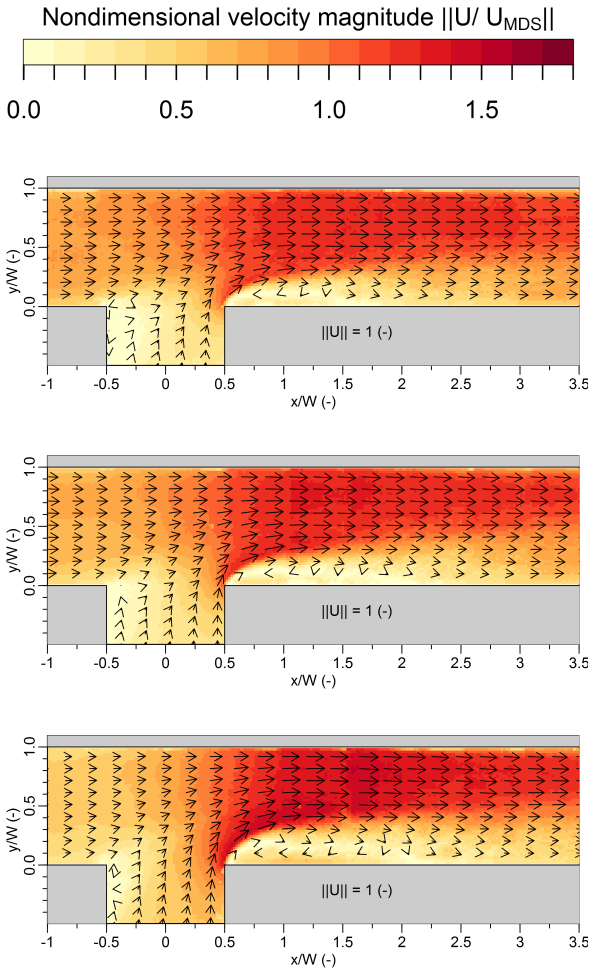

Figure 2.9: Velocity magnitude and flow direction derived from SPTV measurements for q= 0.25, 0.33 and 0.50.

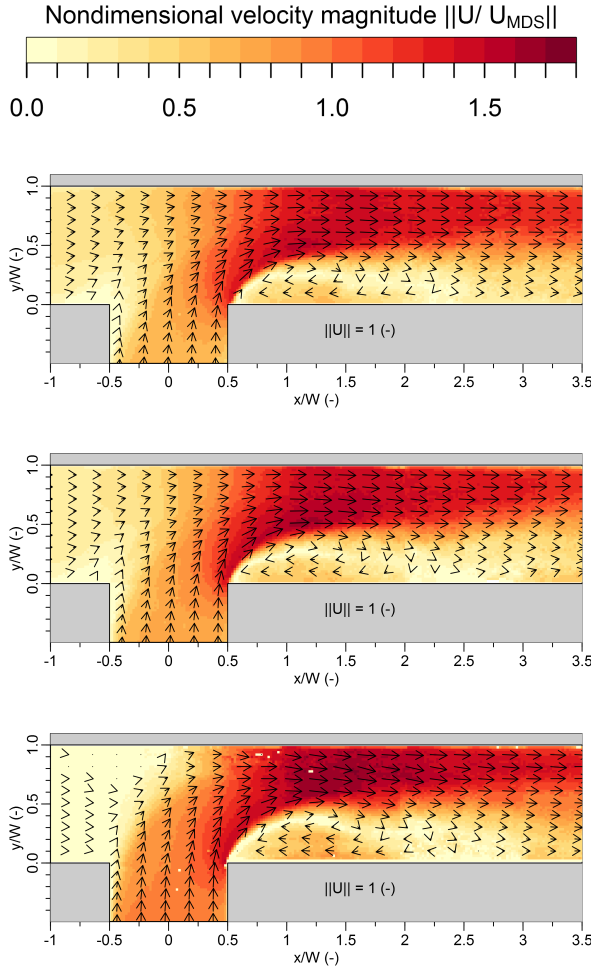

Figure 2.10: Velocity magnitude and flow direction derived from SPTV measurements for q= 0.66, 0.75 and 0.95.

The experimentally obtained time-averaged velocity fields are presented in figure 2.9 and figure 2.10 for the chosen values of the flow ratio q. The resulting velocity fields indicate that:

- The velocities upstream of the confluence are influenced by the presence of the confluence. Not only the velocity downstream of the confluence is affected, but also upstream the flow field is disturbed, especially in the tributary. The flow is clearly contracting towards the downstream corner, away from the flow stagnation zone. The heterogeneity of the flow field is found to increase with decreasing flow in the tributary (decreasing q). Upstream of the confluence in the main channel the flow is contracted towards the outer wall, but the effect is less pronounced than in the tributary.

- The location of the zone of low velocities, associated with the flow stagnation near the upstream corner clearly depends on q. For low flow from the tributary (low q) the low velocity zone is almost entirely located in the tributary. Moreover, near the inner tributary wall, flow from the main channel is intruding into the tributary, as indicated by the flow arrows pointing towards the tributary. With increasing values of q, the zone of low velocities moves more to the main channel. For very high tributary flow ($q = 0.95$) a small eddy against the outer main wall is observed around $x/W = -0.2$.

- The flow separation zone is clearly observable as zone of reduced velocities near the inner wall for $x/W > 0.5$. The high velocities of the flow coming from the tributary are clearly observed next to the low velocities of the separation zone. The associated shear layer is clearly distinguishable in all the cases.

- The flow contraction next to the separation zone clearly increases with increasing inflow from the tributary. The separation shear layer moves closer to the outer wall, indicating growth of the separation zone. This results in a stronger contraction of the downstream flow, and is observed as higher maximum velocity magnitudes in the contracted section.

- The flow is still highly heterogeneous at x/W=3.5, the most downstream represented section in the color plots. In section 6, the contour plots for the entire sampled domain are shown. At the most downstream sampled section, $x/W = 7$ there is still quite some heterogeneity of the flow field, indicating a significantly longer distance is required for the flow to evolve towards the fully developed flow profile.

2.3.2 Flow vorticity

To illustrate the location of the central and separation mixing layer, the vertical component of vorticity of the time-averaged flow field has been calculated. The obtained results are presented in figure 2.11 and figure 2.12. The zone of negative vorticity starting from the downstream corner clearly outlines the separation zone, and illustrates the widening of the separation zone with increasing values of q. In contrast to the size of the separation zone, the lowest recorded magnitudes of the vorticity are similar for all flow ratios. Near the upstream corner, the high dependency of the central mixing layer on q is illustrated by the plots of the vorticity. For low q, the mixing layer at the side of the main channel shows the highest intensity. With increase in tributary flow the vorticity magnitude starts to diminish, and for $q = 0.5$, the mixing layer at the side of the tributary becomes visible. Note that at this flow ratio, the central mixing layer actually appears as two spatially separated mixing layers, at both sides of the stagnation zone. For higher values of q the mixing layer at the tributary side becomes dominant. For $q = 0.95$ the central mixing layer protrudes a significant distance into the main channel. This goes along with the observation that almost the entire main channel is occupied by the stagnation zone, which causes the observed elevated levels of vorticity between the flow from the tributary and the very low flow velocities in the main channel.

2.3.3 Conclusion

In this chapter, the methodology and results of an experimental study to obtain a data set of comprehensive (surface) velocity fields are presented. The application of the developped Surface Particle Image Velocimetry (SPTV) technique was found to be appropriate to obtain the time-averaged velocity field at high spatial resolution in the large scale laboratory flume. Application of the technique, employing optical tracking of floating Polyethylene particles resulted in accurate measurements when compared to Acoustic Doppler Velocimetry point measurements. The application of the optical technique allowed to economically measure an extensive region of the flow, with high enough spatial resolution and accuracy to obtain a data set for numerical model validation. In total, measurements were performed from one width upstream of the confluence to seven widths downstream, for six different flow ratios. The resulting velocity fields have been presented, and are available for the validation of

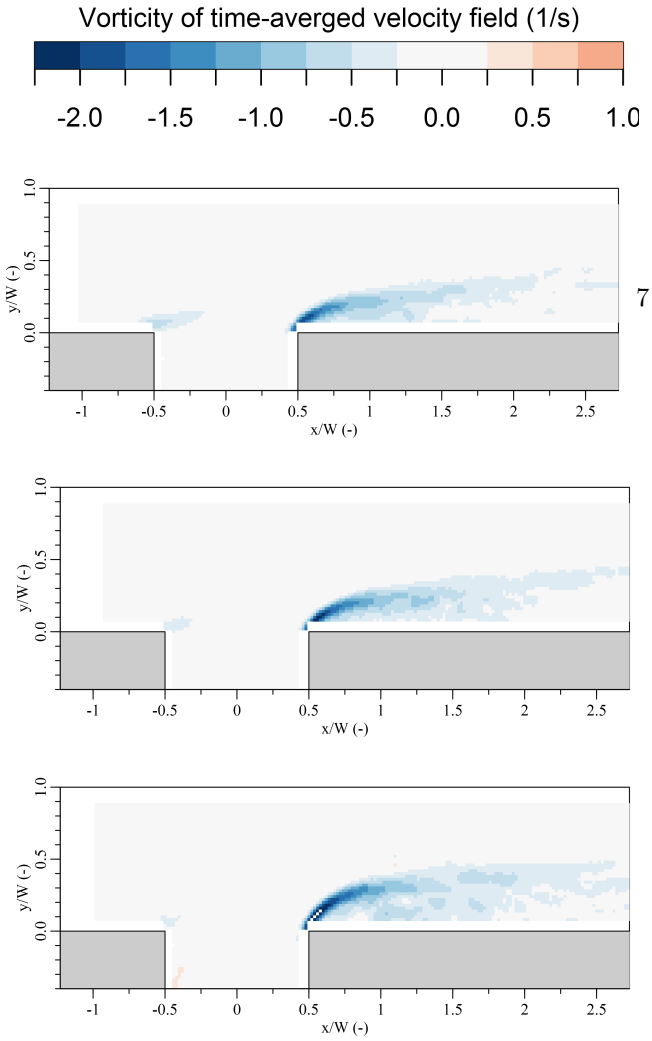

Figure 2.11: Vorticity of the velocity field derived from SPTV measurements for q= 0.25, 0.33 and 0.50.

numerical models. A first qualitative observation of the results showed that the hydrodynamic features that are typical of confluence flow are

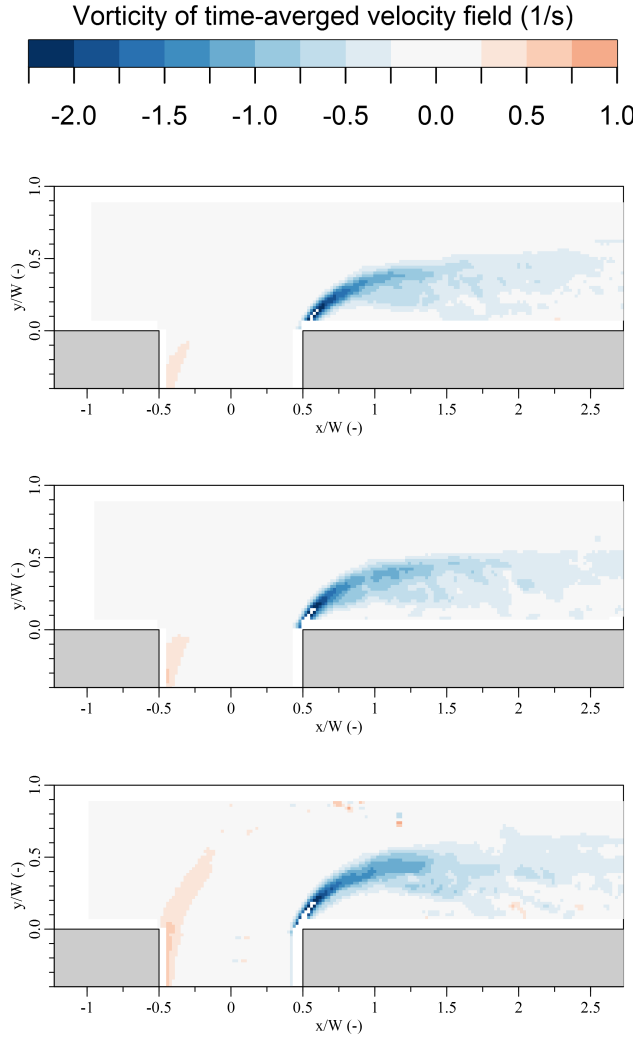

Figure 2.12: Vorticity of the velocity field derived from SPTV measurements for q= 0.66, 0.75 and 0.95.

clearly present, and that some evolution of their appearance with the flow ratio is observable. Analysis of the vorticity of the time-averaged flow

field showed that both the central and the separation zone mixing layer are clearly distinguishable in the experimental data. However, a more in depth, quantitative analysis of the data is required to acquire some more theoretical insight in the influence of the flow ratio on the confluence features. This analysis is the topic of the following chapter.

Chapter 3

Study of the free surface flow features and mixing layers

3.1 Quantification of the different hydrodynamic features of the velocity field

In this chapter the different hydrodynamic features at the confluence are studied further in depth. While the features depicted in figure 1.2 can be directly distinguished in the velocity fields presented in the previous chapter, a qualitative analysis is not enough to gain deeper insight. The encountered features follow from complex hydrodynamic processes that interact. The combined effects result in the interesting global hydrodynamic behaviour. To unravel how this interaction causes the observed features, a rigorous, quantitative analysis of the features is required.

3.1.1 Separation zone

The most apparent and regularly studied feature in confluence flow is the separation zone. While it is shown that the separation zone can be absent in field conditions with realistic morphologies (Lewis and Rhoads, 2015b), whenever it is present it has a profound impact on the hydrodynamics of the entire confluence. A geometry with a very high angle like employed in

the current study (and many other fundamental studies) is convenient for the study of the separation zone, since it has been shown this increases the separation zone length and width (Best and Reid, 1984). Geometries with schematized, sharp edges further increase the separation strength, simplifying the delineation of the separation zone.
A lot of studies in the literature employed visualisation methods (Best and Reid, 1984; Gurram et al., 1997; Hager, 1989; Hsu et al., 1998) to distinguish the separation zone. The experimental conditions cover a wide range of Froude numbers (0.25 to 1) and flow ratios (0 to 1). Coloured dye, released at the upstream corner is transported along the separating streamline, and as such delineates the separation zone.

Also the inverse methodology has been applied, applying dye to the separation zone, colouring the separation bubble, that traps most of the dye, as such directly colouring the separation zone. The presence of the curved, (intense) shear layer between the separation zone and the high velocity flow in the contracted section causes a mixing layer. The appearing turbulent structures quickly disperse the injected dye, making a sharp delineation of the separation zone difficult. An impression of this technique, applied in the new flume, is shown in figure 3.1, indicating the dispersion of the injected dye. Availability of the velocity data with adequate resolution, presented in chapter 2, allows to calculate the separation zone properties from recorded velocity data. In comparison with the visual methods this has several advantages. The most important one is that the calculation of the location of the separation zone can be performed on the high-resolution data, and that the uncertainty of the determination of the interface is significantly reduced. Second, since the velocities are recorded over a long time span, the separation zone location can be determined based on the time-averaged velocity field. This is more difficult with visualisation methods, since only by taking photographs with very long exposure times time-averaging can be done. Moreover, if long exposures are applied, a lot of care should be taken into making sure that the supply of dye is steady over the entire exposure time. The determination of the separation zone properties based on the current velocity measurements can thus be performed more objectively, and is less prone to measurement uncertainties.

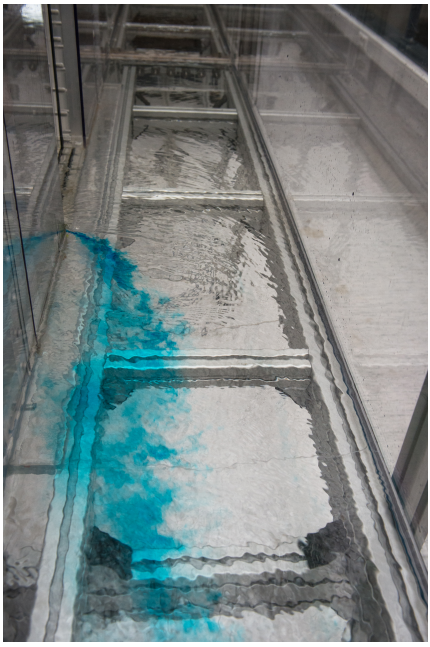

Figure 3.1: Separation zone visualised by dye injection, dispersed by the turbulent structures.

3.1.1.1 Practical procedure for delineation of the separation zone

In this work, the delineation of the separation zone from the velocity fields is performed with two different definitions **(D)**, based on two different interpretations of which quantity defines the separation zone.

(D1) Streamline definition A first methodology to find the separation zone is to calculate the streamline that passes as close as possible to the downstream confluence corner. This streamline is then assumed to be the separating streamline, and can be taken as the definition of the outline of the separation zone. Practically, the streamline is calculated starting from the point just downstream of the confluence corner. This ensures that the streamline always curves back into the separation zone. The streamline is cut at the point where the most downstream coordinate

is reached to obtain the outline of the separation zone. This is done because the selected streamline is known to be located inside the separation zone, and presents itself as a spiral within the separation zone. Since this hinders visual interpretation, and since only the outline of the separation zone is of interest for further study, the streamlines are cut at their most downstream location to prevent this inconvenience. In figure 3.2, the resulting outlines of the separation zone for different values of q are shown.

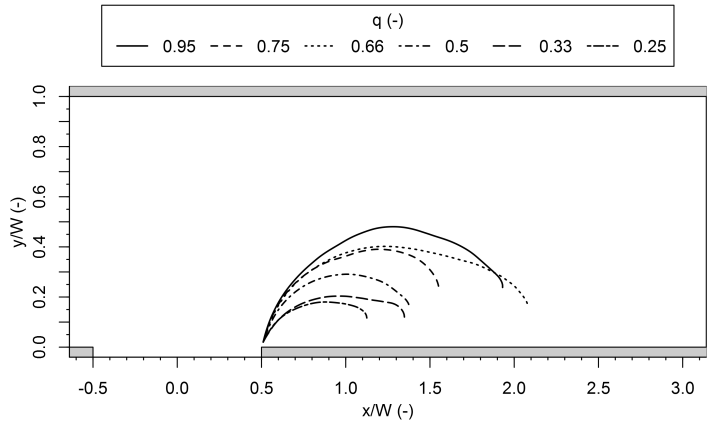

Figure 3.2: Separation zone location based on the streamline separating from the downstream corner **(D1)**.

(D2) Zero net discharge definition A second option to delineate the separation zone is to calculate the point at which there is a zero-net downstream discharge between that location and the inner confluence wall. This definition is somewhat more practical (for experimental data) than the first, for several reasons:

1. it reduces the dependency of the result on small experimental variations in the flow speeds. The calculated separating streamline as in (D1) has the disadvantage that small measurement inaccuracies of the velocities have consequences for the calculated trajectory downstream of that point,

2. the result is hindered less by difficulties to measure very close to the wall. Since the particles tend to stick to the channel walls, the uncertainty of velocities very close to the wall is higher. For the calculation of the separating streamline it is important to start as close to the downstream corner as possible,

3. with the zero net discharge method, the separation zone always has a reattachment point. This is not the case with the definition with the separating streamline.

Practically, the location of the separation zone defined by the zero net discharge method is given by all the points ($x/W \geq 0.5$, $y/W \geq 0$) that satisfy the following criterion:

$$\int_0^{y_{sep}} (x)u(x,y)dy = 0 \tag{3.1}$$

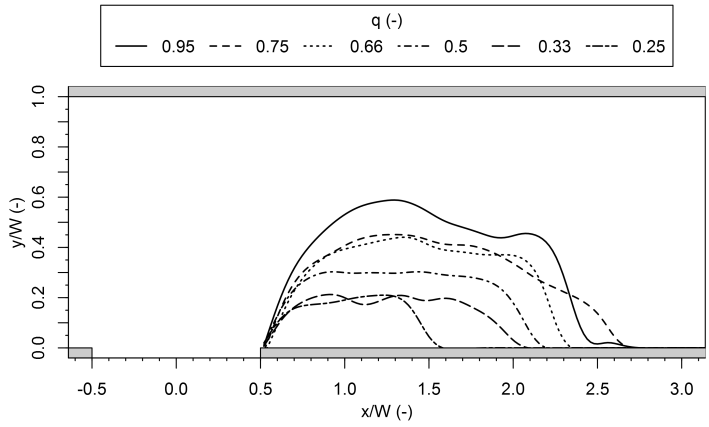

Figure 3.3: Separation zone location based on the zero net discharge method **(D2)**.

The resulting outlines of the separation zones are shown in figure 3.3.

The expected increase in separation zone dimensions is observed in the

results of both definitions. The outlines defined with the streamline definition are clearly smoother than the outlines obtained from the zero net discharge method. It is important to realize that this smoothness is not necessarily indicative of a higher accuracy. In the streamline definition, every measurement error along the path from the downstream corner is decisive for the complete outline path, but does not lead to sudden changed in the path. The location of adjacent points is highly correlated, since the streamline is calculated from one point to the other. For the zero net discharge method, the position of the outline is defined independently of adjacent points, and there is no correlation between any of the obtained points, since they are solely based on the velocities of their respective transects. However, the outline as defined by the zero net discharge method depends on all the velocities between the main channel inner wall and the separation zone outline at that transect. This also means that this leads to a dependency on the less reliable velocities near the walls, and to a more jagged separation zone outline.

3.1.1.2 Width of the separation zone

With the available velocity data and the introduced definitions (D1) and (D2), the separation zone outline with clear, well defined definitions based on experimental data is available. This more objective approach compared to the more empirical approach with dye colouring should lead to more consistency in the resulting values, and allow more rigorous evaluation of the effects of the dimensionless flow ratio on the separation zone dimensions.

In figure 3.4, the (maximum) width of the separation zone W_s is plotted, for both the streamline and zero net discharge definition. The width of the separation zone is clearly increasing with increasing values of q. Notably, the width of the separation zone at quite low values of q is already a significant portion of the total available width ($W_s/W \approx 0.2$).

The widths obtained with both methods are very comparable. For low flow rates almost equal values are obtained, while for higher flow rates the zero net discharge method delivers slightly higher widths. Both experimental data sets are compared with the empirical models for the separation zone width by Gurram et al. (1997) and Best and Reid (1984). Over the entire range of q, the model of Best and Reid (1984) results in the best predictions, with no clear trend in the observed discrepancies between the model and the experimental data. In contrast, the model by Gurram et al. (1997) gives a (slight) overestimation of the separation zone widths.

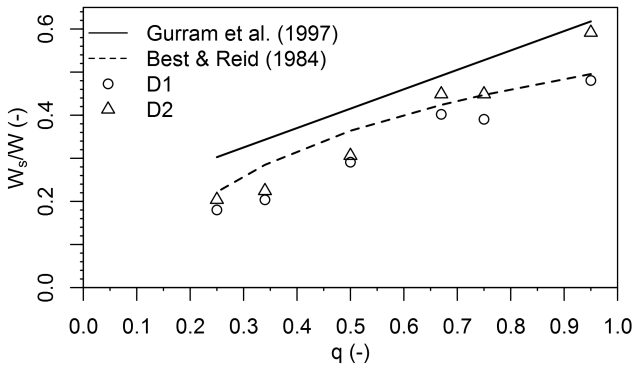

Figure 3.4: Maximum width of the separation zone at the free surface. Circles represent the values based on the separating streamline definition, triangles show values obtained from the zero net discharge method.

The better agreement of the current data with the empirical model by Best and Reid (1984) could potentially be caused by the Fr numbers for which the models were derived. Downstream Froude numbers were in the range [0.1,0.3] for the measurements by Best and Reid (1984), which are quite low, as is the case for the current experiments. The model by Gurram et al. (1997) was derived for a range of Fr of [0.25,1], which is a significantly higher and wider range, and thus might cause the difference in agreement.

3.1.1.3 Length of the separation zone

Complementary to the width of the separation zone, also the length of the separation zone L_s is defined. Whenever the separation zone is found to reattach to the inner confluence wall, L_s is defined as the distance between the downstream corner and the point of reattachment. However, when defining the separation zone with the streamline definition, no reattachment is found (see figure 3.2). For these cases the length of the separation zone is defined as the downstream distance between the downstream confluence corner and the location where the separating streamlines reaches the most downstream coordinate.

In figure 3.5 the obtained lengths of the separation zone have been represented.

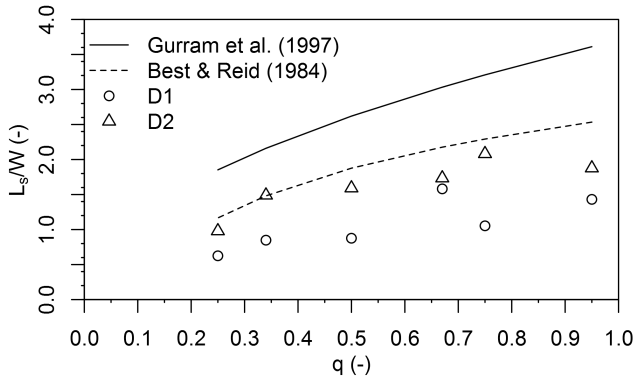

Figure 3.5: Length L_s of the separation zone at the free surface. Circles indicate lengths defined from the streamline definition. Triangles represent values obtained from the zero-net discharge method.

The recorded lengths of the separation zone show quite a large spread. This is due to a combination of the high sensitivity of the reattachment point to small variations in the flow, as well as the difficulty in defining the reattachment point from the obtained data. The lengths found in the current study are however clearly lower than the results from previous studies. The introduction of two different ways to define the location of the separation zone, as well as a dual definition for the length, depending if a reattachment point was found or not, makes the data hard to compare. This reduces the usefulness of a quantitative analysis. In contrast, the maximum width of the separation zone is always clearly defined, and the longitudinal coordinate where the maximum width is encountered is defined more clearly. Therefore, a new parameter is introduced, that also defines a length scale of the separation zone, but without the difficulties of the total length definition.
The length to maximum width L_{W_s} is defined as the distance between the downstream corner and the x-location where the separation zone reaches maximum width.

For both (D1) and (D2) the newly introduced length to maximum width, represented in figure 3.6, gives more consequent results, and a slightly lower experimental spread is observed. Moreover, the values of both definitions are nearly identical (within the experimental spread). This is in contrast with the total length, that gave significantly higher

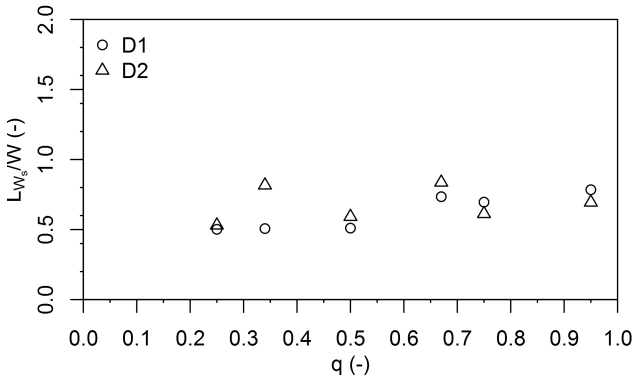

Figure 3.6: Length to maximum width L_{W_s} of the separation zone. Circles indicate lengths defined from the streamline definition. Triangles represent values obtained from the zero net discharge method.

values of the length for the zero discharge definition. L_{W_s} is found to be almost constant with respect to the flow ratio. Only a very mild increase in L_{W_s} with q is observed. This means that although the width of the separation zone is very sensitive to the flow ratio, the downstream location where this maximum width is obtained is quasi constant.

3.1.1.4 Shape index of the separation zone

The shape index of the separation zone was introduced in Best and Reid (1984) as the ratio of separation zone width to length. In figure 3.7 the shape index based on both L_s and L_{W_s} are shown. To obtain more comparable results, the shape index based on L_{W_s} is taken to be $W_s/(2L_{W_s})$. Both definitions result in higher values of the shape index than predicted by the emperical formulae, mainly caused by the shorter lengths than predicted by the models from literature. This might be caused by the relatively deep water conditions in the experiments, combined with the presence of the chamfered corners of the flume. Both effects can promote a stronger 3D flow, that could cause a quicker dissolution of the separation zone.

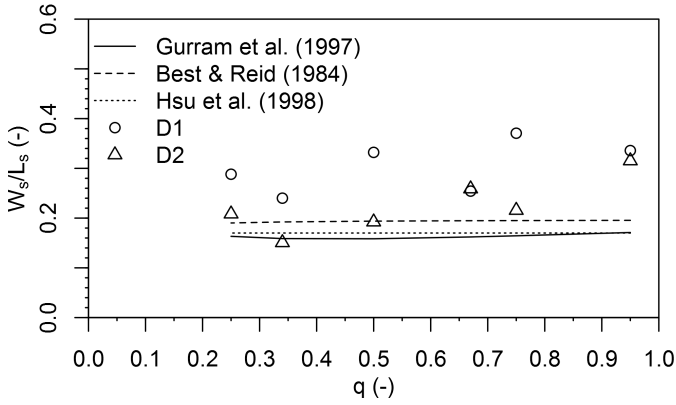

(a)

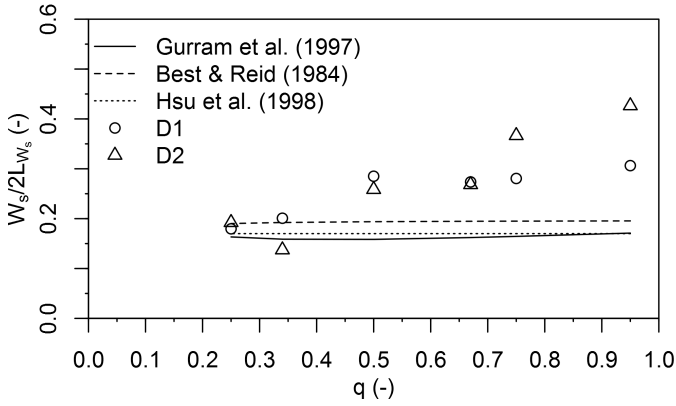

(b)

Figure 3.7: Shape index of the separation zone. Circles indicate lengths defined from the streamline definition. Triangles represent values obtained from the zero net discharge method. Values in (a) are calulated based on the total length, in (b) on the length to maximum width.

3.1.1.5 Most contracted section

Because of the flow separation, the flow can not utilize the entire width of the flume in the region immediately downstream of the downstream confluence corner. Therefore, since the same total discharge has to pass, the flow is contracted and the velocities are (locally) increased. At the point where the separation zone reaches its maximum width, the available section for flow in the downstream direction is the smallest, and the highest degree of flow contraction is reached. This is expressed with the contraction coefficient μ, that is defined as the ratio of the width of the minimal available section to the channel width. This ratio is directly linked to the maximum width of the separation zone, and can be defined as:

$$\mu = \frac{W - W_s}{W} \tag{3.2}$$

With the calculated values of the contraction coefficient, the average velocity in the contracted section can be calculated as:

$$U_{MCS,\mu} = \frac{Q_{MDS}}{h\mu W} \tag{3.3}$$

However, the surface velocity field is not necessarily equal to the depth averaged flow field. With the width of the separation zone W_s and the available velocity fields, the average surface velocity in the contracted section can be calculated:

$$U_{MCS,vel} = \frac{1}{W - W_s} \int_{W_s}^{W} u(x_{MCS}, y)dy \tag{3.4}$$

In figure 3.8 the average velocities in the contracted section are compared, calculated with the different methodologies. The accelerated flow speeds in the contracted section are increasing with increasing values with q. Observations of Weber et al. (2001) indicated that the separation zone is wider near the surface than the depth averaged width, a conclusion that is supported by the current findings. This is clearly visualized by the substiantially higher values of $U_{MCS,\mu}$ compared to $U_{MCS,vel}$.

3.1.2 Stagnation zone

Within the confluence, a second zone of locally reduced velocities is present. The stagnation zone is a region of the confluence flow between the incom-

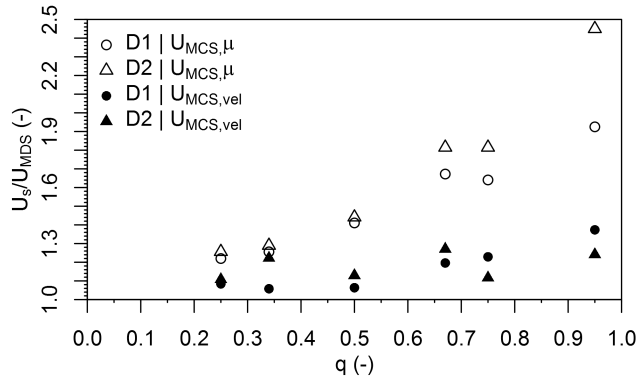

Figure 3.8: Average velocity in the contracted section as a function of the discharge ratio q. Circles indicate lengths defined from the streamline definition. Triangles represent values obtained from the zero-net discharge method. Empty symbols represent values calculated based on the contraction coefficient ($U_{MCS,\mu}$), filled symbols represent values calculated from the velocity field ($U_{MCS,vel}$).

ing flows, encountered more upstream in the CHZ, in the vicinity of the upstream confluence corner. As illustrated with solutions of the potential flow in a confluence by Modi et al. (1981) and Webber and Greated (1966) it is caused by the streamlines that curve away from the upstream confluence corner. This causes a zone of local reduction in flow velocities, and eventually flow stagnation.

3.1.2.1 Location of the stagnation point

While the presence of the stagnation zone is often recognized and deemed important for the confluence hydrodynamic behaviour (see e.g. Rhoads and Sukhodolov (2008) for an extensive description of the effects of the stagnation zone on the (turbulent) flow properties in the CHZ), quantitative information is scarce. Based on the velocity data presented in chapter 2, the location of the stagnation point is derived. Theoretically, in the flow stagnation point a streamline originates from the channel wall near the confluence corner for changing values of q. Theoretical derivations (Webber and Greated, 1966; Modi et al., 1981) show that the flow stagnation point moves around the confluence corner. The geometrical

constraints of the confluence influence the location of the stagnation point. Unambiguously locating this point in the experimental data is however not straightforward.
As explained in section 2.2, the velocity measurements with the applied SPTV technique have a lower accuracy in zones of low flow velocities, because of difficulties in maintaining ideal seeding conditions during the entire sampling period. Therefore, it is important that the working definition to determine the stagnation points is not too sensitive to small measurement variations. Therefore, the following methodology is applied to locate the stagnation point based on the experimental data:

1. define a threshold velocity that corresponds to flow stagnation,
2. apply the threshold to the velocity field, resulting in a zone where velocities are lower than the defined threshold,
3. calculate the area of the resulting zone ($A_{stagnation}$),
4. for each point along the inner channel walls with $x/W < 0$, define the circle section that has the same area as $A_{stagnation}$, excluding surface area that is not part of the confluence (i.e. wall surface is excluded),
5. for each point along the channel walls, integrate the (non-thresholded) velocity data over the circle section,
6. find the point along the channel walls with the lowest value of the defined quantity.

Following the methodology above, the location of the stagnation point can be defined for a chosen value of the threshold velocity. The adopted velocity should always be (substantially) lower than the minimum of the two incoming velocities, since higher values would lead to entire parts of one of either upstream channels to be indicated as part of the stagnation zone, which is clearly undesired. For the current calculations, a value of 10 % of the main channel velocity for q=0.95 is adopted.
The resulting location of the stagnation point is expressed with the distance to the upstream confluence corner (d) defined as indicated in figure 3.9a. In figure 3.9b the location of the stagnation point as a function of the flow ratio is plotted.

As expected from the theoretical derivations, the stagnation point moves (significantly) around the upstream corner. For low flow ratios,

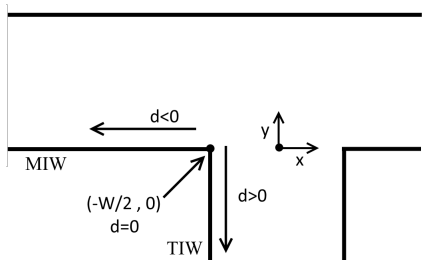

(a) Definition of the distance to the upstream corner.

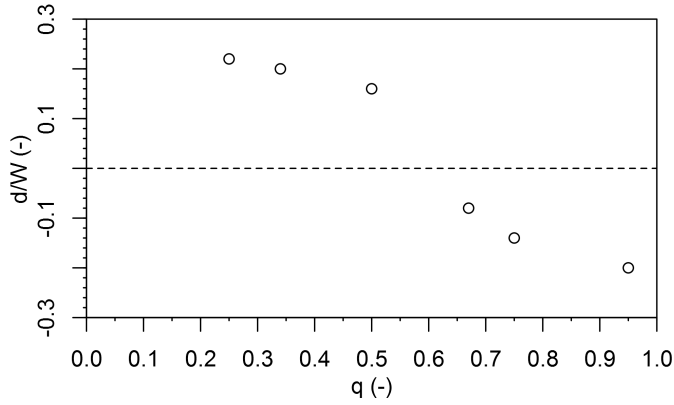

(b) Location of the stagnation point.

Figure 3.9: Evolution of the stagnation point along the confluence inner walls with the flow ratio q.

the stagnation zone is found in the tributary, whereas for high flow ratios in the main channel. In both cases, the stagnation point is found as far as 0.25 W in the respective channels, indicating a significant disturbance in the upstream channels is present. Notably, the shift of the stagnation point from the tributary to the main channel does not occur at q=0.5, as would be the case in a parallel symmetrical confluence. Instead, because of the strong influence of the high (90°) angle, the stagnation point is estimated to be on the upstream corner for $q = 0.6$. This is in very strong agreement with the theoretical value obtained from the potential flow solution of (Modi et al., 1981). The other values of $d/W = -0.37$

for $q = 0,2$ and $d/W = -0.13$ for $q = 0.8$ respectively, however, seem to differ quite significantly from the currently obtained results.

3.2 Study of the confluence mixing layers

Within the asymmetrical confluence, two important mixing layers exist: the central mixing layer, in between the incoming flows from main and tributary channel, and the separation mixing layer, between the contracted flow and the separation zone. Both the mixing layers are highly curved into the main channel, making the analysis of the mixing layers less practical. In the study of the central mixing layer in Mignot et al. (2014b) this issue was solved by the study of the mixing layer in natural coordinates. Based on PIV measurements in the confluence zone, the set of streamlines and normals was calculated. To obtain a global coordinate system, the central streamline (assumed to start at the upstream confluence corner) was chosen as the reference for a global coordinate system. This allowed the study of the central mixing layer in the confluence, while still being able to calculate the classical quantities such as velocity difference, maximum gradient and width of the mixing layer. Mignot et al. (2014b) found that the complex curved and contracting flow in the confluence has a significant impact on the evolution of the velocity profiles along the mixing layer, and that the models of the straight mixing layers are not directly transferable to the (central) mixing layer in the confluence. In the analysis, it was noted that the normals could often not be calculated fully, by lack of data in the upstream and downstream parts of the confluence. Furthermore, as described in Rhoads and Sukhodolov (2008), near the upstream corner, it is possible that there is not a single central mixing layer, but actually two mixing layers, one at each side of the stagnation zone, that continue as one, central mixing layer downstream of the stagnation zone.

Because the performed experiments have been recorded from some distance upstream to well downstream of the confluence, they are particularly suited to perform a similar analysis, without being restricted by data availability. Furthermore, since also data in the downstream channel are available, the separation mixing layer can also be studied. Because of the flow contraction towards the downstream corner, and the low velocities in the separation zone, very high velocity gradients and a pronounced mixing layer is expected. The analysis of the mixing layers is performed for a single flow rate, $q = 0.66$. This flow rate is chosen because it is

the case with velocity data where the central mixing layer starts closest to the upstream corner (see figure 3.9b), it presents a case for which the tributary has a significant influence, and it is the value of q adopted in Mignot et al. (2014b), which should enable the comparison of results.

3.2.1 Streamlines and Normals in the confluence

Based on the acquired mean velocity field, the streamlines and normals (and the associated natural coordinate system (S,N) based on the central streamline) can be calculated over the entire confluence domain (see Mignot et al. (2014b) for a full description of the method). For the sake of clarity the N axis is chosen to be positive towards the main channel outer wall over the entire confluence, instead of towards the local centre of curvature. This is done to prevent that a small local change in curvature would change the location of the centre of curvature to the other side of the central streamline, which would result in a representation of normals that is difficult to interpret. Figure 3.10 (a) shows a selection of streamlines and normals, with the central reference streamline that is defined as N=0 for all S values. Near the upstream confluence corner, the central streamline runs trough the stagnation zone. To prevent that the location of the streamline would be influenced by the larger uncertainty of the velocity data in the stagnation zone, this streamline is defined as the average location of the two bounding streamlines (in grey line in figure 3.10 (a)), at both sides of the stagnation zone.

Figure 3.10 (b) to (e) show a selection of four profiles of streamwise velocity U_s (equal to the velocity magnitude) along the normals, indicated in bold dotted line in figure 3.10 (a). The origin ($S = 0$) of the streamline was chosen to correspond to the downstream end of the stagnation zone, i.e. where no more local velocity deficit is present. This local velocity deficit is clearly observable around $N/W = 0$ when comparing the profiles of n1 and n4.

The streamlines in figure 3.10 (a) illustrate the main flow patterns. The streamlines originating in the upstream main channel experience an S-shape as identified by Biron et al. (1996): upstream, the streamlines are aligned with the main channel; approaching the stagnation zone ($x/W \approx -0.5$), the streamlines start to curve towards the left bank, to then re-align with the main channel direction; once the streamlines pass the maximum width of the separation zone ($x/W > 1$), the streamlines (slightly) curve towards the right bank, and finally re-align with the main channel direction again.

Streamlines originating in the tributary exhibit a very strong curvature into the main flow, since they experience a 90° direction change in a very confined space. Curvature only significantly decreases once the streamlines pass the cross-section $x/W = 1$, i.e. the cross-section where the separation zone reaches maximum width and the flow contraction is maximum. The curvature of these streamlines is observable a significant distance upstream of the confluence zone, again indicating the confluence imposes an upstream influence into the tributary channel.
The normals originating close to the upstream corner extend long distances into the tributary and to a lesser extent into the main upstream channel.

In the separation zone, normals can only be calculated over a limited distance, since in the central area of the separation zone velocities approach zero magnitude, and the direction becomes undefined. Nonetheless, it is clearly observed that the normals located in the separation zone all curve towards a common point, the central point of rotation of the separated flow, a flow feature also observed in the flow separation at a channel diversion (Mignot et al., 2014a).

Figure 3.10 (b) to (e) present the overall evolution of the streamwise velocity U_s of the different selected normal profiles over the confluence. Profile n1, located very close to the upstream corner, clearly shows the two incoming velocity cores. Both at the main channel and the tributary side, maximum velocities are observed at the outer sides of the velocity profile, and a pronounced velocity deficit is present in between, indicative of wake-type behaviour as identified in Rhoads and Sukhodolov (2008).

The central mixing layer between the incoming flows thus actually consists of two mixing layers, one at the main channel side (further referred to as MM) and one at the tributary side (further referred to as MT) of the flow stagnation zone, both indicated in the velocity profile (n1).

In the second selected velocity profile (n4), located near the inlet of the downstream branch, the velocity deficit between the two velocity cores has disappeared, and only the MT is still perceivable. The wake mode was replaced by the mixing layer mode. A contraction of the total width of the normal is observable, due to the significant geometrical contraction of the confluence, and leads to overall acceleration over the entire flow profile. Furthermore, the velocities at the main channel side (positive N values) have become more uniform due to the flow contraction, while the velocities at the tributary side continuously increase towards the outer wall (more

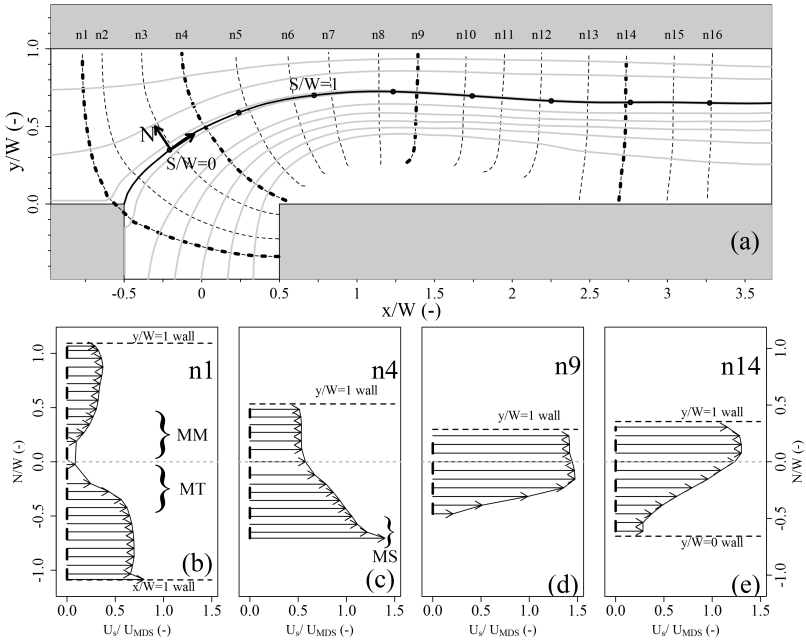

Figure 3.10: (a) Selection of streamlines (grey line) and normals(dashed line) of the measured velocity field. On the central streamline (bold line) a reference axis for S is given by indicating S every 0.5W ; (b-e) Representative non-dimensional velocity profiles along four normals (q=0.66.

negative N values), and no clear uniform outer velocity is discernible at the tributary side. The third selected profile (n9), situated near the most contracted section, clearly reveals the influence of the separation zone next to the contracted flow. Within the contracted section the velocity profile is highly uniform, and the MT no longer exists. Oppositely, a very large velocity difference is observed between the highly accelerated flow in the contracted section (U_s/U_{MDS} up to 1.5) and the near-zero velocities in the separation zone. For the most negative N-values, a very steep gradient next to the maximum velocity is present. This high velocity core has been associated with jet behaviour (Rhoads and Sukhodolov, 2008), and is the initiation of the third mixing layer, the separation zone mixing layer (MS).

The fourth selected normal (n14) is situated downstream of the sepa-

ration zone, where the flow has reattached to the wall, and the final flow recovery is taking place towards a developed flow profile. The MS remains discernible, even though the separation zone is not present any more. In this final flow recovery zone, flow profiles are self-similar when non-dimensionalised with the velocity difference, and resemble a behaviour similar to a wake behind an expansion of the channel width at one side.

3.2.2 Analysis of velocity profiles along the normals

Figure 3.11 shows the velocity profiles, represented in natural coordinates, for all normals indicated in figure 3.10 (a). The evolution of the different mixing layers is clearly visible, as well as the influence of the lateral confinement by the confluence walls. Notably, because of the representation in natural coordinates, the very sharp and abrupt confinement of the confluence walls is transformed into a continuous and more gentle decrease in available width ($n1 \rightarrow n8$) and increase as the width of the separation zone decreases ($n8 \rightarrow n13$). The influence of the upstream end of the separation zone is clearly visible when comparing n4 to n5. At n4 the maximum velocity is observed at the outer wall of the tributary, because of the strong tributary flow contraction towards the downstream corner. In n5, the flow has separated, and the maximum velocity is shifted towards the center of the flow, introducing a strong velocity gradient with the separation zone. Farther downstream, the flow contraction results in a more and more uniform velocity profile at the main channel side ($N/W > 0$), while at the side of the separation zone the width of the mixing layer increases (Mignot et al., 2014a). Downstream of the separation zone, the final flow recovery starts as the flow reattaches to the wall (n13), as can also be seen from the slight increase in minimum velocity along the profile.

3.2.3 Mixing layer properties

To further investigate the behaviour of the three previously identified mixing layers, some typical parameters are computed in the same way as for well-defined straight mixing layer analysis. Figure 3.12 depicts the absolute value of the outer velocity differences over the mixing layer ($\Delta U/U_{MDS}$), maximum gradients ($[\partial U_s/\partial n]_{max}$) and mixing layer widths ($\delta = \Delta U/[\partial U_s/\partial n]_{max}$) for the different mixing layers, as a function of the streamline distance S (see Mignot et al. (2014b,a) for further details).

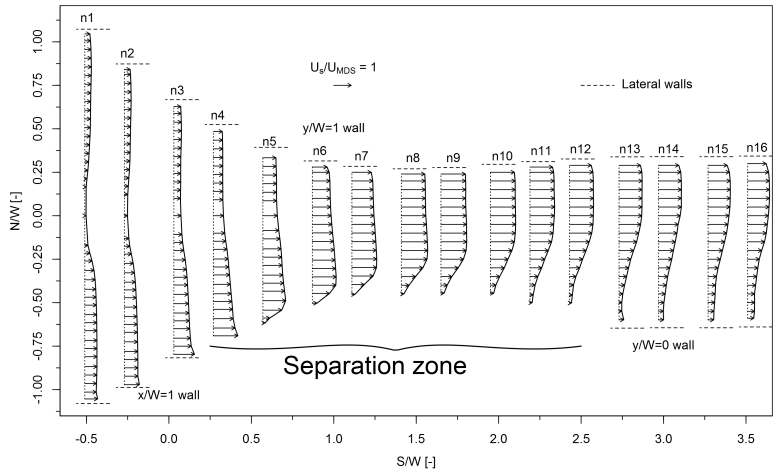

Figure 3.11: Non-dimensional streamwise velocity profiles over the normals from figure 3.10 (a) throughout the confluence for q=0.66.

The quantities have been made dimensionless with the downstream velocity U_{MDS} and channel width W. Note that to prevent influence of small measurement inaccuracies, the gradient of the velocity profiles have been determined with a higher (third) order central difference scheme.

The initial outer velocity difference over MM is almost equal to the upstream bulk velocity magnitude in the main channel $\Delta U_{MM} \approx (1-q) = 1/3$. As MS progresses downstream, both the velocity difference and the maximum gradient decrease so that the mixing layer width stays more or less constant. This mixing layer is thus decreasing in strength, as would be expected, but not growing in size.

At the other side of the stagnation zone, the initial outer velocity difference over the MT is close to the tributary velocity magnitude $\Delta U_{MT} \approx q = 2/3$. Farther downstream, the velocity difference over the mixing layer first slightly increases, as the tributary flow accelerates. For $n > n3$, the velocity deficit inside the stagnation zone has disappeared, and ΔU decreases (Mignot et al., 2014b). The magnitude of the maximum gradient observed in the MT is monotonously decreasing from up to downstream

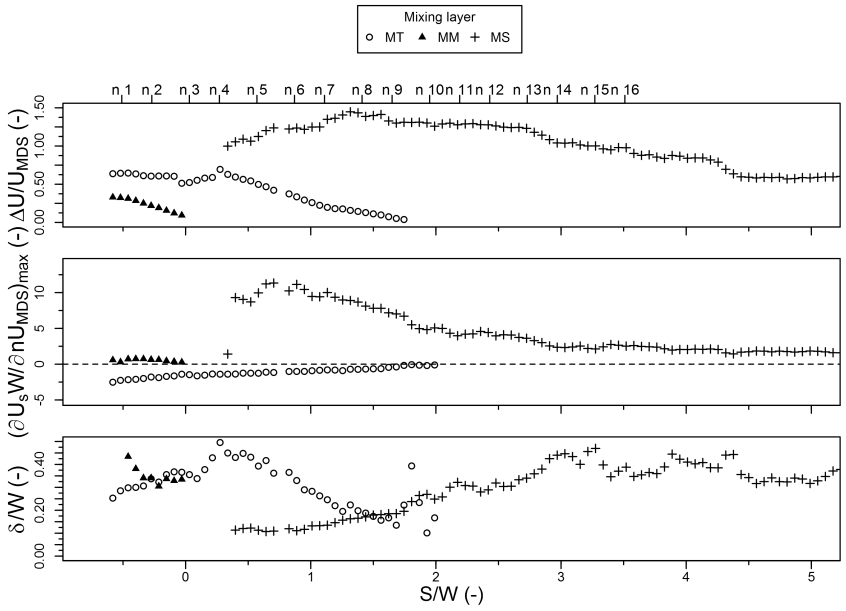

Figure 3.12: Outer velocity differences, maximum gradients and widths of the different mixing layers for q=0.66.

(as also observed in Mignot et al. (2014b)), and no difference in trend is observable between the wake mode ($S/W < 0$) and (single) mixing layer mode ($S/W > 0$). Consequently, the mixing layer width evolution resembles the velocity difference, with an initial increase upstream of the flow separation (Mignot et al., 2014b), followed by a decrease towards downstream.

Finally, the mixing layer at the border of the separation zone, MS is initially much stronger, with higher ΔU and maximum gradient, than MT and MM, as the tributary flow adjacent to the stagnation zone is highly accelerated (see n3 in Figure 3.11 (a)). The outer velocity difference first increases ($n3 \rightarrow n8$) with downstream distance because of the flow contraction, and then diminishes downstream of the most contracted section ($n > n8$). The initial maximum gradient starts at its maximum value, and decreases towards downstream. The width of MS is found to increase

with S, up to the flow reattachment (n13). From there onwards, the mixing layer width remains more or less constant, while the outer velocity difference and gradient tend to zero.

3.2.4 Evolution of the wake mode

Figure 3.13 (a) shows a selection of velocity profiles very close to the stagnation point, representing the evolution of the wake mode. The local velocity deficit between the two higher velocity cores coming from the incoming branches is observed for $S/W < 0$. These velocity cores are however not uniform, since flow redistribution has caused the highest velocities at both sides to be near the outer walls of the confluence. With downstream distance, the velocity deficit quickly diminishes, and the outer velocities increase because of the lateral flow contraction. The flow contraction causes the flow at the tributary side to accelerate to a greater extent than the one at the main channel side, in agreement with the earlier observation that the velocity difference over the MT initially increases. It is also perceivable that the width of the low velocity zone decreases, and gets suppressed by the growth of the MM and the MT.

Figure 3.13 (b) shows the streamwise evolution of the velocity on the central streamline. The velocity at the stagnation point is zero, and then increases with downstream distance. This increase is a combined effect of the flow contraction causing a general increase in average velocity over a normal, and the dissolution of the local velocity deficit. At $S/W \approx 1$ the centerline velocity is equal to the downstream velocity, it then increases towards downstream because of the formation of the separation zone, until the final deceleration downstream of the separation zone towards the downstream velocity.

3.2.4.1 Spatial extent of the mixing layers

Figure 3.14 shows the spatial location of the three identified mixing layers throughout the confluence, defined as the location of maximum velocity gradient across the normal, and assuming a symmetrical mixing layer width on both sides. Near the upstream corner, the two mixing layers MM and MT are visible at both sides of the stagnation zone. The area in-between corresponds to the zone of relatively uniform low velocity, de-

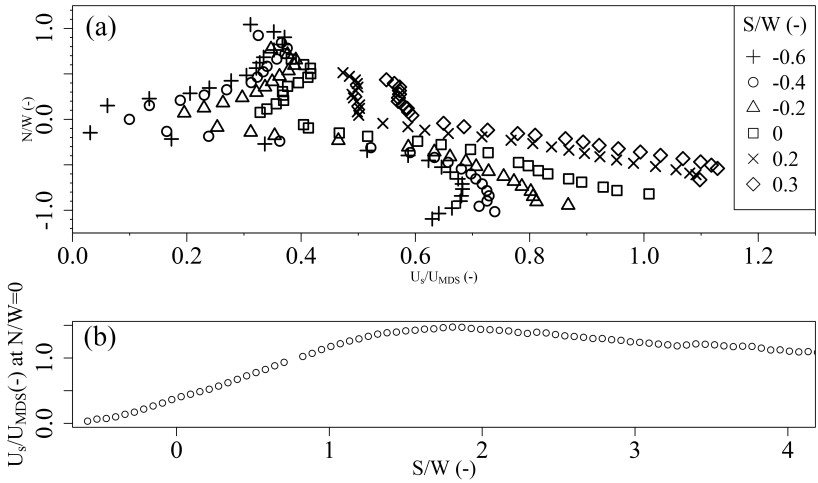

Figure 3.13: (a) Selection of normals close to the stagnation zone (b) Evolution of the centreline velocity for q=0.66.

lineated by two velocity gradients, associated with the wake behaviour. The spatial extent of this zone diminishes, until the two mixing layers start to interact spatially. At this point, the velocity difference over MM has, however, disappeared so that MM is no longer present. Downstream of the separation point, both MT and MS exist, but are spatially separated. The flow contraction next to the separation zone results in increasing uniformity of the flow profile, and at $x/W \approx 1.5$ MT is no longer present. Close to the downstream corner, the centreline of MS first more or less follows the separating streamline, but spatially separates at the most contracted section and slowly moves towards the centre of the channel.

As reported in the literature (Biron et al., 1996; Best and Reid, 1984; Mignot et al., 2014b), the location of the separating streamline depends on a lot of parameters e.g. confluence planform geometry, relative flow rates, cross-sectional shape etc., and changes in the determining parameters will surely influence the location and characteristics of MM, MT and MS. Therefore the mixing layer locations as depicted in figure 3.14 are only valid for the current investigated (surface) velocity field. Yet, it provides some valuable information on how the mixing layers spatially

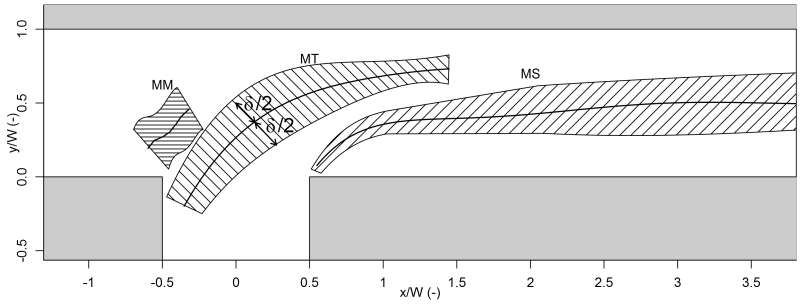

Figure 3.14: Sketch of the spatial extent of the different mixing layers within the confluence.

develop within the complex environment of an asymmetrical confluence, and together with the rich literature on confluence flow contributes to the understanding of the mixing capacity in such a flow configuration.

3.2.5 Conceptual representation of the mixing layers within the heavily contracting confluence geometry

The transformation of the velocity measurements to the natural coordinate system introduces a different representation of the flow. Making abstraction of the curvature effects that are hidden in a representation in natural coordinates, the flow redistribution in a confluence can be represented by a straight channel approximation with continuously varying width as presented in figure 3.15. The incoming flows are separated by a thick splitter plate (representing the effect of the stagnation zone), upstream of the confluence. Because of the splitter plate thickness, a wake develops in between the two incoming flows in region I. Simultaneously, the flow is contracted on both sides. In region II, the wake has disappeared, and the two flows interact, while being further contracted and accelerated. In region III, the third mixing layer MS develops. It is also in this region that the flow reaches maximum contraction. In region IV the intensity of MS decreases and the flow recovers to a fully developed profile over the width of the downstream channel.

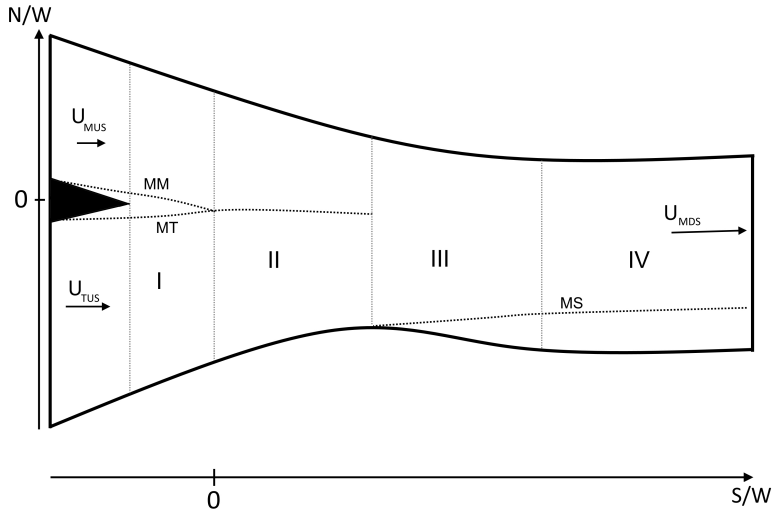

Figure 3.15: Straight channel approximation of confluence flow, with indication of the different regions of typical behaviour.

3.2.6 Discussion and Conclusion

The surface velocity fields obtained by application of Surface PTV give a detailed data set for the study of the different mixing layers at an open channel confluence. Analyzing figure 3.10, some of the features reported in the literature are apparent. The stagnation zone is observed near the upstream corner, as well as the separation and contraction zone. In the tributary branch, a clear deflection of the streamlines towards the downstream corner is observed, as predicted by Modi et al. (1981) and Webber and Greated (1966) with the help of conformal mapping theory. In the main channel, near the stagnation zone, the inflection in the streamline curvature, as described in e.g. Bradbrook et al. (2001) or Mignot et al. (2014b) is clearly observable. Approaching the stagnation zone ($-0.75 < x/W < 0$) near the inner confluence wall ($y/W = 0$), the streamlines curve away from the tributary, towards the outer wall ($y/W = 1$). This curvature is, however, quickly reduced again, and even changes sign, so the streamlines become aligned with the main channel

banks again. This S-curve behaviour of the streamlines is intrinsically related to the presence of the stagnation zone and the associated slow flow speeds. It is caused by the colliding flows converting kinetic energy into a local superelevation of the water level in the stagnation zone, hence a pressure gradient redirects the flow from the tributary into the main channel (Bradbrook et al., 2001; Tancock, 2014). The interface between the incoming flows causes a mixing layer between the flows, with a velocity difference that is (partly) determined by the incoming flow ratio. Performing an analysis of the velocity field for q=0.66, the stagnation zone is actually delineated by two mixing layers (typical of wake mode), merging into one further downstream in the confluence (mixing layer mode), contrary to what would be expected for this high momentum ratio. This is probably due to the high confluence angle, maximizing the effect of the adverse pressure gradient, and locally redistributing the flow. The stagnation zone with two mixing layers on the side was not observed in Mignot et al. (2014b) for their case F1, probably since the first analysed normal was further away from the corner, and no measurement data was available upstream of the confluence zone. Farther into the confluence the MT quickly reduces in strength, because of the strong lateral contraction that has a uniformization effect on the streamwise velocity magnitudes (Rhoads and Sukhodolov, 2001; Mignot et al., 2014b, 2012). Slight upstream velocities in the stagnation zone as observed in Rhoads and Sukhodolov (2001), are also observed in the current experiments, albeit in a very confined zone near the upstream confluence corner.

While the velocities in the separation zone are very low, the velocities near the opposite bank are significantly increased, due to the flow contraction by the large lateral component of the incoming tributary flow. Consequently, a very high velocity gradient forms with associated shear layer. In the cross-section where the separation zone reaches its maximum width, the flow in the contracted zone has become more or less aligned with the main channel and shows a zone of rather uniform velocities, as often reported in literature (Gurram et al., 1997; Hsu et al., 1998). As described in Weber et al. (2001), no reattachment of the separating streamline to the wall is observed, because of upwelling flow near the bank. Visual observation of the tracer particles confirms the presence of the upwelling flow in the separation zone. This effect is possibly also enhanced by the presence of the chamfer (Schindfessel et al., 2015b,a), facilitating the transfer from lateral to vertical momentum.

Finally, it is important to realize that the entire analysis was performed on a velocity field captured at the free surface. Although the mixing interface is sometimes reported to remain quite vertical and confined (Rhoads and Sukhodolov, 2001; Biron et al., 2004, 1993), it is certain the flow will have a three-dimensional topology, as can be seen in the experiments by e.g. Weber et al. (2001) and Shakibainia et al. (2010). This is confirmed in the current experiments, since a comparison of the velocity in the contracted section at the free surface with the velocity expected by calculation from the observed separating streamline shows a significant disagreement. The three-dimensionality might be even further enhanced by the relatively deep flow depths, that are shown to have an impact on flow mixing (Lewis and Rhoads, 2015a), and the specific chamfers of the flume utilized in the present experiments (Schindfessel et al., 2014, 2015b). Formation of the Streamwise oriented vortices has been shown to significantly distort the mixing layer (Constantinescu et al., 2011), a feature that can surely be influenced by relative depth and channel geometry.

Furthermore, the analysis was limited to the time-averaged properties of the mixing layers, and no information about turbulent structures or other types of time-dependent behaviour has been processed or presented. To further understand the mixing behaviour, formation, transport and disappearance of coherent structures, as well as other turbulent quantities should be studied, as is e.g. performed in Constantinescu et al. (2016). To perform the time-dependant analysis of the mixing layers, a time-resolved velocity field should be available over a large enough time base to obtain converged results, which could not be obtained from the current measurement methodology. Despite the fact no in-depth analysis of time-dependent behaviour was performed in the current work, it was observed that the position of the central mixing layer between the incoming flows was not constant in time, but showed some long-term oscillations, as reported in Biron et al. (1993). Furthermore, the formation of coherent structures in the wake and central mixing layer was limited, and only in the MS significant formation, transport and growth of large coherent structures was observed.

Chapter 4

Experimental study of the free surface elevations

4.1 Design and construction of the new flume

As outlined in the methodology, next to the velocity field obtained and presented in chapter 2, also a high resolution data set of water depths is envisioned to meet **(O1)**. For these measurements, a new flume is constructed at the Hydraulics Laboratory of Ghent University. An impression of the confluence flume, applied for confluence research is shown in figure 4.1.

The flume is constructed to enable experimental work in open channel confluences in the best conditions possible. It consists out of six straight flume parts; a confluence piece, equipped to enable changes in the confluence corner and discordance ratio; and the required up- and downstream inlet and outlet structures.

The outline of the flume with overall dimensions is sketched in figure 4.2. The width of all the channels is W=0.4 m. The total length of the main channel is 12 m, the tributary channel is 2 m long.

4.1.1 Confluence flume pieces

The confluence flume is constructed out of transparent polycarbonate. It is essentially constructed out of two kinds of polycarbonate plates, 6 mm thick for the large areas and 20 mm for pieces that need constructive

Figure 4.1: Impression of the confluence flume, applied for confluence research. Blue dye has been applied to outline the separation zone, yellow wires are applied in the tributary to illustrate the streamline curvature.

strength. Using the thick plate in combination with an appropriate glue allows for seamless polycarbonate flume pieces, without having to use opaque materials that would again hinder optical access.
The basis of the flume pieces is the 6 mm plate that is shaped in factory to a U-shape of 2 m long, 0.4 m wide with 0.5 m high edges. This U-beam is bent under a heat treatment, to ensure a very sharp finishing of the corners (rounding of the edge in the order of 1 mm). By constructing the entire beam out of 1 plate, there are no joints between the bottom and the sides of the flume, and perfect water tightness is ensured.

To couple the different pieces of the flume, a standardized flange is constructed, illustrated in figure 4.3. The flange is constructed out of the thick plate, and has a groove where the flume piece can be glued into. Because the groove is sunk 6 mm into the flange, the flume and flange are joined with only a very minimal seam and no depth difference. Near the outer edges of the coupling piece, holes allow to bolt two flanges together, obtaining a perfectly aligned and rigid connection between two flume pieces. Between the flanges, two rubber strips are placed in two small grooves, to ensure water tightness of the connection.

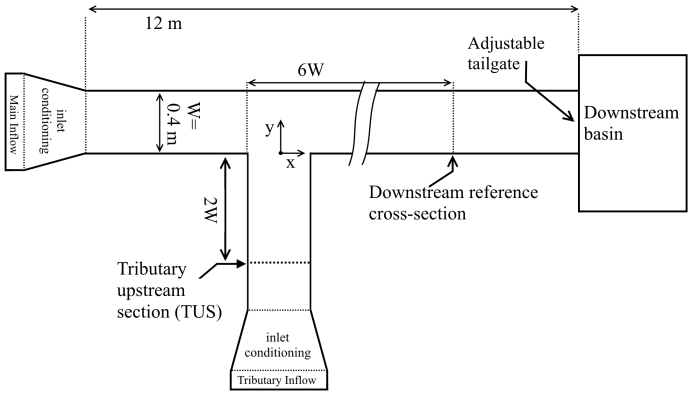

Figure 4.2: Sketch of the flume mounted with a 90° angle, indicating the most important dimensions.

4.1.2 Confluence joining piece

At the confluence, both up- and downstream main channel flume parts, as well as the tributary channel need to be connected. To allow the broadest of possibilities open for future research, the confluence piece had to be designed so that both a change in angle, as well as bed discordance are possible. Since high quality data are envisioned, good detailing of the confluence geometry was identified as being of paramount importance. Therefore, no solution was chosen employing flexible sides or movable pieces. This would be detrimental for the finishing of the confluence geometry, and influence the experimental results. Moreover, in these kind of solutions it is very difficult to secure watertightness, which would lead to a lot of practical problems in the operation of the flume. Because of the modularity of the entire flume set-up, it is relatively easy to mount and dismount flume pieces. This leads to the design of the confluence joining piece made out of a central main channel piece, where by application of different side pieces, the confluence geometry can be altered. The central main channel piece is a piece like the other flume pieces, with one of the sides removed over a large distance (0.8 m), and with a larger version of the flume flanges attached. By subsequently mounting a custom made tributary piece, the desired confluence geometry can be obtained. By then mounting the desired flume pieces to the tributary flange, the con-

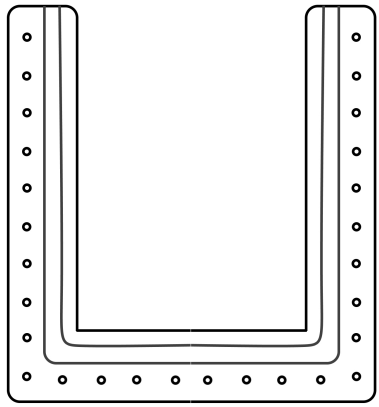

Figure 4.3: flange for the flume to ensure well-aligned mounting of the flume and watertightness. Circles represent holes for the bolts, the rubbers are indicated by the grey lines.

fluence can be constructed with the desired geometry, while maintaining the highly detailed finishing and good water tightness.

4.1.3 Supporting structure

The supporting structure is fabricated out of aluminium profiles. This allows for a relatively slender supporting structure, that is fully modular. Modularity of the supporting structure has three important advantages:

- In case the profiles hinder visual access at a certain position, the frame can be adapted. By mounting supporting legs at a different location, or by moving the longitudinal supporting beams, the visual access at the location of interest can be restored.

- The flume can be adapted for new configurations quite flexibly. It is possible to apply a slope, change the confluence angle (provided a new joining piece is constructed), etc.

- By adding extra profiles to the supporting structure, measurement equipment can be installed in a flexible and reliable way. Modularity of the profile structure also means that any specific mounting

brackets for equipment can be mounted at any position on one of the aluminium profiles. Furthermore, this makes the placement of equipment very reliable, since the position of the equipment is directly based on the supporting structure. This helps in correct relative positioning and alignment of the experimental measurement devices.

4.1.4 Inlet system of the flume

To ensure maximum quality and usability of the experimental results, the boundary conditions at the inlet of the flume should be well controlled. The Hydraulics Laboratory (Dep. of Civil Engineering, Ghent University) has a closed circuit water supply, with adequate pumping capacity. Therefore, the flume was connected to this general circuit. The incoming flows are sampled with electromagnetic flow meters, which allows to conveniently check the incoming flow rates. It is also possible to log the flows, to check whether no variations in the incoming flows are observable. The general water supply of the laboratory is, however, very steady, by the application of a constant head tank that supplies the general circuit. This ensures a very constant pressure at the pipe inlets, and thus if the experiment is given adequate start up time to reach full equilibrium conditions, ensures a very constant water supply.

On top of the stability of the incoming flow, also the flow distribution over the cross section of the flume is important. The incoming flow out of the supply pipe should be well distributed, and given adequate time to evolve towards a fully developed flow profile. The first precaution that is taken is to ensure enough upstream length for the profile to develop. The total upstream lengths are 4 m and 2 m, for main channel and tributary, respectively. For a typical water depth of 0.1 m this corresponds to 60 and 30 times the hydraulic radius. Secondly, the inlet structure is designed to distribute the incoming flow evenly over the cross section of the flume. By ensuring the incoming velocity distribution is as close as possible to the developed profile, the adaptation length is reduced. To this end, a two layered inflow structure is designed for the flume, depicted in figure 4.4.

The incoming flow gets evenly distributed over the bottom tank by closing the inflow pipe at the end, and perforating the last piece of the pipe. A large amount of holes are drilled, to ensure the relative throughflow surface is very large, and a very calm outflow is ensured. The most upstream half of the lid of the bottom part of the tank is perforated to allow the flow to go from the bottom tank to the top. Underneath this

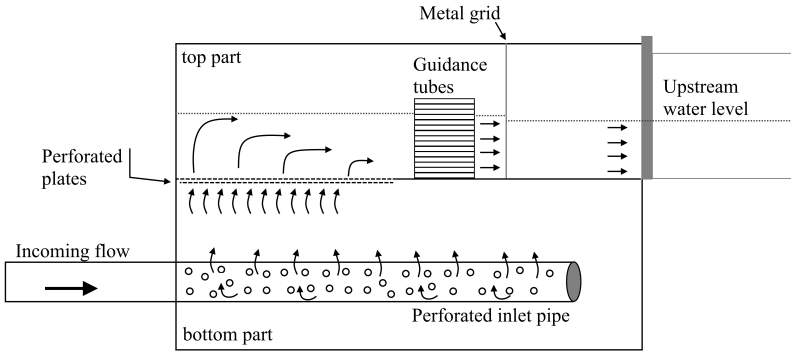

Figure 4.4: Schematic representation of the inlet strucure of the flume.

perforated plate, a second, movable plate with identical perforations is mounted. This configuration allows to regulate the diameter (and shape) of the openings between the bottom and top part of the tank. By adapting the opening area of the holes the strength of the upward directed jets can be regulated, as such influencing the division of the flow over the vertical. Once the water is in the top part of the tank, it is guided by (mildly) contracting side walls, through two flow redistribution structures. The first one is a series of small horizontal pipes, that are mounted in the direction of the flume, and orient the flow towards downstream, destroying large secondary motions that might exist. Secondly, a (series) of metal grids is applied for a final uniformization. Several of these grids can be applied in series, and grids with multiple mesh size are available. This allows to have some control over the upstream boundary, in case a measurement of the incoming flow profiles would indicate the requirement to adapt the inlet structure. Finally, just downstream of the tank, a small strip of floating (Polyurethane) foam has been applied, to suppress any surface turbulence that is created by the flow through the meshed grids, in order not to disturb the water level measurements.

4.1.5 Downstream weir

At the downstream section, a movable overflow type weir is installed to allow a well controlled downstream boundary condition. The weir is only fixed by a threaded rod at the top, which allows very precise control over the weir depth. To support the weir at the sides it slides against two rubber strips, that ensure water tightness while still maintaining movability. At the bottom, the weir also is mounted against a rubber strip, so that the weir can be lowered completely to the bottom level, to obtain very low water depths if desired (see figure 4.5).

Figure 4.5: Downstream weir in completely lowered position.

4.2 Automated gauging needle for measurements of the free surface

Within the scope of this work, experimental measurements of the free surface levels over an extensive measurement domain are envisioned. Since the data is gathered to enable validation of numerical work, the measurement grid resolution and accuracy should be sufficiently high. Moreover, since the flow in the confluence is quite turbulent at some locations, each location should be repetitively measured to obtain a true time-averaged water level. In this section the conception and practical implementation of an automated system applying a gauging needle to sample the flow depths is described.

4.2.1 Measurement principle

The automated gauging system works as follows: an electrically conductive needle is vertically mounted on a vertical rod. This rod is mounted to an actuator that can move the needle up and down. The needle is connected to a digital logger, and is kept under electrical tension, over a large electrical resistor. As soon as the needle touches the water surface, the needle is grounded through the electrically conductive water. The digital logger knows the position of the needle, and upon making contact registers the actual position, thus resulting in the measurement of the water level.

4.2.2 Practical implementation

The electronically sampled sensing needle is mounted on a vertical rod driven by a stepper motor. This allows to move the needle up and down with increments of 0.0125 mm. Since the flow can have turbulent surface fluctuations, and a lot of measurements have to be performed, a lot of effort is dedicated to get high measurement speeds, enabling a measurement frequency in the order of 2 Hz. By logging the electronic response of the needle making contact with the water surface, the position of the free surface is recorded. Because of the temporal variability of the free surface, 30 samples are taken per grid point, enabling the calculation of a time-averaged free surface position. Because the needle moves to a position well above the free surface before taking a following measurement, problems of capillarity resulting in biased surface levels are avoided.

Figure 4.6: Photo of the traverse system mounted on the flume. The system allows a fully automated operation of the gauging needle over a set measurement grid.

This automated procedure removes the cognitive bias of a manual measurement with a gauging needle. In case of manual measurements, the decision whether the needle is exactly at the surface level is subjective, and under turbulent flow conditions inevitably leads to larger margins of error on the determination of the free surface location. In order to be able to measure an extensive grid of points, the measurement needle is mounted on a traverse system, which allows automated movement of the needle to different points in the measurement domain (see figure 4.6).

Together, the needle system and traverse system form the measurement robot, mounted on a rigid frame on top of the confluence flume, that allows fully automated measurement of the implemented experimental programme.

4.2.3 Calibration

Before starting with the measurements, a calibration procedure is performed. In this procedure, the position of the measurement robot relative to a set reference water level is recorded. Although careful mounting of the measurement robot was performed to have the local reference of the robot as horizontal as possible, small mounting errors can be expected,

and should be corrected. Furthermore, since the pursued measurement accuracy is relativity high, the deformation of the supporting frame by the weight of the robot is not negligible. Since the deformation of the supporting frame is only a function of the location of the traverse, it can be corrected by determining the height of the traverse with respect to the fixed water level for each position. The combined effect of these potential horizontality errors is captured, and a calibration function is derived, that can be used to eliminate the previously mentioned effects. Horizontality errors of the traverse are found to be in the order of 1 mm/m and the maximum deformation of the frame beams in the middle of the channel is about 0.3 mm.

4.2.4 Measurement validation

Accuracy of the measurement system is estimated with three different approaches. In a first validation step, individual measurements of the calibration run are compared with the calibration function. This provides an estimate of the variability of individual measurements versus the averaged values. The maximum deviation is found to be 0.25 mm. When this step is completed, a second fixed water level is implemented, and subsequently sampled, to determine the accuracy of the usage of the calibration procedure. Since the level difference between two fixed water levels is constant, the accuracy of the calibration procedure can be tested by comparing depth recordings for each of the grid positions. Analysis shows that the maximum error is 0.25 mm, which indicates that the calibration procedure yields accurate results and that the main source of differences are deviations in the individual measurements. In a last step, the influence of experimental conditions and repeatability on the measurement accuracy is checked. For this test, the flows are set up and sampled twice at q=0.75 (with the rest of the flow conditions as outlined below). The average error between the two measurements is 0.1 mm, the maximum error 0.5 mm, and 95 percent of the measurements differs by less then 0.25 mm.

4.3 The importance of the free surface in an asymmetrical confluence

Throughout the literature, the analysis of the asymmetrical confluence flow has been performed mainly with a strong focus on velocity information, because of the interesting features such as the (low-velocity) stagnation zone, separation zone, shear layers and associated coherent structures. With respect to the surface levels, only the study of the headlosses over the confluence (and thus the ratio of up to downstream water depths) has been investigated intensively. However, to fully understand the complex flow, and to be able to grasp the complex pattern of flow accelerations, decelerations and directional changes, it is important to also investigate the local surface levels and associated gradients over the entire CHZ.

Near the stagnation zone, flows are decelerated, and an increase in flow depth is apparent. This local super-elevation causes a pressure gradient towards the downstream branch of the main channel, which redirects the flow of the tributary branch into the downstream main channel (Bradbrook et al., 2000). The local deceleration of the flow near the stagnation zone has already been established multiple times (Hsu et al., 1998; Weber et al., 2001; Hager, 1989; Ramamurthy et al., 1988), but on the surface levels far less experimental data is available (Weber et al., 2001; Gurram et al., 1997). Downstream of the confluence, the flow can separate and a zone with a distinctive surface depression is observed. In the contracted section, a surface depression is also present, caused by the flow acceleration. This depression is, however, of smaller amplitude than the separation zone depression (Gurram et al., 1997). Downstream of the contracted section and separation zone, the water levels gradually evolve towards the downstream water depth with increasing distance from the confluence.

Because of the high complexity of the flow field in asymmetrical open channel confluences, they are often studied with the help of numerical codes. In the literature, a lot of numerical models have used the data for validation purposes. Some of these models applied a Reynolds-averaged Navier-Stokes (RANS) formulation with a turbulence closure model (e.g. Dorđević (2013), Huang et al. (2002)), whereas others adopted an eddy-resolving approach, like e.g. Large Eddy Simulations, or a hybrid RANS-LES approach (e.g. Zeng and Li (2010)). In the aforementioned numerical models, the free surface has been modelled with different approaches such

as a rigid lid (Dorđević, 2013; Schindfessel, 2017) or interface-tracking methods with moving meshes (Huang et al., 2002; Zeng and Li, 2010). As indicated, in asymmetrical confluences with moderate to high Froude numbers, the surface gradients become significant and need to be modelled correctly to capture the governing processes. Depending on the treatment of the free surface - for which even other than the aforementioned approaches are being adopted in state-of-the-art numerical models, including interface-capturing methods with fixed meshes, such as the Volume of Fluid method and the Level -Set Method (Rodi et al., 2013) - the obtained results can vary in accuracy. For example, Bradbrook et al. (2000) states that for predicting the length of the separation zone free surface effects are more important than the applied turbulence model. While the dataset of Weber et al. (2001) allows for an overall evaluation of the model in predicting water levels for the cases with available water levels, coarseness of the measurement grid and the manual measurement method hinder comparison of local gradient information. The water depth recordings in this chapter should thus contibute to available data sets for model validation, so that also the free surface predictions can be adequately validated.

4.4 Adopted flow conditions

For the measurements of the free surface in the new flume, the flow conditions are chosen to obtain a Froude scaled version of the experimental conditions of Weber et al. (2001). The moderately high downstream Froude number of 0.37 adopted is a proper choice, since it is high enough to induce clear free surface effects, while it is still low enough to ensure fully subcritical conditions throughout the confluence. The range of flow ratios (q = 0.083, 0.25, 0.417, 0.583, 0.750, 0.917) provides a good coverage of flow ratios to deduce the effects of changes in q. For W = 0.4 m this corresponds to a downstream water depth (measured at a reference section x/W=5.5) of 13.3 cm. This leads to a Reynolds number of:

$$Re = \frac{U\mathbb{R}}{\nu} = 34,000(-). \tag{4.1}$$

The correspondence in flow conditions is chosen to maximize the utility of the obtained experimental data, i.e. to complement the already existing data. Since in Weber et al. (2001) also manual measurements of the free surface were performed at a selection of transects and for some of the flow

ratios, the newly acquired data can be compared to the existing data. Note that, although Weber et al. (2001) provided water depths on some transects, the focus of the study was on the description of the velocity fields. Furthermore, no water level recordings were performed for the extreme discharge ratios of q=0.083 and q=0.917. The measurements in the current study thus complete the water levels for the missing discharge ratios, and complement the measurements for the other cases because of the finer measurement resolution and higher accuracy.

4.5 Experimental results in the new flume

4.5.1 Water levels over the confluence

In figure 4.7, the experimentally recorded water depths are shown for different dimensionless flow ratios. It is immediately apparent that the increase of up to downstream water depth ratio is present, and that the increase in backwater effects with increasing q is established. Some of the typical flow features can be clearly identified. The most pronounced one is the large surface depression near the confluence inner wall of the main channel, associated with the separation zone. It is already apparent in the case with the smallest tributary discharge although very confined in space, and with a limited amplitude. With increasing values of q, the surface depression becomes more pronounced, and expands to downstream and towards the outer wall. The surface depression can however not be solely related to the separation zone as a one-to-one relationship.

First of all, the shape of the zone of surface depression appears to be more or less unchanged over the range of flow ratios, and has an almost triangular shape. This is different from the observed shape of the separation zone in chapter 3. In all cases but the first, the zone of surface depression is ending with a surface slope that is perpendicular to the channel walls. Moreover, with increasing q the gradient between the end of the surface depression and the downstream reference level is increasing, resulting in a more or less constant distance where the depression ends. This behaviour is different from what is observed for the separation zone. First of all, the separation zone is reported to be widening with the tributary flow ratio, but never reaches the opposite wall. Maximum widths of the separation zone reported are about $0.6W$, measured at the free surface, where the separation zone is known to be the widest. Second, the length of the separation zone is reported to be increasing with q, while the length of the

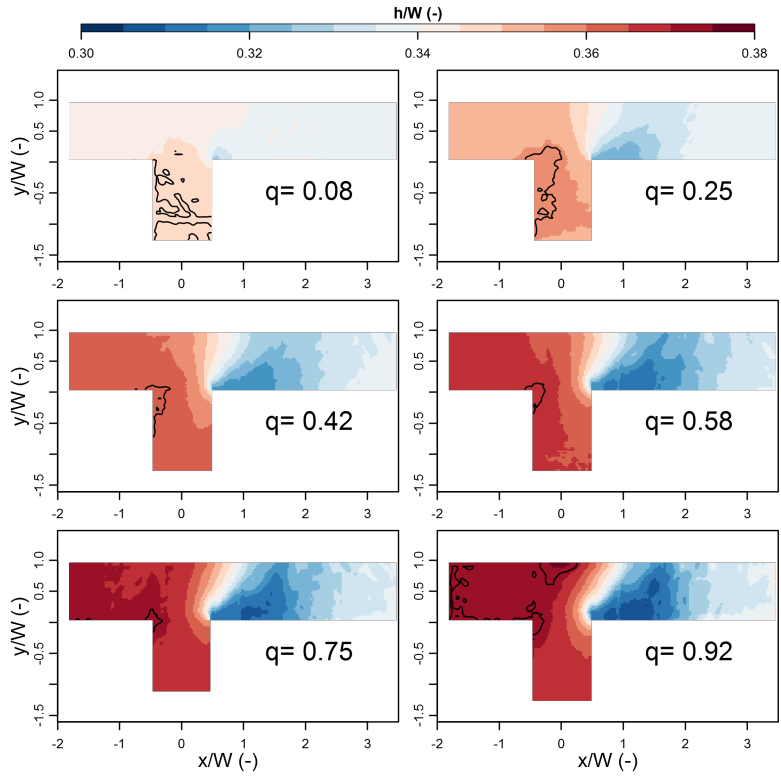

Figure 4.7: Water depths in the confluence for different flow ratios. A black contour line is drawn at half the velocity head below the maximum upstream water head to outline the stagnation zone.

surface depression zone is almost constant. However, L_{W_s} is more or less constant, and could potentially be linked with the zone of large surface depressions.

At the inflow section of the downstream channel (i.e. $x/W = 0$ to 0.5), a large surface gradient is apparent from the quick succession of the colour levels. This is the decrease in water levels caused by the contracting flow. Upstream of the confluence, a significantly larger cross-sectional area is available (2 channel widths), that is quickly diminishing in the downstream direction. Moreover, the flow separation causes a further flow contraction, amplifying the effects. Comparing the directionality of the contour lines, it is clear that the direction of maximum gradient (i.e. perpendicular to the contour lines) changes with changing q. For low flow ratios, the contour lines are showing a fanned shape around the downstream corner. The direction of maximum gradient is thus starting slightly oriented towards the main channel outer wall, and gradually changes towards a more downstream direction, and eventually towards the main channel inner wall. With increasing q, the contour lines become more and more parallel, and are directed more in the downstream direction. The zone that shows clear gradients already starts further upstream, and is immediately directed downstream, and even slightly angles towards the inner wall for q =0.92. Together with the upstream evolution of the gradient, the upstream distance of the flow that is disturbed by the confluence hydrodynamics increases. While traditionally the flow dynamics starting from the confluence zone and more downstream are studied, the presented measurements of the free surface indicate that a clear upstream influence can be present in the tributary branch. Also in the main channel upstream effects exist, but they are less pronounced. This indicates that when studying confluence hydrodynamics, the analysis should start a sufficiently large distance upstream of the confluence.

Finally, in figure 4.7, a black contour line is added to visualize the location, size and shape of the stagnation zone. The height of this contour line is (pragmatically) defined as half the incoming velocity head below the upstream total energy head, calculated in the upstream branch with the highest flow. Changes in size and shape cannot be unambiguously defined, but the evolution of the location is clearly changing with q. For low q, the stagnation zone is mainly observed in the tributary. With increasing values of q, it is pushed towards the main channel. For q=0.92, the stagnation zone has moved (partially) towards the main channel outer wall. Further analysis of the data (not shown) indicates that the local maximum water level is found near this outer wall, and thus the stagnation

point indeed has moved towards the outer wall.

4.5.2 Longitudinal water level profiles

In this section some water level profiles along the longitudinal direction of the confluence are given. These profiles are of particular interest because they illustrate the water level gradients in the direction of the main stream, and thus are relevant for the complex pattern of de- and accelerations in the confluence hydrodynamics zone.

Figure 4.8 presents longitudinal profiles over the main channel of the section-averaged water depths for different dimensionless flow ratios. The ratio of up- to downstream water depths is clearly increasing with increasing q. All the profiles show similar behaviour from up to downstream. The upstream water level remains quasi-constant until the middle of the incoming tributary ($x/W = 0$), followed by a sharp decline in water depth over the second half of the tributary width. The gradient of the water depth profile for all flow ratios keeps increasing until the downstream corner. It is apparent that at the cross-section situated at the downstream confluence corner ($x/W = 0.5$) the gradient is maximum for all q. Furthermore, in this same cross-section the water depth for all flow ratios are equal, and also very close to the downstream water depth. Downstream of the confluence corner, for all q but the lowest value of q =0.083, the water depth keeps decreasing. The downstream section where the minimum depth is reached depends on the flow ratio, and slightly increases with increasing values of q. After this minimum value the section-averaged water level increases again, to finally reach the downstream water level. Although the water levels have not yet fully reached the downstream water level at the most downstream sampled section ($x/W = 3.25$), the recovery is almost completed. Even though Fr is higher for the experiments in the new flume, the uniformization appears to be completed faster than in the existing flume. This is, however, just a matter of relative scales, since the water depths vary with the velocity head, and thus relatively decline faster when compared to the velocity profiles.

The overall shape of the free surface profiles in figure 4.8 is quite similar for the different flow ratios. It appears that it is mainly a matter of increasing amplitudes (i.e increased ratio of up- to downstream water depth). Over the width, the water surface in the confluence is, however, highly heterogeneous in both directions, as could be seen in figure 4.7.

Therefore, figure 4.9 and figure 4.10 show longitudinal profiles near

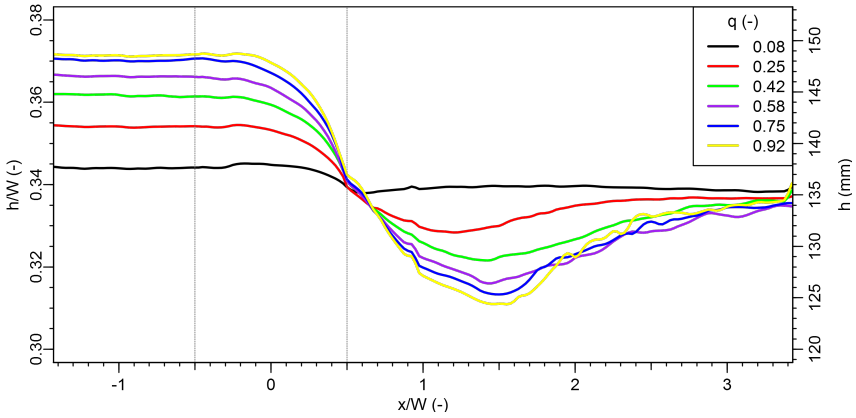

Figure 4.8: Section-averaged water depths along the main channel, presented in dimensionless form (relative to the channel width W, left vertical axis) and dimensionfull (right vertical axis).

the inner ($y/W = 0.04$) and outer ($y/W = 0.96$) wall. In contrast to figure 4.8, water levels have been made dimensionless with the water level difference between up and downstream. As seen in figure 4.8, differences in the shape of the section-averaged longitudinal profiles are small, and therefore if they are made dimensionless with the water level difference, they almost perfectly coincide. This allows to draw the averaged (i.e over all q values) non-dimensional cross-sectionally averaged profile as a reference. This reference profile is drawn in grey line in figure 4.9 and figure 4.10 .

The most apparent difference between the outer and inner wall is situated downstream of the tributary inflow. While the outer wall profile shows a gradual decrease in water depth from up to downstream, the inner profile has a very sharp gradient at the downstream corner (x/W =0.5). The latter decrease in water level is caused by the flow separation at the downstream corner. Looking at the profiles along the inner wall, it is clear that for all flow ratios but q =0.083, the separation zone is mostly horizontal, and the recovery of the water level towards downstream starts at about x/W =1.5. This is also the location where the decrease in water level along the outer wall stops, and the flow recovery starts. Comparison of the different profiles to the cross-sectionally averaged profile in grey

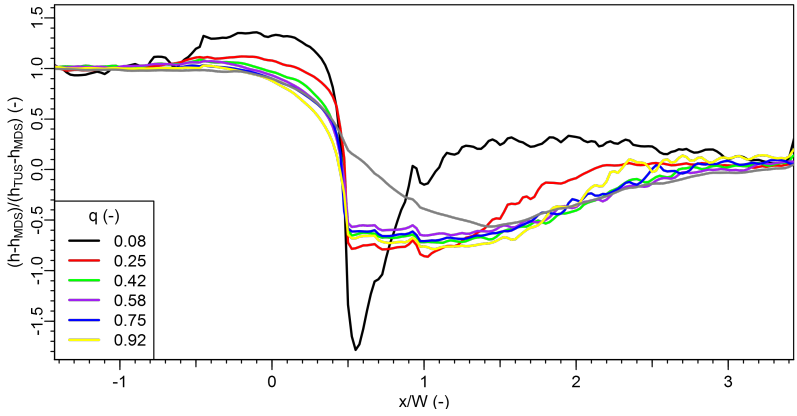

Figure 4.9: Water depth difference profiles (with the downstream water depth) near the inner wall (y/W=0.04) of the main channel. Water depth differences have been made dimensionless with the increase in water depth between up and downstream.

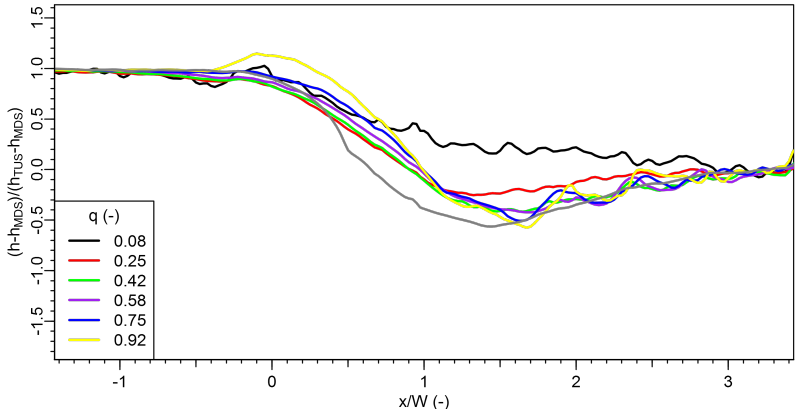

Figure 4.10: Water depth difference profiles (with the downstream water depth) near the outer wall (y/W=0.96) of the main channel. Water depth differences have been made dimensionless with the increase in water depth between up and downstream.

line further clarifies this difference between inner and outer wall.
Comparing different profiles for different q, the lowest discharge ratio clearly is different from the rest. The inner wall profile shows that the relative increase in water level near the stagnation zone is larger, and the separation zone almost has no horizontal part, which might indicate that it is very small or non-existent for this flow ratio. Also for q =0.25 small deviations from the profiles at higher q are still perceivable. At the outer wall, the profile for $q = 0.083$ is again different since there is a monotonously decreasing water level present, and no undershoot followed by a final recovery is observable. For q =0.92, the shift of the stagnation zone towards the outer wall, as observed in figure 4.7, is very clearly present. Where for all the other flow ratios water levels in the upstream main channel only decrease, a very pronounced increase in water levels is observable for q =0.92 at $x/W = 0$.
For $q > 0.25$, a pattern of standing waves is perceivable in the flow recovery zone. Although the cause for this phenomena is unknown, it is clearly present. While the wavy pattern in the profile for q =0.083 is due to small fluctuations in the recorded water levels because of measurement precision, this is not the case for the wave pattern observed for these higher flow ratios. Their absolute magnitude is at least one order of magnitude larger, and is recorded very consistent.
In figure 4.11, experimentally obtained longitudinal water level profiles at $y/W = 0.167$ and $y/W = 0.833$ for q=0.25 and 0.75 are compared to the results from Weber et al. (2001). In general, the experimental data sets correspond well over the entire confluence zone. The largest discrepancy observed is situated in the surface depression near the main channel inner wall. The current measurements show slightly higher levels for q=0.25, while slightly lower values are predicted for q=0.75.
A first reason for the discrepancies could be the difficulties in accurate manual measurements of water levels (the measurement methodology that was adopted by Weber et al. (2001)) which are fluctuating because of turbulent effects. Capillary forces result in a water surface that sticks to the measurement needle, resulting in subjective errors. The differences between both data sets is in the order of a mm, an order of magnitude that could well be attributed to those effects.
A second potential reason for differences is the limited movement speed of the automated measurement needle in the vertical direction. The fast undulations of the water surface combined with the measurement methodology might result in a slight bias towards higher water levels. This bias is, however, estimated to be one or two orders lower than mm's. Further-

more, in figure 4.11 no consequent bias towards higher water levels with the traverse system is observed, thus it is unlikely this is the cause of the observed differences. Given these considerations, the correspondence between the data sets is fair, and the experimentally obtained high density water level measurements can be considered to complement the velocity measurements presented in Weber et al. (2001).

4.5.3 Pressure force in tributary direction

As seen in figure 4.9 and figure 4.10, downstream of the downstream confluence corner a significant difference between the water levels at both the main channel walls is present. The difference between the hydrodynamic pressures on both walls results in a net pressure force in the direction of the tributary, since the water levels at the main channel outer wall are higher than those at the inner wall. It is this pressure force that counterbalances the incoming momentum flux from the tributary.

Expression of the balance in the y-direction results in :

$$P_{TUS} + M_{TUS} + P_{MIW} = P_{MOW} + F_{body} + F_{shear} \tag{4.2}$$

where P indicate the pressure forces, M the momentum flux term, and F the additional forces that act on the fluid. Subscripts indicate the applicable wall or cross-section indicated in figure 1.3. Making abstraction of the frictional force (low roughness) and other forces in the control volume (horizontal bed, other body forces are estimated to be small), equation (4.2) shows that the differential pressure force between the main channel walls has to make a balance with the incoming momentum flux and the pressure force on the TUS.

The net pressure force per unit width acting between the boundaries of the control volume at a certain x-location can be calculated as:

$$\Delta p(x) = \begin{cases} \frac{\rho g}{2}(h^2_{MOW}(x) - h^2_{MIW}(x)) & x/W < -0.5 \\ \frac{\rho g}{2}(h^2_{MOW}(x) - h^2_{TUS}(x)) & -0.5 \leq x/W \leq 0.5 \\ \frac{\rho g}{2}(h^2_{MOW}(x) - h^2_{MIW}(x)) & 0.5 < x/W \end{cases} \tag{4.3}$$

In figure 4.12 this net pressure force per unit width is represented in a dimensionless way, by division by the average pressure force per width on the main downstream section $\frac{P_{MDS}}{W}$. For clarity, the sidewalls of the

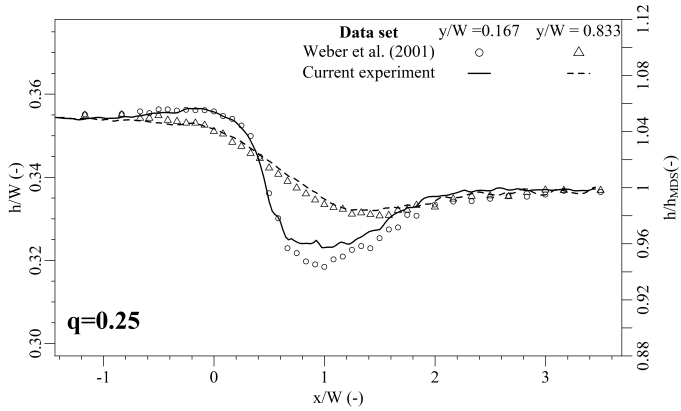

(a)

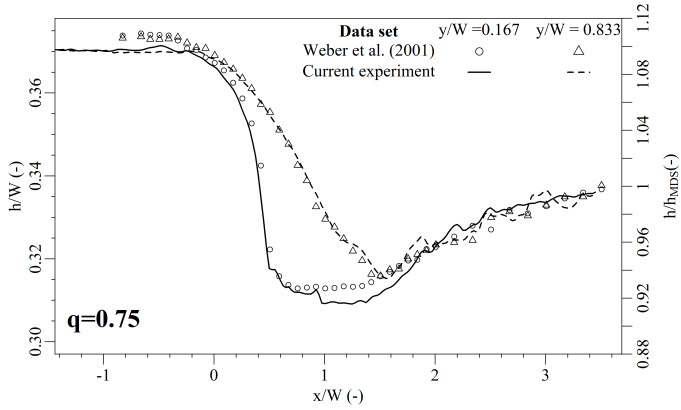

(b)

Figure 4.11: Comparison of the experimentally obtained water depths between the current study and the measurements by Weber et al. (2001).

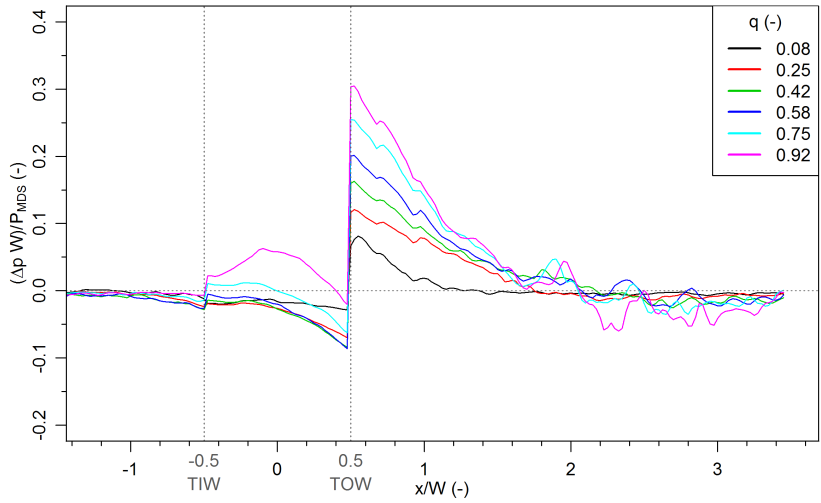

Figure 4.12: Relative differential pressure over the control volume in the y-direction (direction of the tributary).

tributary channel are indicated in grey dotted line. Furthermore, the horizontal grey dotted line indicates the zero net pressure, to illustrate where the net pressure accelerates the incoming flow from the tributary (negative values) and where it decelerates/counterbalances the incoming tributary momentum flux (positive values). For each of the flow ratios the net pressure contribution shows two discontinuities, located at the x-location of the tributary walls. This is a consequence of the sudden change of relevant water depth, going from the water depth at the MIW to the water depth in the TUS. In both cases the pressure contribution just downstream of the tributary wall is higher than just upstream of the that wall.

Near the upstream corner the water depth in the stagnation zone is higher than h_{TUS}, thus resulting in the sudden increase in value. Near the downstream corner, the water depth in the separation zone is (significantly) lower than h_{TUS}, resulting in the large discontinuity in the net pressure graph at $x/W = 0.5$.
In the upstream branch of the main channel ($x/W < -0.5$), the magnitude of the net pressure is small. It is, however, clearly negative for

all flow ratios, indicating an acceleration of the flow towards the MOW. This is what causes the flow contraction towards the MOW, and the flow stagnation zone near the upstream corner. In the confluence zone ($-0.5 < x/W < 0.5$) the overall net pressure contribution is mainly negative, with small magnitudes near the upstream corner, and increasing magnitudes towards the downstream corner. This indicates that the flow coming from the tributary is experiencing an acceleration towards the MOW, contrary to what might be expected. Only for high flow ratios (q=0.75 and q=0.95) the net pressure shows positive values at some locations, decelerating the incoming flow. Largest positive magnitudes of the net pressure for all the flow ratios are observed just downstream of the downstream corner, monotonously decreasing towards zero values at about $x/W = 1.5$. This is the same transect where the surface depression associated with the separation zone was ending, and the final recovery towards the downstream depth was beginning.

4.5.4 Depth ratios

In order to parameterize the most important free surface effects in the confluence, some depth ratios have been expressed in the literature.

The most documented and important one is the up- to downstream water depth ratio. Since head losses can cause important backwater effects in the entire upstream part of the network, they have been studied on multiple occasions. Figure 4.13 shows the depth ratio for both the tributary and main channel upstream section. The increase in ratio with q is clearly visible, with a maximum value for $q = 0.75$. For the extreme discharge ratio of q=0.92, a slightly lower depth ratio is observed, indicating that the maximum increase in water depths is found for flow rates between q=0.58 and 0.92. A second clear observation is the small differences between the main upstream to downstream ratio (red) and the tributary upstream to downstream ratio (black). This was already established by Hsu et al. (1998) for measurements at higher Froude numbers ($\approx$0.6), but is clearly also present for the Froude number adopted in the current study. Although it is common to assume that the two ratios are more or less equal, a clear evolution in their relative values with q is observable.

Additionally, some depth ratios related to local effects have been defined, such as the ratio of the depth in the separation zone to the downstream water depth (expressing the severity of the local surface depression), as defined by Gurram et al. (1997). This depth ratio is shown in

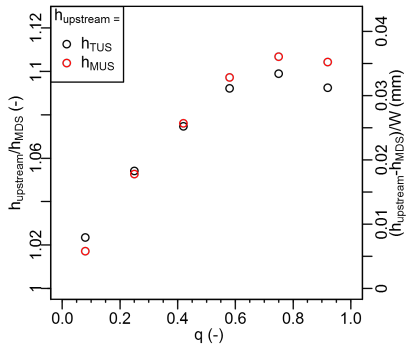

Figure 4.13: Ratio of up- to downstream water depth for different q (left vertical axis). Relative increase in water level made dimensionless with the channel width W (right vertical axis).

figure 4.14. With increase in q, the relative depth of the separation zone is decreasing more or less linearly. In comparison with the empirical model of Gurram et al. (1997), the current values are slightly lower. This might be caused by a different (lower) Froude number in the current experiments compared to the Froude numbers going up to 1 in Gurram et al. (1997).

A third depth ratio is defined as the ratio of water depths between the two tributary walls at the most downstream point. For a 90° confluence, this reduces to the ratio between the water depths at the downstream to the upstream corner. This ratio is represented in figure 4.15. It is clear that the transversal slope over the tributary increases with increasing q, showing the effects on the tributary water depths caused by the confluence also increase with q. Comparison with the values predicted by the empirical model of Gurram et al. (1997) indicate that the model (again) slightly overestimates the ratio for the current experiments.

4.5.5 Turbulent water level fluctuations

So far, in this chapter, the time-averaged results of the water level measurements were presented. These time-averaged values were calculated by averaging 30 measurements taken at a frequency of about 2 Hz. This was done to obtain time-convergence of the averaged values. However, the set of measurements also allows to calculate an estimate of the magnitude of

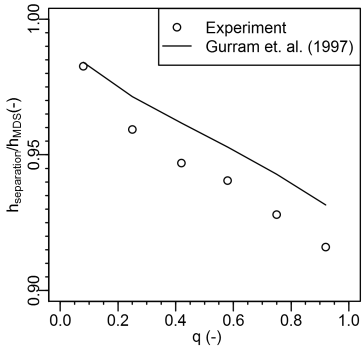

Figure 4.14: Ratio of minimum water depth in the separation zone vs. downstream water depth for different q.

unsteady fluctuations of the free surface. While the number of samples is not adequate to obtain time-averaged values of the standard deviations (SD), it is indicative to outline the locations with the highest amount of fluctuations. In figure 4.16, the standard variations of the recorded water levels are shown. In all cases, the separation zone shows the highest values, with increasing amplitudes for increasing q. With increase in q, the zone of maximum values also seems to shift slightly downstream. Observing the maximum values of the standard deviation reaching values up to 0.01 W. To calculate the maximum expected deviations, a normal distribution of the surface variations is assumed. This leads to a maximum deviation of 2.5 SD, or 0.025 W, which corresponds to almost 10 percent of the water depth at some locations.
The slightly elevated levels of surface turbulence for q=0.08 in the main channel originate from the upstream inlet. By application of a very thin sheet of Polyurethane at the inlet (just downstream of the inlet structure) at the free surface, these oscillations were suppressed. With increasing values of the lateral influx, at q=0.58 the same issues appeared, and also the inlet of the tributary was adapted. Although these modifications were not required to obtain accurate time-averaged values, they were introduced to make the data on time dependent fluctuations of the surface as valuable as possible. These mitigation issues were checked to have no influence on the time-averaged values of the water depths.

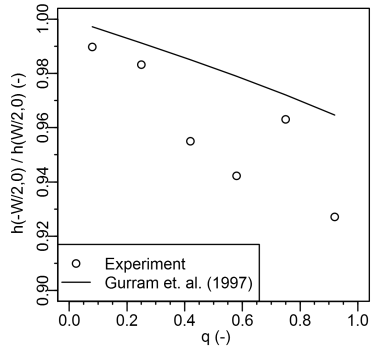

Figure 4.15: Ratio of water depth at the downstream to the upstream corner for different q.

4.5.6 Conclusion

In this chapter, the free surface elevations for different flow ratios have been recorded. To facilitate these measurements, and to be able to perform them in optimal conditions, a new flume was built. The new flume has been constructed to be as widely applicable as feasible, for this and further confluence research. Special consideration was put into designing the inflow structures, to ensure adequate control over the upstream boundary conditions. To accurately record the free surface elevations, and to allow a dense measurement grid with sufficient repetitions, a measurement robot was constructed. The robot uses a digitally sampled gauging needle, and as such is able to automatically sample the region of interest. The infrastructure described above allowed to record high density, accurate recordings of the free surface, for different flow ratios. The obtained fields of free surface elevations clearly show different distinct features, that can be related to the classical flow features encountered in confluence flow. Moreover, the measurements can be used in the following chapter, to validate the proposed model for the flow in the tributary.

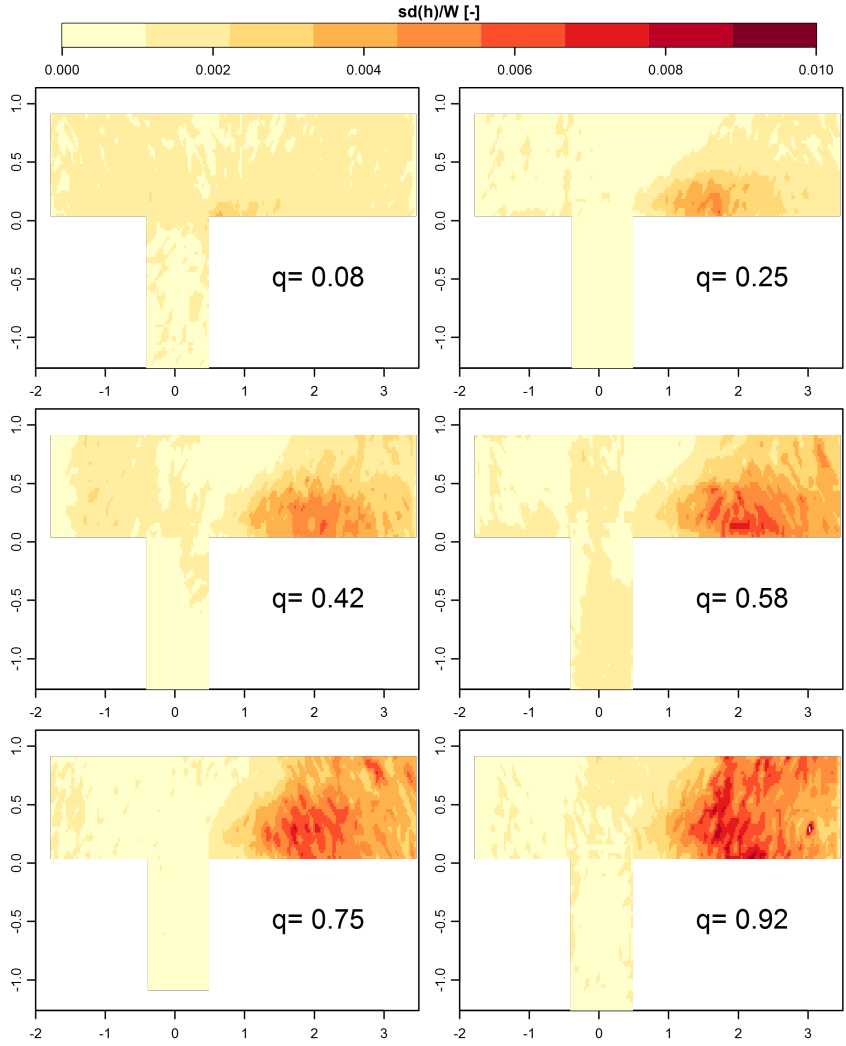

Figure 4.16: Non-dimensional standard deviation (SD) of the experimentally sampled water depths

Chapter 5

Theoretical modelling of the tributary hydrodynamic processes

This chapter is largely based on the paper by Creëlle et al. (2017), supplemented with validation efforts based upon the measured data presented in chapter 4. The orientation of the x-axis differs from the one in the previous chapters since this is more convenient for the analysis to have an x-axis that is positive in the direction of increasing radius of curvature of the streamlines in the tributary.

5.1 Modelling of the tributary velocity profiles

In chapter 2 the velocity field in the tributary of the confluence was found to be disturbed by the confluence. The strong change in flow direction, and the flow contraction result in alteration of the flow upstream of the confluence as well. In the tributary, the flow contracts towards the downstream corner, and decelerates at the opposite side, towards the stagnation zone. This goes along with a curvature of the streamlines, towards the downstream corner. Although some studies already mentioned upstream disturbances (Weber et al., 2001; Webber and Greated, 1966; Hager, 1989), only some qualitative descriptions or empirical formulations

to express the non-uniformity are available. In this section, a theoretical model for the velocity profile in the tributary is developed, based on the insights in the flow obtained from the experimental efforts.

5.1.1 Modelling assumptions and conventions

The modelling of the tributary flow profile will occur based on the conservation of momentum. The control volume considered extends from the MDS to the TUS and the MUS, as indicated in figure 5.1. Notice that the TDS and TCS coincide for the case of a $\theta = 90°$ confluence, and for the remainder of this work this chapter will be referred to as the TDS. Within this work a few - commonly made - assumptions **(a)** are made:

(a1) All channels have a rectangular shaped cross section with width W;

(a2) The entire confluence bed is concordant, fixed and horizontal;

(a3) In the MUS, the TUS and the MDS, the flow is uniform (with velocity magnitudes U_{MUS}, V_{TUS} and U_{MDS}, respectively) and the water surface is horizontal (with water depths h_{MUS}, h_{TUS} and h_{MDS}, respectively), resulting in a momentum correction coefficient $\beta = 1$ for these sections;

(a4) The friction losses at the walls and the beds can be neglected;

(a5) The pressure distributions are hydrostatic in the sections and along the walls considered;

(a6) The upstream water depths are equal: $h_{TUS} = h_{MUS}$;

(a7) The flow is subcritical throughout the confluence.

5.1.2 Free vortex profile and development of the streamline curvature

The flow from the tributary has to change direction when merging with the main channel flow. Most of this directional change is observed in the confluence hydrodynamics zone. However, as observed in the streamline plot in chapter 3, also in the upstream part of the tributary the streamlines show a curvature. This has also been observed in the literature in both experimental observations (Weber et al., 2001) as well as from theoretical derivations (Modi et al., 1981; Webber and Greated, 1966).

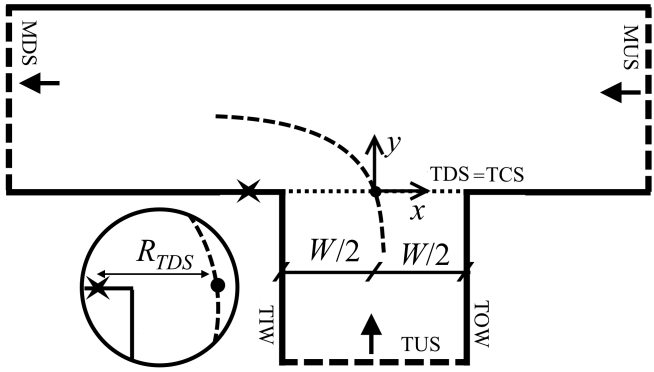

Figure 5.1: Definition of Cartesian coordinate system and radius of curvature R_{TDS} (in insert) for the 90° confluence.

Analysis of a validated 3D-RANS numerical model (Creëlle et al., 2014) showed the same behaviour of streamline curvature in the TDS. Further evidence was found in several papers displaying results of 2D and 3D simulations, (e.g. Dorđević (2014); Ghostine et al. (2010); Mignot et al. (2012); Zhang et al. (2009)). Actually, the aforementioned phenomenon is similar to what takes place in a curved open channel near the transition between the straight channel and a subsequent circular bend (see e.g. De Vriend (1972); Mockmore (1944); Rozovskiĭ (1957) and references therein). Despite the discontinuous geometrical curvature at the transition, the curvature of the streamlines in the straight channel gradually builds up from a zero value towards the finite value of the circular bend. This flow curvature distribution is accompanied by a gradual transition from a uniform velocity distribution towards a free vortex like velocity profile at the instream section of the bend, yielding higher velocities near the inner bend as compared to the outer bend.

The similarities with the flow upstream of a circular bend in a straight open channel are exploited to model the flow in the tributary channel of a confluence. Assuming the head losses to be zero in the tributary **(a8)**, the velocity distribution at each cross section upstream of the TDS features a free vortex profile (De Vriend, 1972; Rozovskiĭ, 1957):

$$v(x,y) = \frac{C(y)}{R(x,y)} \tag{5.1}$$

where C is a measure for the circulation in the given cross-section and R is the radius of curvature in the centre of the considered cross-section. The centre of curvature for each cross-section is assumed to be located on the same vertical plane (i.e. having the same y-coordinate as the cross-section) **(a9)**. This enables to express the curvature in a section as:

$$R(x,y) = R(0,y) + x = R(y) + x \tag{5.2}$$

Introducing the local dimensionless curvature :

$$\kappa(y) = \frac{W}{2R(y)}, \tag{5.3}$$

the flow curvature in the tributary is described by an exponential function:

$$\kappa(y) = \kappa_{TDS} e^{\frac{y}{\lambda}} \tag{5.4}$$

where $\kappa_{TDS} = \kappa(0)$ denotes the curvature in the centre of the TDS. The foregoing relation (equation (5.4)) was derived by Olesen (1987) in the framework of curved open channel flow. By a linearization of the governing equations, and neglecting friction losses, Olesen (1987) found a length scale for the adaptation of the flow curvature: $\lambda = W/\pi$. The same value is adopted in this work **(a10)**. Note that due to the exponential decay, the flow curvature at a distance of two channel widths upstream of the TDS (i.e. at $y/W = -2$) is already more than 500 times smaller than in the TDS. Situating the TUS at this location - a common choice in the literature (Hsu et al., 1998; Lin and Soong, 1979; Pinto Coelho, 2015) - thus leads to consistency with the assumption **(a3)** of a straight and uniform flow at the TUS. Calculation of the velocities in the tributary with equation (5.1) requires an expression for $C(y)$. To this end, mass conservation is expressed in the tributary. Integration of the velocity profile $v(x,y)$ and the water depth profile $h(x,y)$ over any cross-section, should yield the flow rate Q_{TUS} :

$$Q_{TUS} = qQ_{MDS} = \int_{-W/2}^{W/2} v(x,y)h(x,y)dx \tag{5.5}$$

Within this work, the head losses between the TUS and TDS are neglected **(a8)**, and thus the total head is constant and equal to H_{TUS}. Consequently, the water depths can be calculated once the velocity head is known:

$$h(x,y) = H_{TUS} - \frac{1}{2g}[(u(x,y)^2 + v(x,y)^2] \tag{5.6}$$

Substituting equation (5.6) and equation (5.1) into equation (5.5) results in the following cubic equation for $C(y)$:

$$\begin{aligned} Q_{TUS} = C(y)H_{TUS}ln\left(\frac{1+\kappa(y)}{1-\kappa(y)}\right) + \\ \frac{C(y)^3\kappa(y)^2}{gW^2}\left[\frac{1}{(1+\kappa(y))^2} - \frac{1}{(1-\kappa(y))^2}\right] \end{aligned} \tag{5.7}$$

Introducing the definition of the total head in the TUS yields:

$$\begin{aligned} Q_{TUS} = C(y)h_{TUS}ln\left(\frac{1+\kappa(y)}{1-\kappa(y)}\right) + C(y)\frac{V_{TUS}^2}{2g}ln\left(\frac{1+\kappa(y)}{1-\kappa(y)}\right) \\ + \frac{C(y)^3\kappa(y)^2}{gW^2}\left[\frac{1}{(1+\kappa(y))^2} - \frac{1}{(1-\kappa(y))^2}\right] \end{aligned} \tag{5.8}$$

Since $C(y) \approx V_{TUS}R(y)$ - a result which derives from linearization of the free vortex velocity profile equation (5.1) around the centre of the cross-section - equation (5.8) can be reformulated:

$$\begin{aligned} Q_{TUS} = C(y)\left\{h_{TUS}ln\left(\frac{1+\kappa(y)}{1-\kappa(y)}\right) + \frac{V_{TUS}^2}{2g}\left[ln\right.\right. \\ \left.\left.\left(\frac{1+\kappa(y)}{1-\kappa(y)}\right) + \frac{1}{2}\left(\frac{1}{(1+\kappa(y))^2} - \frac{1}{(1-\kappa(y))^2}\right)\right]\right\} \end{aligned} \tag{5.9}$$

Since it is assumed that (i) the flow in the entire confluence is subcritical **(a7)** and (ii) the flow is contracting towards the contracted section (which goes along with negligible head losses (Hager, 1989)), the velocity at the downstream corner is certainly not higher than in the contracted section (see also (5.1.3)). Moreover, the water depth in the contracted section is equal to or lower than in the tributary. Therefore, the following expression holds:

$$\frac{V(-W/2,0)}{\sqrt{gh_{TUS}}} \leq 1 \tag{5.10}$$

Making use of the free vortex profile in equation (5.1), with the abovementioned approximate value for $C(y)$ and the definition of the dimensionless curvature in equation (5.3), equation (5.10) becomes:

$$\frac{V_{TUS}}{(1-\kappa_{TDS})\sqrt{gh_{TUS}}} \leq 1 \tag{5.11}$$

Since $\kappa_{TDS} \geq \kappa(y)$ in the tributary (i.e. values of $y < 0$ which is the range where the model is valid) , the following relation for the ratio of velocity head to water depth in the TUS (which is equal to $Fr^2_{TUS}/2$) can be derived from equation (5.11):

$$\frac{V^2_{TUS}/2g}{h_{TUS}} \leq \frac{1}{2}\left(1-\kappa(y)\right)^2 \tag{5.12}$$

With the latter constraint, it can be proven (numerically) that the first term in between the curly brackets of equation (5.9) is an order of magnitude larger than the second term, and as such the latter term can be neglected. Therefore, $C(y)$ can be determined in good approximation by the following linear relation in $C(y)$:

$$Q_{TUS} = C(y)h_{TUS}ln\left(\frac{1+\kappa(y)}{1-\kappa(y)}\right) \tag{5.13}$$

yielding:

$$C(y) = \frac{Q_{TUS}}{h_{TUS}ln\left(\frac{1+\kappa(y)}{1-\kappa(y)}\right)} = \frac{V_{TUS}W}{ln\left(\frac{1+\kappa(y)}{1-\kappa(y)}\right)} \tag{5.14}$$

With equation (5.2), equation (5.3) and equation (5.14), equation (5.1) can be reformulated:

$$\frac{v(x,y)}{V_{TUS}} = \frac{2\kappa(y)}{ln\left(\frac{1+\kappa(y)}{1-\kappa(y)}\right)\left(1+2\kappa(y)\frac{x}{W}\right)} \tag{5.15}$$

Since $\lim_{\kappa(y)\to 0} ln\left(\frac{1+\kappa(y)}{1-\kappa(y)}\right) = 2\kappa(y)$, the right-hand side of equation (5.15) approaches unity for increasingly small values of the curvature, which should be expected.

5.1.3 Initial curvature at the confluence-tributary interface

Determination of the initial curvature κ_{TDS} is the final requirement to be able to apply the model. In case experimental results for confluence flows are available, appropriate values for κ_{TDS} can be readily found. Also (higher dimensional) numerical modelling can be applied to compute κ_{TDS} (Dorđević, 2014). Both approaches lead to empirical values of κ_{TDS} for the case at hand.

To model as much of the flow as possible, in this work, the assumption **(a11)** is introduced that the streamline separating from the downstream corner (delineating the separation zone), is a Helmholtz free streamline. Note that the latter assumption is commonly introduced in conformal mapping methods, see e.g Modi et al. (1981). This assumption states that the velocity along the free streamline is constant. Since the free streamline starts at the downstream corner, and goes into the contracted section (that is assumed to have a uniform velocity U_{MCS}), the corner velocity is also equal to U_{MCS} . Consequently, the ratio ϕ of the corner velocity to the velocity in the contracted section is equal to one. This assumption provides the required additional equation to calculate the initial curvature κ_{TDS}, based on the evaluation of equation (5.15) at the downstream corner ($x/W = -0.5$):

$$\phi U_{MCS} \equiv v\left(-W/2, 0\right) = \frac{2\kappa_{TDS}}{ln\left(\frac{1+\kappa_{TDS}}{1-\kappa_{TDS}}\right)} \frac{V_{TUS}}{1+\kappa_{TDS}} \tag{5.16}$$

where $\phi = 1$ and $U_{MCS} = Q_{MDS}/(h_{MCS}\mu W)$.
The velocity ratio ϕ is introduced as a parameter in equation (5.16), because in reality, the water depth can slightly decrease towards the contracted section, resulting in an increased velocity in the contracted section, and thus a value of ϕ lower than one. At this point, the parameter ϕ can be used as a model parameter, to implement empirical knowledge (obtained from numerical or experimental insights) into the model, and fine-tune the outcome as such.

Empirical values for the velocity ratio ϕ can be calculated from several papers in the literature, by application of the free vortex velocity profile and optimizing the value of phi to obtain a best fit. Measurements by Weber et al. (2001) for $q = 0.75$ result in a value of $\phi = 0.82$, while numerical results for the same flume for $q = 0.25$ result in a value of $\phi = 0.92$ (Huang et al., 2002). Experimental data presented in Mignot

et al. (2012) for $q = 0.5$ result in $\phi = 0.76$, while measurements performed by Gurram et al. (1997) (q is unknown) result in $\phi = 0.72$. Therefore, values of ϕ seem to lie in the interval [0.7;1].

It is also possible to obtain values of κ_{TDS}, based on the water depths recorded in chapter 2. By best-fits of the theoretical water depths (employing equation (5.6) derived in the following sections and performing a least-squares calibration of κ_{TDS}) to the experimental data, values of κ_{TDS} can be obtained. For the current experiments the values of ϕ are also found to be in the interval [0.7;1], with a value of $\phi = 0.75$ as a best fit for all measurements combined.

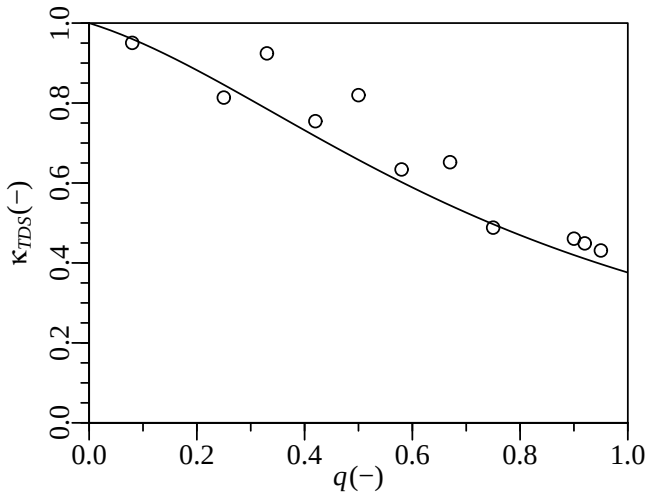

Figure 5.2: Dependency of κ_{TDS} on the flow ratio. Points represent values of κ_{TDS} obtained by best-fit from the presently experimentally measured surface levels. The full line is the theoretical curve obtained from equation (5.16) with $\phi = 0.75$.

In figure 5.2 the open circles represent the values of κ_{TDS} obtained from the experimental surface level data. Although the experimentally obtained values of κ_{TDS} are somewhat sensitive to measurement inaccuracies and the exact definition of the error metric, a clear dependency of κ_{TDS} on q is obtained. Values near unity are found for very low q, and values below 0.5 for high tributary flow. In figure 5.2, the full line represents calculated values of κ_{TDS} based on equation (5.16) with ϕ=0.75.

For this value of ϕ, the theoretical model lies well within the spread of the experimental results, and thus the theoretical model based on the velocity at the downstream corner performs as well as an empirical fit to the data, and thus should be preferred over empirical formulations.

Further investigation into the initial curvature and more accurate modelling could lead to better results of the model. Yet, as will be demonstrated below, reasonable modelling of the tributary momentum contribution is already possible by adopting assumption **(a11)**.

5.1.4 Validation

With the values for κ_{TDS} determined, the velocity profiles in the tributary can be calculated with eqs. (5.2), (5.3), (5.15) and **(a10)**. Since this section is focused on assessing the performance of the governing equations of the proposed model, values of κ_{TDS} are chosen to obtain the best fits for those specific cases. This is done because the required data to correctly estimate values of κ_{TDS} are not available in all experimental data sets. Using the currently obtained value of $\phi = 0.75$ could also have been a possibility, but this could lead to less accurate predictions, because it might be an inaccurate value for that set of experiments. Since the main goal is to validate the overall model performance, selection of the κ_{TDS} values that give the best fits is methodologically the best choice for model validation on the experiments in literature.

By predicting the velocity profiles, the streamlines in the tributary can be modelled. Figure 5.3 shows a comparison between the streamlines predicted by the proposed model and those predicted by a 3D numerical model (Zhang et al., 2009), for both a low tributary flow ($q = 0.25$) and a high tributary flow ($q = 0.75$) case. The streamlines predicted by the proposed model correspond well, especially considering they are following from a 1D+ modelling effort. For comparison purposes, also the streamlines drawn with conformal mapping in Webber and Greated (1966) are shown, albeit for a slightly higher value of $q = 0.33$. Their predicted streamline contraction, however, seems to be substantially higher, and higher values of κ_{TDS} would be required to obtain a better fit. Yet, higher q values should go along with lower values of κ_{TDS} . It thus seems that conformal mapping overestimates the streamline contraction towards the downstream corner.

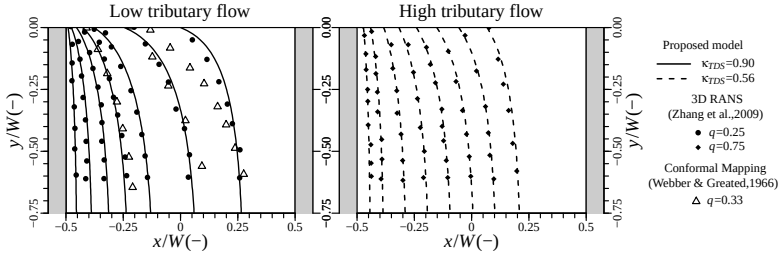

Figure 5.3: Validation of streamlines in the tributary predicted by the proposed model by comparison with 3D numerical simulations (Zhang et al., 2009) and conformal mapping (Webber and Greated, 1966).

5.2 Theoretical model to calculate confluence head losses: incorporation of a model for tributary flow patterns

5.2.1 Conservation of momentum approaches for confluence head loss calculations

Several authors (Gurram et al., 1997; Hager, 1989; Hsu et al., 1998; Shabayek et al., 2002; Taylor, 1944; Webber and Greated, 1966) have applied the principle of (streamwise) momentum conservation over a control volume to predict the head losses at an asymmetric open channel confluence, consisting of a straight main channel and a tributary. In all these works it was noticed that the prediction of the momentum contribution of the tributary branch was of paramount importance. The goal of the present section is to provide an overview of the different approaches in modelling this tributary momentum contribution.

Writing the momentum balance in the direction of the main channel over the control volume represented by the dotted line in figure 1.3 yields:

$$M_{MUS} - M_{MDS} + M_{TUS}cos\theta = P_{MDS} - P_{MUS} - P_{TUS}\ cos\theta - (P_{TIW} - P_{TOW})sin\theta \tag{5.17}$$

in which θ denotes the geometrical confluence angle, M represents the streamwise momentum flux term through an open boundary of the control volume and P is the pressure force exerted on a vertical boundary of the control volume.

The last term of the right hand side is the tributary momentum contribution caused by the pressure differences over the tributary walls. The water depth differences that are the source of pressure difference follow from the respective accelerations and decelerations at the TOW/TIW. A model for the tributary pressure term has been reported in the literature several times, based on different theoretical hypotheses or experimental measurements. Taylor (1944) assumed that the water depths along the TOW and TIW were uniform and equal to h_{TUS} , leading to the following expression for the tributary momentum contribution:

$$(P_{TIW} - P_{TOW})sin\theta = -\frac{\rho g h_{TUS}^2 W}{2tan\theta} sin\theta = -\frac{\rho g h_{TUS}^2 W}{2} cos\theta \quad (5.18)$$

This formula resulted in good predictions for experiments in a $\theta = 45°$ confluence flume, but a lower accuracy was observed in a $\theta = 135°$ configuration. Later experiments (Webber and Greated, 1966) for an extended set of angles indicated that for increasing confluence angles, the model accuracy decreased. However, by evaluating the last term in equation (5.17) by means of experimentally obtained values from pressure taps along the tributary walls, the model accuracy increased significantly. Consequently, it was confirmed that equation (5.17) gives accurate results, provided that the tributary wall pressure term is evaluated correctly. Moreover, with the help of conformal mapping, Webber and Greated (1966) found a streamline deflection towards the TOW, also observed in the experimental recorded data in chapter 2. Therefore, they concluded that local water depths at the TOW decrease, while they increase near the TIW. As such, the assumption of a uniform water depth h_{TUS} over the channel walls is indicated as the source of the modelling inaccuracies, a remark also made qualitatively in the discussions following Taylor (1944). This effect becomes more and more pronounced for confluence angles θ closer to 90° . Furthermore, several authors (Hager, 1989; Hsu et al., 1998; Webber and Greated, 1966) noticed that at large angles between the tributary and the main channel, the inflow angle starts to deviate significantly from the physical confluence angle. Moreover, since the tributary is chosen perpendicular to the main channel, no momentum contribution from the TUS is present in equation (5.17), and any tributary momentum contribution is caused by the pressure differences over the tributary walls, introduced by the streamline contraction.

For 90° angle confluences, several empirical relations for the tributary momentum contribution have been developed. A model based on direct

pressure measurements at the tributary walls was presented by Ramamurthy et al. (1988):

$$(\frac{P_{TIW} - P_{TOW}}{M_{TUS}}) = \frac{1-q}{q} \tag{5.19}$$

Other relations were derived by Hsu et al. (1998) and Hager (1989), through measurements of the flow angles in the TDS. By adopting a different, rectangular control volume, extending from the MUS to the MDS, flow angles α in the TDS are indeed required in order to calculate the tributary momentum contribution, since they differ from the physical confluence angle $\theta = 90\ ^\circ$. With the aforementioned rectangular control volume, the momentum balance in the streamwise direction becomes:

$$M_{MUS} - M_{MDS} + M_{TDS}\ cos\alpha = P_{MDS} - P_{MUS} \tag{5.20}$$

Combining eqs. (5.17) and (5.20) for the case of $\theta = 90^\circ$ leads to:

$$M_{TDS}\ cos\alpha = P_{TIW} - P_{TOW} \tag{5.21}$$

Assuming no change in momentum flux in the tributary direction is present between the TUS and the TDS **(a12)**, Hsu et al. (1998) conjectured that:

$$M_{TDS}\ sin\alpha = M_{TUS}\frac{M_{TUS}}{tan\alpha} = P_{TIW} - P_{TOW} \tag{5.22}$$

The latter formula can then be combined with a relation for the tributary inflow angle α, like e.g. the one proposed by Hager (1989) :

$$\alpha = \frac{8}{9}\theta \tag{5.23}$$

or the one proposed by Hsu et al. (1998):

$$\alpha = acos[0.149 + 0.914(1-q)] \tag{5.24}$$

Referring to the control volume presented in figure 1.3, the tributary momentum contribution can be obtained by integrating the pressure difference over the tributary walls. Following **(a5)**, knowledge of the wall pressures follows directly from the water depth along the walls. Since for θ=90° the wall normal velocity component u is zero at the walls TIW and TOW, knowledge of the wall parallel velocity component v along the tributary walls leads to knowledge of the pressures, hence allows the calculation of the tributary momentum contribution.

5.2.2 Water depths in the tributary based on conservation of head

Application of the model for the velocity profiles in the tributary, the water depths in the tributary can be modelled. Substituting equation (5.15) in equation (5.6) yields:

$$h(\pm W/2, y) = H_{TUS} - \frac{V_{TUS}^2}{2g} \frac{4\kappa(y)^2}{ln(\frac{1+\kappa(y)}{1-\kappa(y)})^2 (1 \pm \kappa(y))^2} \tag{5.25}$$

This can be expressed as the multiplication of a factor and h_{TUS}:

$$h(\pm W/2, y) = h_{TUS} \left[1 + \frac{Fr_{TUS}^2}{2} \underbrace{\left(1 - \frac{4\kappa(y)^2}{ln(\frac{1+\kappa(y)}{1-\kappa(y)})^2 (1 \pm \kappa(y))^2} \right)}_{A\pm} \right] \tag{5.26}$$

where the factor $A\pm$ (which is multiplying $(\frac{Fr_{TUS}^2}{2})$ has been introduced for the sake of brevity. The resultant force - caused by the difference in pressure between the inner and outer wall - can be calculated as:

$$P_{TIW} - P_{TOW} = \int_{-\infty}^{0} \frac{\rho g}{2} h(W/2, y)^2 - \frac{\rho g}{2} h(-W/2, y)^2 dy \tag{5.27}$$

Substituting equation (5.26) into equation (5.27) for the resultant force - caused by the difference in pressure between the inner and outer wall of the tributary - yields:

$$P_{TIW} - P_{TOW} = \frac{\rho g h_{TUS}^2}{2} \int_{-\infty}^{0} \left[\left(1 + \frac{Fr_{TUS}^2}{2} A_+ \right)^2 - \left(1 + \frac{Fr_{TUS}^2}{2} A_- \right)^2 \right] dy \tag{5.28}$$

$$P_{TIW} - P_{TOW} = \frac{\rho g h_{TUS}^2}{2} \int_{-\infty}^{0} \left[Fr_{TUS}^2 (A_+ - A_-) - \frac{Fr_{TUS}^4}{4} (A_+^2 - A_-^2) \right] dy \tag{5.29}$$

Using equation (5.11), which is a constraint for Fr_{TUS} , it can be numerically proven that the magnitude of the second term between square brackets in equation (5.29) is at maximum 4% of the first one, and thus can be neglected. Since

$$\rho g h_{TUS}^2 Fr_{TUS}^2 = \frac{M_{TUS}}{W} \tag{5.30}$$

equation (5.29) then can be reformulated as:

$$P_{TIW} - P_{TOW} = \frac{M_{TUS}}{W} \int_{-\infty}^{0} \frac{2\kappa(y)^2}{ln\left(\frac{1+\kappa_{TDS}}{1-\kappa_{TDS}}\right)^2} \left[-\frac{1}{(1+\kappa(y))^2} + \frac{1}{(1-\kappa(y))^2} \right] dy \tag{5.31}$$

Changing the integration parameter to κ and making use of eqs. 5.4 , 5.3 and 5.31 leads to:

$$P_{TIW} - P_{TOW} = \frac{\lambda}{W} M_{TUS} \int_{0}^{\kappa_{TDS}} \frac{2\kappa^2}{ln\left(\frac{1+\kappa}{1-\kappa}\right)^2} \left[+\frac{1}{(1-\kappa)^2} - \frac{1}{(1+\kappa)^2} \right] \frac{d\kappa}{\kappa} \tag{5.32}$$

$$P_{TIW} - P_{TOW} = 8\frac{\lambda}{W} M_{TUS} \int_{0}^{\kappa_{TDS}} \left[\frac{\kappa}{ln\left(\frac{1+\kappa}{1-\kappa}\right)} \right]^2 \frac{1}{(1-\kappa^2)^2} d\kappa \tag{5.33}$$

No closed form expression is known for the integral appearing in the foregoing equation. Therefore, an approximation is derived, involving a factor B:

$$P_{TIW} - P_{TOW} \approx 8\frac{\lambda}{W} M_{TUS} B \int_{0}^{\kappa_{TDS}} \frac{1}{(1-\kappa^2)^2} d\kappa \tag{5.34}$$

$$P_{TIW} - P_{TOW} \approx 4\frac{\lambda}{W} M_{TUS} B \left[\frac{\kappa_{TDS}}{1-\kappa_{TDS}^2} + \frac{1}{2} ln\left(\frac{1+\kappa_{TDS}}{1-\kappa_{TDS}}\right) \right] \tag{5.35}$$

By numerical integration, B as a function of κ_{TDS} can be retrieved. Subsequently, a compact approximation to this function is sought. It turns out that:

$$B \approx \frac{1}{4}(1-\kappa_{TDS}^2)^{0.275} \tag{5.36}$$

is a good approximation in a wide range of κ_{TDS} values. For $\kappa_{TDS} < 0.9$ (i.e. $R_{TDS}/W > 0.56$) the approximation only differs less than 2% from the exact value, while for higher values of κ_{TDS} the tributary momentum contribution is negligible in the overall momentum balance. Using equation (5.36) in equation (5.35) leads to:

$$P_{TIW} - P_{TOW} \approx \frac{\lambda}{W} M_{TUS}[1-\kappa_{TDS}^2]^{0.275}[\frac{\kappa_{TDS}}{(1-\kappa_{TDS}^2)} + \frac{1}{2} ln(\frac{1+\kappa_{TDS}}{1-\kappa_{TDS}})] \tag{5.37}$$

Either an accurate numerical solution of the exact integral in equation (5.27) - with the use of equation (5.25) - or the approximate form in equation (5.37) can be used to predict the tributary momentum contribution. Application of the approximate form has a computational advantage, but introduces some additional errors. Since the head losses will be calculated by means of an iterative procedure, a combined use of both approaches can be adopted, i.e. using equation (5.37) during the first iteration and only utilizing equation (5.27) in the later iterations.

5.2.3 Depth and width of the contracted section

Calculation of κ_{TDS} with equation (5.16) requires knowledge of μ and h_{MCS}. By expressing the conservation of energy (Hager, 1989) between the MUS, the TUS and the MCS, and introducing the water depth ratio $Y_s = h_{MUS}/h_{MCS}$ the contraction coefficient μ can be determined with the insertion of **(a6)**:

$$H_{MCS} = qH_{TUS} + (1-q)H_{MUS} \tag{5.38}$$

$$H_{MCS} = q\left(Y_s h_{MCS} + \frac{\mu^2 q^2 h_{MCS}}{2Y_s^2}\frac{Q_M DS^2}{q\mu^2 W^2 h_{MCS}^3}\right) + (1-q)\left(Y_s h_{MCS} + \frac{\mu^2 (1-q)^2 h_{MCS}}{2Y_s^2}\frac{Q_M DS^2}{q\mu^2 W^2 h_{MCS}^3}\right) \tag{5.39}$$

$$H_{MCS} = Y_s h_{MCS} + \frac{\mu^2 h_{MCS} Fr_{MCS}^2}{2Y_s}[q^3 + (1-q)^2] \tag{5.40}$$

Substituting $H_{MCS} = (1 + \frac{Fr_{MCS}^2}{2})$ in equation (5.40) yields:

$$\frac{2Y_s^2}{Fr_{MCS}^2[q^3 + (1-q)^3]}(1 + \frac{Fr_{MCS}^2}{2} - Y_s) = \mu^2 \tag{5.41}$$

$$\mu = \frac{Y_s}{Fr_{MCS}}\sqrt{\frac{2(1 + \frac{Fr_{MCS}^2}{2} - Y_s)}{q^3 + (1-q)^3}} \tag{5.42}$$

Expressing the momentum conservation between the MCS and the MDS yields:

$$\frac{\rho g h_{MDS}^2 W}{2} - \frac{\rho g h_{MSS}^2 (1-\mu) W}{2} - \frac{\rho g h_{MCS}^2 \mu W}{2} = \frac{\rho Q_{MDS}^2}{\mu W h_{MCS}} - \frac{\rho Q_{MDS}^2}{W h_{MDS}} \tag{5.43}$$

Note that no net momentum flux term for the separation zone is present in equation (5.43). As long as the downstream Froude number Fr_{MDS} is limited (< 0.5), it can be assumed that **(a13)** $h_{MCS} = h_{MSS}$ (Gurram et al., 1997). Consequently, U_{MCS} can be calculated from equation (5.42) and equation (5.43). Subsequently, equation (5.16) can be applied to obtain κ_{TDS}.

5.2.4 Solution routine

In the previous paragraphs, a set of equations was provided, based on several modelling efforts and assumptions, to model the flow in the confluence tributary. In figure 5.4 an overview is given of the solution routine to apply the model. The required equation numbers and assumptions introduced are shown in a comprehensive diagram, to facilitate usage of the model.

5.3 Validation of the theoretical model

In the previous section, the theoretical model for the tributary velocity profiles proposed in section 5.1 was used to model the head losses over the confluence. In the process, also the tributary momentum contribution, the water depths along the tributary walls, contracted section and separation zone, as well as the width of the separation zone are calculated as intermediate results of the model. In the current section, a thorough validation of the model is performed, comparing the model results to data found in

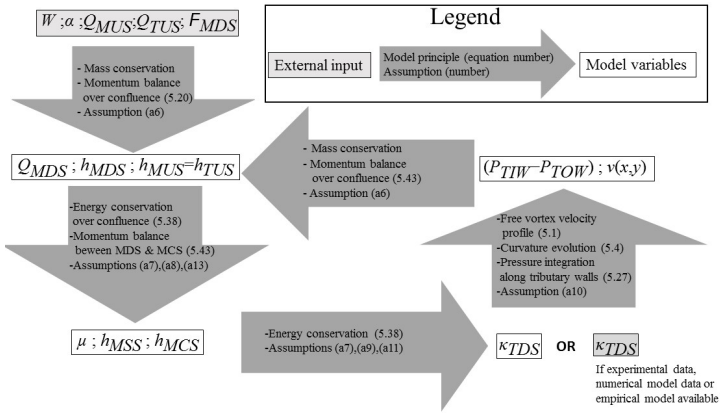

Figure 5.4: Schematic representation of the basic equations, variables and assumptions for the proposed model.

the literature, as well as data obtained in the experiments performed in chapter 2 and chapter 4. Furthermore, the findings are compared to as many of the available empirical models in literature as possible.

5.3.1 Contraction coefficient

The contraction coefficient is calculated with equation (5.42) and equation (5.43). When using assumption **(a11)** and equation (5.16) to obtain values of κ_{TDS} , μ is even required to calculate the tributary momentum contribution. Figure 5.5 shows a comparison of the predictions by the proposed model for the conditions of different experimental data sets, as well as the appropriate empirical models.

First, it is noted that the conformal mapping approach of Modi et al. (1981) severely underestimates the contraction coefficient. This shows that the conformal mapping approach, with the free streamline assumption, leads to overestimation of the flow contraction. This is in line with the comparison of the streamlines, where the solution of the potential flow also overpredicted the streamline contraction towards the downstream corner. As such, the finding that the velocity ratio should take values below 1, as also concluded in section 5.1, is confirmed. The values of Best and Reid (1984), which pertain to a range of Froude numbers $Fr_{MDS} = [0.1; 0.3]$,

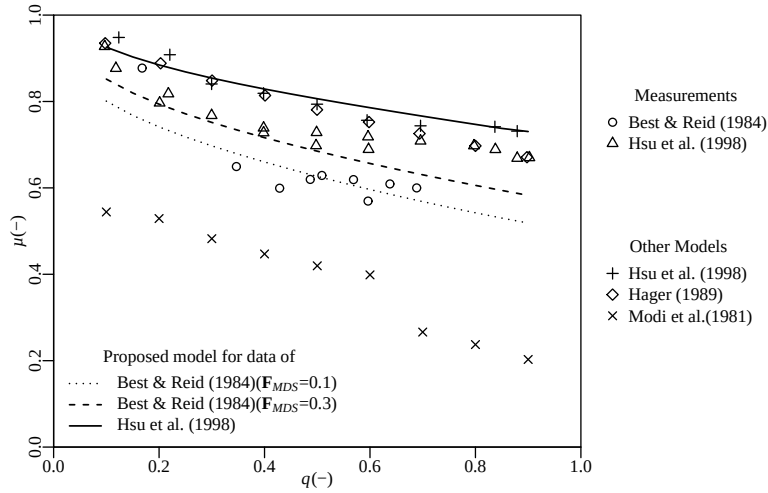

Figure 5.5: Comparison of contraction coefficients predicted by proposed model with experimental values and predictions by other models

seem to be reasonably well predicted by the model when adopting the lower limit value (i.e. $Fr_{MDS} = 0.1$), while the predictions making use of the upper limit (i.e. $Fr_{MDS} = 0.3$) overestimate all the data by Best and Reid (1984). Also for the measurements by Hsu et al. (1998) the proposed model seems to somewhat overestimate μ. It can be seen that the predictions lie very close to the points predicted by the empirical formula of Hager (1989). This is logical, since a variation on Hager's derivation was used to predict the contraction coefficient. In figure 5.6 the values of the contraction coefficient measured in chapter 2 are compared to the results of the proposed model. The agreement is found to be relatively good. The discrepancy starts to increase for larger values of q. A probable cause for this observation is the shape of the separation zone, that starts to be wider at the top than at the bottom, an effect that is amplified with increasing discharge from the tributary (Weber et al., 2001). As noted in the discussion of the experimentally obtained values of the contraction coefficient, the determination of the contraction coefficient is difficult, and the different methodologies applied in different studies suffer from different issues, leading to a larger spread on the obtained values of μ. Therefore, the model seems to perform well, considered the low dimensional modelling

approach, and the spread on the experimental data.

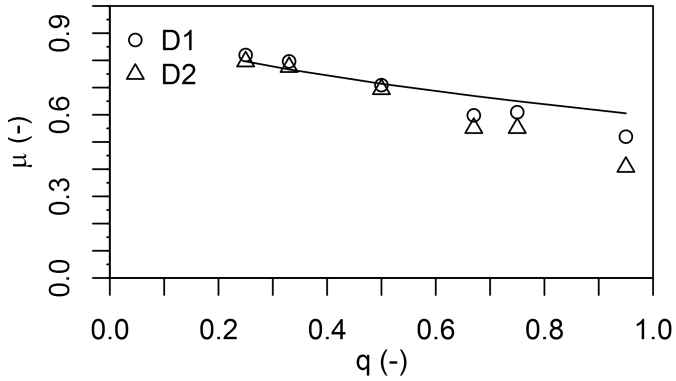

Figure 5.6: Comparison of contraction coefficients predicted by proposed model with experimental values obtained from the velocity data in chapter 2. D1 presents the results from the streamline definition, D2 from the zero net discharge method.

5.3.2 Water depth in the separation zone

Because of the flow contraction, the water depth h_{MCS} in the contracted section is lower than in the downstream section. Also in the separation zone a local surface depression, with water depth h_{MSS} is present. In figure 5.7 a full line shows the values of h_{MCS}, predicted by the proposed model. To obtain experimental observations of h_{MCS} from the surface level measurements, values of μ are required, to delineate the MCS and MSS. This is, however, no information that can be deduced from the surface level measurements, and for those cases, no velocity information is available. Therefore, the values of μ as predicted by the proposed model are used. This allows to calculate experimental values of h_{MCS} and h_{MSS}, which are shown in figure 5.7 as points.

The values of h_{MCS} and h_{MSS} are found to be almost equal, as predicted by Gurram et al. (1997) for this downstream Fr. The differences are in the order of one percent maximum. The proposed model predicts the values of h_{MCS} very well. No differences other than small variations that are probably due to experimental uncertainty, are observable.

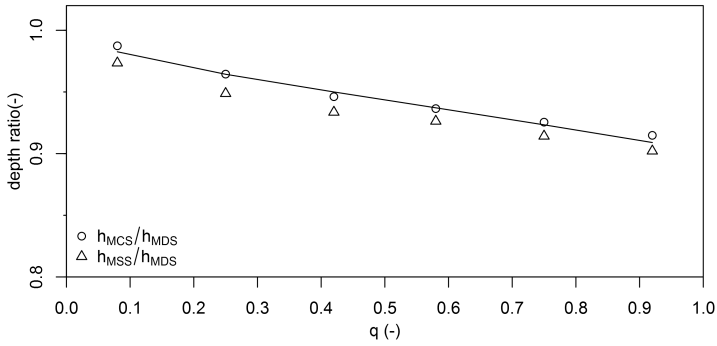

Figure 5.7: Ratio of water depths in the most contracted section (h_{MCS}) and in the separation zone (h_{MSS}) and the downstream water level (h_{MDS}) for different values of the flow ratio q. The full line indicates predicted values by the proposed model ($h_{MCS} = h_{MSS}$)

.

5.3.3 Water depth along the tributary walls

With the best-fit values of κ_{TDS}, the velocity profiles were successfully modelled in section 5.1. By expressing the conservation of head, and applying the model for the velocity profiles in the tributary, the water depths in the tributary can be calculated. A comparison of both longitudinal and transversal water depth profiles is presented in the following paragraphs.

5.3.3.1 Cross-sectional profiles

In figure 5.8 cross-sectional profiles are presented for q=0.25, 0.67 and 0.90. There is a good agreement between the experimental data and the theoretical profile from equation (5.6), especially for the higher q values. In the profile for q=0.25, the model slightly underestimates the level differences. However, for all flow ratios the shape of the predicted water level profile based on the free vortex profile and conservation of head matches the experimental results very well. It is noted that the transversal velocities are assumed to be low enough to neglect the influence of the transversal velocities on the velocity head. Both the experimentally

recorded velocities in chapter 2, as well as the good agreement between modelled and experimentally recorded water depth confirm the validity of this assumption. Furthermore, since one single value of κ_{TDS} is used to model the curvature in the entire tributary channel with the help of equation (5.4), the length scale of the development of curvature inspired by Olesen (1987) again proves to yield accurate results, as was the case for the velocity profiles. Since the current experiments allow to evaluate the water depths near the tributary corners (i.e. at y/W=0 , near $x/W \approx \pm$ 0.5), the formula of Gurram et al. (1997) for the corner to corner water depth ratio can be evaluated:

$$\frac{h(0.5,0)}{h(-0.5,0)} = 1 - q\mathsf{Fr} \tag{5.44}$$

For the current experiments this results in calculated ratios of 0.99, 0.98 and 0.97 for q=0.25 , 0.75 and 0.95, respectively. When comparing this with the values found from the experiments, the formula by Gurram et al. (1997) results in an overprediction of the corner to corner depth ratio (i.e. an underestimation of the transversal slope) for the current experiments. The ratio for e.g. q=0.95 in the current experiments is 0.92. A possible explanation for this observation could be found in the set-up of the experiments by Gurram et al. (1997), where the upstream branches seem to be quite short, and the presence of the upstream boundary might suppress the flow curvature development.

5.3.3.2 Longitudinal profiles

Supplementary to the cross-sectional profiles, longitudinal profiles in the tributary are shown in figure 5.9. As the flow curvature decreases with the distance from the confluence, the water level difference is found to decrease from a certain value at the tributary downstream section ($y/W = 0$) to zero at the tributary upstream section. The presented longitudinal profiles are profiles at $x/W = \pm 0.33$ for $q = 0.25, 0.42, 0.5, 0.58, 0.75$ and 0.9 respectively. While the agreement is again very good at high flow ratios q, for lower values of q the model again seems to underestimate the water level differences somewhat. Furthermore, data obtained by Weber et al. (2001) for q=0.25, 0.42, 0.58 and 0.75 along these longitudinal profile are shown in filled symbols for comparison purposes. These show that the general agreement between the data sets is good, but that for locations far upstream in the tributary ($y/W < -0.5$)) some differences seem to exist. Given it is unlikely that any significant water level differences exist

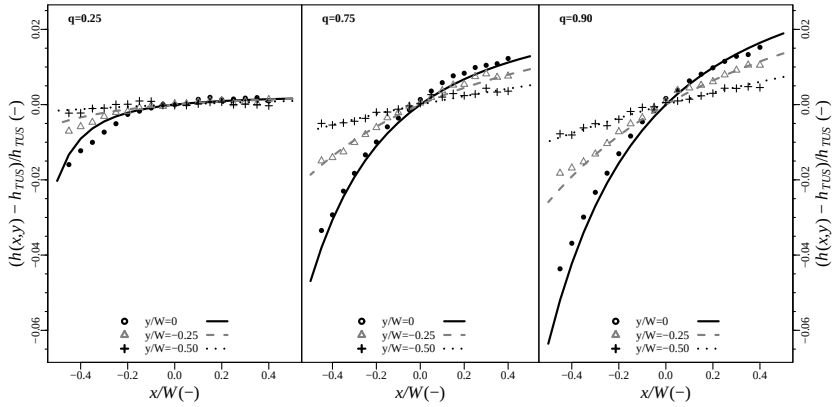

Figure 5.8: Comparison of measured and predicted water level differences in a selection of transects. Symbols represent values from the experiments. Predictions with equation (5.6) using best fit values of κ_{TDS}.

that far upstream, this is probably due to measurement inaccuracies in Weber et al. (2001).

5.3.4 Tributary momentum contribution

From the comparison of measured and predicted water depths in the previous section, the capability of the model to accurately predict the water levels in the tributary is established. With the predicted water depths, it is now possible to integrate the pressures over the tributary walls, and obtain the tributary momentum contribution. As outlined in the introduction of this chapter, the tributary momentum contribution is an important term in the overall momentum balance (equation (5.17)), and thus several empirical data sets and models are available. In this section the available data and models from the literature will be compared to the current experimental data, as well as the proposed model.

In the literature, two well described sets of experimentally obtained tributary momentum contributions are available. Ramamurthy et al. (1988) measured the momentum contribution of the tributary by pressure taps along the tributary walls. Therefore, the measurements of the resulting momentum contribution result from the difference of the pressure forces on the tributary walls. Hsu et al. (1998) measured the contribution

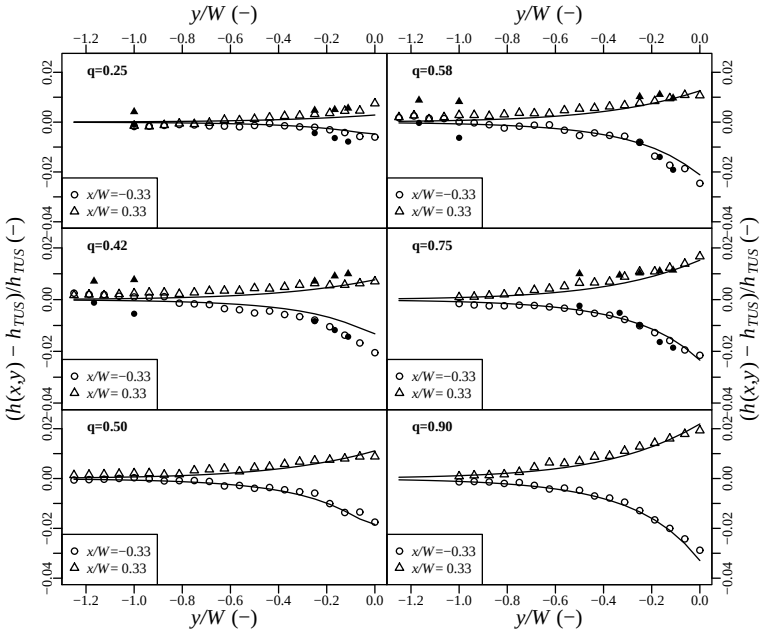

Figure 5.9: Comparison of measured (open symbols) and theoretically predicted (full lines) water level differences along the tributary at an off-centerline distance of $x/W = \pm 0.33$. For q=0.25, 0.42 , 0.58 and q=0.75 the available measurements from Weber et al. (2001) are represented (filled symbols).

of the tributary to the streamwise momentum balance by measuring the flow angles α and the velocities in the TCS. These are converted to a tributary contribution using equation (5.20). For the available data sets, no values of the velocity ratio ϕ are readily available. To check the influence of ϕ, the current model is applied with three values of ϕ, equal to 1, 0.7 and 0.85 for the measurements by Hsu et al. (1998). These correspond to the theoretical value obtained from the streamline definition ($\phi = 1$) , the lower limit found in literature ($\phi = 0.7$) and the average of both, respectively.

In figure 5.10 the momentum contribution from the tributary is presented as a function of the relative flow ratio q, comparing the data from the literature to the current model. As opposed to some other representations in the literature, $P_{TIW} - P_{TOW}$ is made dimensionless with M_{TUS}/q^2 instead of M_{TUS}. Since $M_{TUS}/q^2 = \frac{M_{MDS}h_{MDS}}{h_{TUS}}$, the obtained dimensionless number is a more direct measure of the relative importance of the momentum contribution of the tributary in the overall momentum balance.

In general, the predictions of the tributary momentum contribution by the proposed model show reasonable agreement with the experiments, although a systematic underestimation of the contribution is noticed, especially for the measurements by Ramamurthy et al. (1988). The most noticeable discrepancy is the failure of the model to predict the declining values for high values of q, as reported by Hsu et al. (1998). However, it appears that with increasing values of q, decreasing values of ϕ result in better results. This seems to be in line with the values for ϕ derived from the literature, that also showed a tendency to decrease with increasing values of q. It should be noted that the resulting curves are linked with the modelling assumption **(a11)** adopted in equation (5.16), and that a different approach to obtain κ_{TDS} (like e.g. using a value for κ_{TDS} that is tuned on experimental or numerical velocity fields near the TDS) can alter the shape of the presented curves. However, the validation of streamlines, velocity profiles and water depths showed the model was well capable of modelling the respective flow properties.

In figure 5.11, the tributary momentum contribution predictions by empirical models from the literature (Hager, 1989; Hsu et al., 1998; Ramamurthy et al., 1988; Shabayek et al., 2002) are compared to the predictions of the proposed model. Several distinct observations can be made. For low flow ratios the developed model yields results very close to the ones obtained by the formulae of Hsu et al. (1998) and Shabayek et al. (2002). While the model agreement with the latter remains high, the de-

clining values of the contribution for higher q, as modelled by Hsu et al. (1998), are again not predicted (as was already observed in figure 5.10). Furthermore, it can be seen that the models of Ramamurthy et al. (1988) and Hager (1989) predict respectively higher and lower values than the other models. It is reminded that in order to convert the original formulae for the flow angles in the TCS, as stated by Hsu et al. (1998) and Hager (1989), to a pressure contribution, some assumptions were introduced **(a6, a8)**. One should be aware that these assumptions might impact the predictions made by the formulae. It should also be noted that the formulation derived by Hager (1989) was obtained from experimental measurements in transcritical flow ($Fr_{MCS} = 1$). Furthermore, a remark has to be made on the formulation by Shabayek et al. (2002), since strictly speaking two contributions mentioned by Shabayek et al. (2002) are combined to represent the net tributary momentum contribution. The total incoming tributary momentum is first assumed to be integrally transferred into a main stream momentum contribution, and is subsequently reduced by a momentum loss to account for the presence of the separation zone. The net result is interpreted as the tributary momentum contribution modelled by Shabayek et al. (2002) and is presented in figure 5.11. Since this model for the tributary momentum contribution has proven to yield accurate head loss predictions (Kesserwani et al., 2008), and the tributary contributions predicted by the proposed model agree well with the ones of Shabayek et al. (2002), it is expected that the proposed model also yields accurate head loss predictions.

In figure 5.12, the experimental values obtained from the surface level data are presented, and compared to the modelling results. It should be noted that, because of mechanical constraints, the automated traverse could not record measurements closer than 15 mm ($4W/100$) from the side walls of the flume (see the description of the set-up in chapter 4. This means that the calculated values of the tributary momentum contribution is slightly underestimated. Therefore, also corrected values of the relative contributions are calculated. This is done by extrapolating the profiles with the individually fitted values of κ_{TDS}, and indicated in figure 5.12 with the empty diamond shapes. This allows to estimate the underestimation made by the unavailability of data at the channel walls, by comparing the directly calculated and corrected points in figure 5.12. The relative momentum contribution based on the theoretical model with ϕ=0.75 is calculated and represented with the full line. To facilitate comparison to the experimental data available in the literature, this data has also been added to figure 5.12. These are represented in grey symbols, to

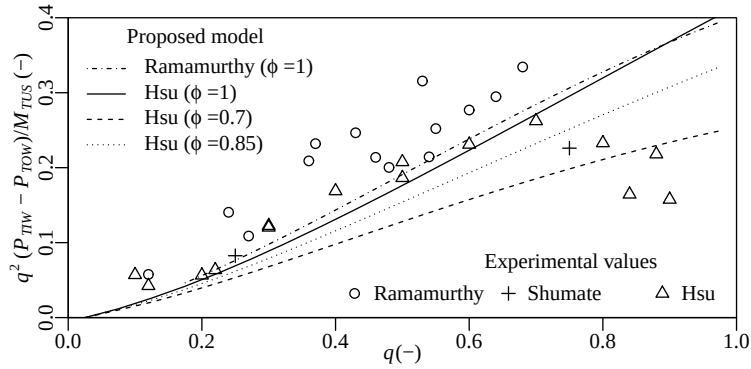

Figure 5.10: Comparison of measured and predicted relative momentum contribution from the tributary as a function of q for the experimental conditions of Hsu et al. (1998); Ramamurthy et al. (1988) and for different values of the velocity ratio ϕ.

keep the visual clarity of the figure.

Comparing the model to the directly calculated values of the tributary (black crosses), the agreement is good, but a slight overestimation by the theoretical model is observed. However, comparing the model results to the experimental results that were corrected for the distance of the measurement to the wall, the theoretical model performs very well, and variations are found to be within the experimental spread.

Comparing the results of the current experiments with values from the literature (Weber et al., 2001; Hsu et al., 1998), the current experiments clearly result in lower values, especially in the region $0.25 < q < 0.75$. The very sudden decrease in the tributary momentum contribution that was found by Hsu et al. (1998) at $q \approx 0.7$ is not present in the current data. This might indicate a dependence on the downstream Froude numbers. While the current experiments predict the lowest tributary momentum contribution, they were also performed at the lowest downstream Froude number Fr=0.37 , while the other experiments were performed at significantly higher Froude numbers (i.e. 0.6 and 0.8). The developed theoretical model predicts increasing tributary momentum contributions for increasing values of ϕ (see figure 5.10). Therefore, it is possible that the downstream Froude number also has implications for the initial curvature of the streamlines in the tributary.

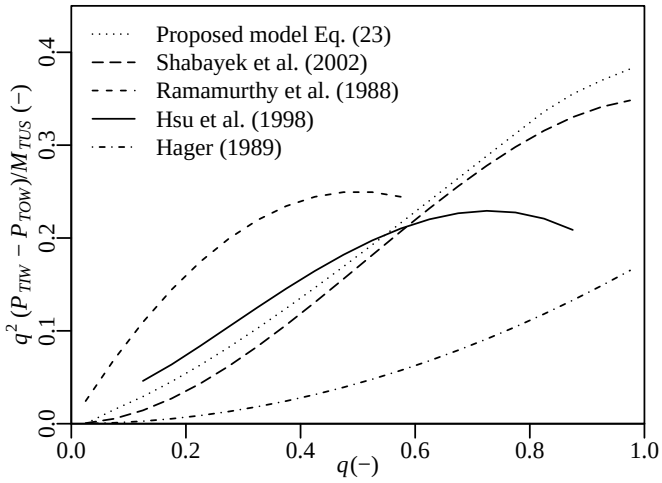

Figure 5.11: Comparison of the proposed approximate analytical model equation (5.37) ($\phi = 1$) with empirical relations from the literature for predicting the relative momentum contribution from the tributary.

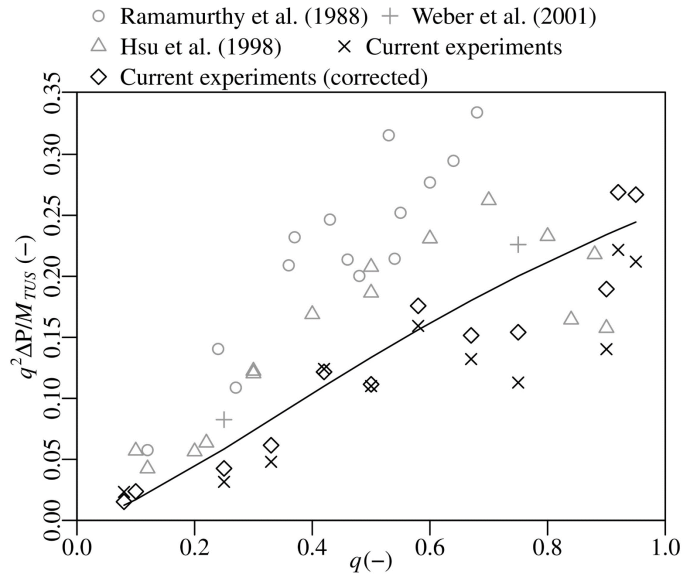

Figure 5.12: Relative momentum contribution from the tributary. Symbols in grey color represent values from other experimental works in the literature, black symbols present the results of the current study. Black crosses are calculated directly from the experimental data, while the diamond shapes are corrected values of the experimental data. The full black line presents the results predicted with the theoretical model of the current model, with a velocity ratio $\phi = 0.75$.

5.3.5 Confluence head losses

In a final validation step, the head losses over a 90° angle confluence are calculated with the presented model, and compared with experimental data available in the literature. As is common in the literature on experiments for such type of flows, the water depth ratio $Y = \frac{h_{MUS}}{h_{MDS}}$ will be reported, instead of the associated head losses. This is because experimental values of the up- and downstream head require both water depth and velocity measurements. Since one of the modelling assumptions is that the water depth in the MUS and TUS is uniform, it is more convenient to compare modelled and measured water depth ratios, than it is to compare head losses over the confluence. From the known (input) flow parameters, and the calculated water depth ratios, the corresponding head losses can then easily be calculated. Several authors have reported measurements of the water depth ratio for a large range of Froude numbers, flume dimensions and flow ratios. For these different data sets, the water depth increase over the confluence is calculated, and compared to the measured value. In general, for subcritical flow in the confluence, the water depth (difference) is made dimensionless with the downstream water depth. This is done for several measurements in the literature (Lin and Soong, 1979; Weber et al., 2001; Webber and Greated, 1966).

In Hsu et al. (1998), however, the values presented in the original paper were made dimensionless with the critical water depth $h_c = \sqrt[3]{\frac{Q_{MDS}^2}{W^2 g}}$. For reasons of uniformity, these data are converted to be dimensionless with respect to the downstream water depth as well, making use of $Fr_{MDS} = 0.6$. (The latter value is the average value of the reported range [0.59;0.61].) For the sake of simplicity, all calculations are performed with a value $\phi = 1$. When comparing measured with predicted water depths, it is important to keep in mind that the absolute differences in measured water depths are small (mm range). Moreover, the model results are quite sensitive to the accuracy of the measured flow rates and the Froude numbers (Gurram et al., 1997).

Figure 5.13 present the comparison between measured and predicted water depth ratios. It is clear that only a limited amount of points fall out of the 2 % error band, notwithstanding that the data set covers a large range in experimental conditions. Furthermore, the model was not adapted to any of the data sets, and the general value of $\phi = 1$ was used, which was seen to cause some minor deviations already. To assess the accuracy of the proposed model in an objective way, the prediction

Table 5.1: Errors on the estimation of the water depth ratio for the proposed model and two recently developed 1D and 2D models, in comparison to experimental data by Hsu et al. (1998) (18 measurements).

Model	Error (%)
1 D model (Ghostine et al., 2012)	3.5
2 D model (Ghostine et al., 2012)	≈1
Proposed model	0.7

Table 5.2: Errors on the estimation of the water depth ratio for the proposed model, in comparison to various experimental data.

Dataset	Error (%)
Webber and Greated (1966), 18 measurements	0.8
Lin and Soong (1979), 51 measurements	0.6
Weber et al. (2001), 4 measurements	0.3

error is quantified by means of the L_2 norm, similar to what was used in Ghostine et al. (2012):

$$Error = \sqrt{\frac{\sum_{i=1}^{n}(Y_{pred,i} - Y_{exp,i})^2}{\sum_{i=1}^{n} Y_{exp,i}^2}} \tag{5.45}$$

In table 5.1, the error of the present model is compared to the one of the other models, for the measurements of Hsu et al. (1998). The accuracy of the proposed model proves to be comparable to the performance of a 2D (depth-averaged) model (Ghostine et al., 2012). Therefore, the proposed model (which introduces theoretical modelling of the tributary flow in a 1D model formulation, based on the 2D flow patterns) can offer a valuable alternative to (full) 2D calculations of open channel confluences. As such, the general remark is confirmed that correct modelling of the tributary momentum contribution facilitates a correct prediction of the head losses by a momentum conservation approach. In table 5.2, the error of the present model is shown for other datasets. It turns out that the present model performs well over all datasets, although it has not been calibrated on the specific cases separately.

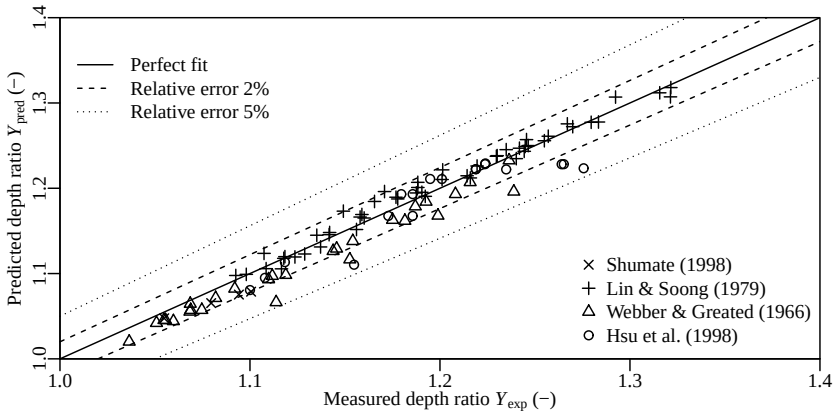

Figure 5.13: Comparison of measured water depth ratios $Y = \frac{h_{MUS}}{h_{MDS}}$ with predictions of proposed model.

5.4 Adaptation of the model for application outside of the modelling assumptions

The proposed model has been developed in a stepwise manner. Wherever needed to enable theoretical modelling, simplifying assumptions were introduced. When applying the model to real flows, however, it is likely that not all these assumptions are met. For the original assumptions **(a1-a7)**, some discussion on how to change the proposed model in case the assumptions are not met is provided below.

For the assumptions **(a1)** to **(a6)**, the proposed model can quite easily be adapted by changing a few of the modelling equations. In case not all channels in the confluence have identical rectangular sections, the different momentum contributions should be expressed in relation to their respective cross-sections, like e.g. investigated in Pandey and Mishra (2012). In case the bed has a non-zero bed slope, this effect can be accounted for by adding an additional term to the momentum balance, see e.g. Shabayek et al. (2002). If one of the inflow or outflow sections does not have uniform flow, momentum correction coefficients β should be introduced in the appropriate momentum flux terms. Furthermore, this can also affect the curvature development and as such potentially influence values of κ_{TDS} or λ. When the confluence angle is not 90° , the influence of the angle in

the momentum balance should be introduced in the momentum balance again. In that case, the developed model for the curvature development is probably still valid (indications can be found in Gurram et al. (1997) where the ratio of water depths at the most downstream section is shown to be more or less constant).

When the bed friction within the confluence has a significant influence, this effect can be added by introducing a momentum sink term in the overall momentum equation. For both the bed slope term and the friction term, the introduced terms in the momentum balance are of empirical nature. Indeed, both the water volume inside the control volume and the velocity field over the bed are highly heterogeneous and are evolving with both q and Fr, following the complex changes in free surface elevations as shown in chapter 4. All deviations from the above mentioned assumptions might also result in a (slight) change in the evolution of the streamline contraction in the tributary section. While the streamline contraction will surely remain present, it might be necessary to change the values of ϕ **(a11)** or λ **(a10)**. For instance, λ is known to change if friction effects become dominant (Olesen, 1987). Assumption **(a6)** has been frequently checked, based upon both experimental and numerical simulations, and was shown to be a reasonable approximation. Also in the current work (chapter 4) the ratio between both upstream flows was checked. A small variation with q was found, but for the overall balances, assumption **(a6)** was found to be appropriate. If desired, it is possible to compute the two upstream water depths separately, provided an additional equation is introduced, like e.g. performed in Shabayek et al. (2002). However, this requires an empirical value for the exchange of momentum between the two control volumes, which is difficult to obtain over a large range of flow conditions.

5.4.1 Adaptation of the methodology in case of critical flow in the MCS

In some confluence configurations, critical flow may occur in the contracted section, while the downstream flow still remains subcritical. Though the last initial assumption **(a7)** is violated in that case, the proposed model can be altered to account for such cases. Once critical flow in the MCS can be assumed, this introduces an additional known value in the problem solution. However, the water depths over the MCS and the MSS cross-sections cannot be assumed uniform anymore (i.e. **(a13)** is no longer valid). Consequently, a distinction is made between the water depth in

the contracted section h_{MCS} and the one in the separation zone h_{MSS}. Therefore, the pressure force on the MCS and the MSS can be calculated as:

$$P_{MCS} + P_{MSS} = \frac{\rho g \mu W h_{MCS}^2}{2} + \frac{\rho g (1-\mu) W h_{MSS}^2}{2} \tag{5.46}$$

Note that h_{MSS} is found to be lower than h_{MCS}, especially for higher tailwater Froude numbers Fr_{MDS} (Gurram et al., 1997). This behaviour was also observed in the performed measurements of the free surface, as illustrated in figure 5.7. As long as the flow is subcritical in the MDS, the water depth in the separation zone h_{MSS} can be calculated based on the empirical relation reported by Gurram et al. (1997), as their eq. (9) can now be reformulated by substituting the latter relation for h_{MSS}. In addition to this, the variable h_{MDS} appearing in the empirical relation will be rewritten as a function of h_{MCS} and Fr_{MCS}. To this end, the conservation of mass between the MCS and the MDS can be expressed, taking into account that $Fr_{MCS} = 1$:

$$h_{MDS} = \frac{h_{MCS} \mu^{2/3}}{Fr_{MDS}^{2/3}} \tag{5.47}$$

With the aforementioned substitutions, equation (5.46) can be reformulated as:

$$P_{MCS} + P_{MSS} = \frac{\rho g h_{MCS}^2 W}{2} \left[\mu + \frac{(1-\mu)\mu^{4/3}}{Fr_{MDS}^{4/3}} (1 - 0.6 \sqrt{q Fr_{MDS}^5} \right] \tag{5.48}$$

Consequently, the head losses for cases with a critical section can be calculated, as long as the tailwater Froude number Fr_{MDS} is known and is lower than one. For the dataset of Ramamurthy et al. (1988), the resultant L_2 error of the present model with application of equation (5.48) is 0.8 % for a comparison with 13 data points.

For cases where the flow remains supercritical after the contracted section, the water depth in the separation zone is very small, and its contribution to the momentum balance between the contracted section and the MDS can be neglected (Hager, 1989). In that case, the second term of the right-hand side in equation (5.46) can be neglected and no value for h_{MSS} is required, which removes the need to know the downstream Froude number Fr_{MDS} for calculating the head losses. Only a flow rate

Table 5.3: Errors on the estimation of the water depth ratio for the proposed model and two recently developed 1D and 2D models, in comparison to experimental data by (Hager, 1989) (15 measurements).

Model	Error (%)
1 D model (Ghostine et al., 2012)	6
2 D model (Ghostine et al., 2012)	1.5
Proposed model	1.3

q is required in that case. With the above-stated expressions, the head losses are computed and the resulting error for the dataset of Hager (1989) is again compared to 1D and 2D model results reported in the literature (table 5.3). The resulting error clearly indicates that the present model can also be applied to cases with transcritical flow, i.e. with critical flow in the MCS, provided that the other terms in the overall momentum balance can be accurately calculated as well.

Chapter 6

Conclusions and recommendations

In the current work, an in-depth investigation of the specific flow patterns at an asymmetrical open channel confluence has been performed. The overall objective of this work was to contribute to the understanding of these important nodes of the open channel network of rivers and canals, as well as to provide engineers and modellers with knowledge to better incorporate the effects of confluences in their designs. To meet the objectives, a three step approach has been taken.

6.1 Acquisition of experimental data sets (O1).

In accordance with the first objective **(O1)**, laboratory experiments have been performed, to obtain data with adequate resolution and spatial coverage for the validation of numerical models, as well as for a profound analysis of the flow. Two comprehensive data sets have been gathered in 90° asymmetrical flumes with concordant bed at the Hydraulic Laboratory, Department of Civil Engineering, Ghent University. Both data sets comprise measurements over a range of incoming flow ratios.

Data set of surface velocities A first data set contains the surface velocity data, measured in an existing flume in the laboratory. The flume with a chamfered rectangular shape and concrete walls was equipped with adequate inlet and outlet structures, to have the desired control

over the inlet. To obtain the surface velocities, a surface particle tracking velocimetry methodology has been developed and implemented. This technique allowed the measurement of the velocities at the large scale of the flume with adequate resolution, over a considerable distance up and downstream. These measurements have been performed at low Froude numbers (0.05) to obtain a quasi horizontal water surface. The obtained velocity fields clearly captured the desired flow features, and illustrated the complex change in flow field with changing flow ratio. The large sampling area employed within the measurements was found to be important, with the confluence flow patterns that influenced regions upstream of the confluence, as well as a considerable distance downstream.

Data set of water levels Because of the limited amount of data on surface levels in confluences in the literature, the acquisition of a high density, high accuracy data set of surface elevations was envisioned. For these measurements, a new flume was conceived and constructed at the Hydraulics Laboratory. The new flume was built for mainly two reasons. First, to allow a more flexible control of the boundary conditions. The new flume allows higher Froude numbers, required to obtain meaningful variations in the free surface levels. Second, the new flume was designed for flexible application for a lot of different tests. It is designed to maintain maximum visual access, as well as great modularity of the set-up, to allow tests in changing geometries (i.e. change of the confluence angle, bed discordance, ...). Moreover, thought was given towards convenient and accurate mounting of measurement equipment on the flume, to further facilitate high quality measurements.

To record the desired water levels, a measurement robot with automated gauging system was conceived. The robot allows an efficient measurement of a large amount of measurement points. By application of an electronically sampled gauging needle, high accuracy measurements of the free surface, without the subjective bias of manual measurements, could be recorded.

The flow conditions for the measurements of the free surface have been chosen to be a Froude scaled version of the measurements presented in Weber et al. (2001). Thus, the current water level measurements can complement the (mainly) velocity measurements presented in that study. As such, the usefulness of the combined data sets for numerical model validation is increased. Analysis of the obtained free surface elevations indicated the importance of free surface effects on the confluence flow in

general, even at the moderately high Froude numbers adopted. Incorporation (or exclusion) of these effects in numerical simulations thus should be well considered, and consequences of practical modelling choices on the model output should be critically evaluated.

6.2 Analysis of the different flow features that define confluence flow(O2).

Based on the acquired data sets, an in-depth analysis of the different flow features at an open channel confluence was performed. By identifying the different features in the highly detailed data, a step by step qualitative and quantitative description of the different flow features could be performed. This analysis led to the following conclusions:

- Size and shape of the separation zone are found to be highly dependent on the flow ratio. Depending on the adopted definition of the separation zone the obtained values for width and length can differ quite a lot.

- The location and shape of the stagnation zone greatly depend on the relative flow ratio. This can be observed in both measurements of the surface levels and in the surface velocity fields. For the first time a quantitative determination of the stagnation point location along the confluence walls was performed based on experimental data.

- Analysis of the shear layers in a natural coordinate system enables the study of the shear layers within the highly curved environment, and allows calculation of typical quantities related to more classical mixing layers.

- Mixing layer mode and wake mode behaviour of the central shear layer between the incoming flows is governed by the relative strength of two shear layers that exist at the boundaries of the stagnation zone, one at each side of the stagnation zone. Depending on the flow ratio, one of the two shear layers disappears, and the other one continues as the central shear layer.

- The strength of the central shear layer is less than would be expected based on the difference between the incoming velocities. Redistribution of the flow in the upstream channel parts diminishes the

velocity gradient over the central shear layer. The flow contraction in the confluence hydrodynamics zone results in a fast decrease of the velocity difference over this shear layers, resulting in a quite short observable length.

- In asymmetrical confluences, the separation shear layer shows a substantially higher initial velocity difference than the central shear layer. The most apparent turbulent structures appear in this shear layer, and they persist a longer distance downstream than the structures in the central shear layer.

- Upstream effects of both water depths and velocities are important to understand the overall confluence hydrodynamics. Simulation and analysis of flow patterns should start sufficiently far upstream to be able to correctly grasp these upstream effects.

- The strong curvature of the streamlines in the confluence hydrodynamics zone is building up in the flow approaching the confluence from the tributary branch.

6.3 Theoretical modelling of the flow to obtain engineering formulations(O3).

Following the quantitative analysis of the different confluence flow features based on the surface velocity flow field and the recorded water levels, the obtained insight is applied to analytically model the confluence flow. This modelling is performed to obtain accurate low dimensional models of the confluence behaviour, to be able to be applied in engineering calculation of networks of rivers and open canals.

Starting from the expression of the conservation of momentum, it was identified that the incorporation of the tributary momentum contribution in highly angled asymmetrical confluences is not yet described by a theoretical model, despite the importance. In case of highly angled asymmetrical confluences, the tributary momentum contribution is found to be mainly caused by the water level differences over the tributary walls. This has been established in the literature by measuring the pressures on the tributary side walls, leading to several empirical formulations of the tributary momentum contribution. To be able to have a more generally applicable model for this tributary momentum contribution, an analytical model based on modelling the flow is introduced. This has the

main advantage over the empirical models that it can be expanded to other flow cases. The developed model is based on the modelling of the depth-averaged velocity profiles in the tributary. By exploiting similarities between the development of the flow curvature upstream of a bended channel and in the tributary of a confluence, the velocity profiles can be modelled with a free vortex profile, provided a value of the streamline curvature at the tributary downstream section is chosen. This value can be provided from several sources such as measurements, numerical modelling, but also by the simplified approach presented in this work, in case no other information is at hand. By assuming the head losses in the tributary are negligible, an expression for the water depths in the tributary can be derived. Integration of these water depths, and expressing the difference between both tributary walls, leads to the desired expression for the tributary momentum contribution. Application of the expression in the overall momentum balance was shown to yield accurate prediction of the depth ratios of up- to downstream water levels for different experimental data sets, without any calibration on experimental data. Comparison to results published in the literature showed that the resulting accuracy of the 1D expression was in the same order as a 2D depth-averaged calculation of the tributary. As such, an analytical expression of the tributary momentum contribution for head loss calculations was developed, for incorporation in computationally feasible 1D network calculations.

6.4 Recommendations for further research

During the current experimental investigation of confluences, and the subsequent conceptual modelling, additional insight and engineering capabilities for open channel confluences were obtained. However, to be able to perform an in-depth analysis, some limitations were introduced restricting the amount of variable parameters. In order to generalize the results of this work, some additional work could be performed, which would expand the applicability of the proposed results.

Confluence angle The asymmetrical confluence within this work was assumed to have a 90° geometrical angle with the (straight) main channel. This choice was made since it presents a case with very strong tributary momentum influx, amplifying the effects studied. However, to generalize the findings within this work, experiments at different angles should be

performed to assess the influence on the properties of the different identified features such as the stagnation and separation zone, mixing layers and flow recovery zone. Also the validity of the proposed model for the tributary flow field should be examined for reduced angles between tributary and main channel. The new flume is designed to facilitate this research, which should enable to perform the required experiments.

Bed discordance Within this work, the confluence bed was assumed to be horizontal throughout. Because of the sediment transport capacity that suddenly changes at the confluence, in a lot of (natural) confluences a bed discordance is present. This severely impacts the flow in the CHZ. Expectation is that particularly the mixing layers will be impacted, since the bed discordance is known to generate a strong secondary flow, that influences the redistribution of the flow, and thus the mixing layers. However, with this larger secondary flow cells, the free surface, separation and stagnation zone will probably also be altered, and a rigorous analysis should be performed to enable generalisation of the findings in this work to cases with a discordant bed. These experiments are also enabled by the new flume. By application of a new confluence joining piece several discordance ratios can be tested to understand these effects.

Upstream velocity profiles While the incoming velocity profiles from the upstream sections were assumed to be uniform over the entire channel section, this will often not be the case. Upstream disturbances in planform (e.g a bend upstream of the CHZ) or in channel geometry can alter the incoming velocity profiles. This can in turn have an impact on the flow in the CHZ, and therefore it would be interesting to study the amount of impact a non-uniform upstream velocity profile has on the confluence flow, by e.g. mounting a bended flume section as a tributary, instead of a straight channel with uniform flow. These experiments could also be set up in the new flume, by coupling a part of the existing bend flume to the new flume, by application of an adapter piece.

Influence of bed roughness In the analysis of the data, and the conception of the engineering model, the bed roughness in the confluence was assumed to be low enough to be neglected. However, it is well possible that in some cases (riprap, vegetation, bed forms) the influence of the roughness is high enough to severely impact the flow field in the confluence. The effects of roughness can impact the confluence flow in several

ways. Upstream, a change in bed roughness changes the incoming vertical velocity profiles, adding heterogeneity to the flow over the vertical direction. The adaptation length formulation for the streamline curvature, used in the analytical model is known to change with roughness (Olesen, 1987), and thus will impact the incoming velocity profile in the horizontal direction, as well as the tributary momentum contribution. Within the confluence, the roughness is known to facilitate the change in flow direction near the bed, resulting in even higher vertical heterogeneity. This will all inevitably lead to a more heterogeneous form of the separation zone, and thus impact the flow recovery. Since it has an impact in so many different ways, it should be investigated to what extent the roughness alters the flow on a relevant scale, and when it is negligible.

Depth-to-width Ratio The experiments performed in both the existing and the new flume had a quite large depth-to-width ratio. This is typical for laboratory experiments, and is also the case for almost every other laboratory test in the literature. However, because of this high relative depth, large secondary structures can be formed, that would not be possible in case of a lower width-to-depth ratio. Since no velocity measurements in the bulk of the flow were performed, the influence of secondary structures on the experimental data is unclear. To better frame the current experimental results (but also the experiments in the literature) a study towards the influence of the depth-to-width ratio in confluence flow would be beneficial.

Turbulent fluctuations of the free surface Out of the multiple samples of the free surface that were taken, time-averaged quantities were calculated and presented. However, as indicated in the plots with the standard deviations of the water depth measurements, the water surface can locally be quite turbulent. It is also clearly observed that these regions coincide with regions with high turbulent fluctuations of the velocity. While in a lot of numerical models there is consideration on how to deal with the turbulent velocity fluctuations, turbulent fluctuations of the water depths are often overlooked. Even in eddy-resolving models such as Large Eddy Simulations, that aim to simulate the larger turbulent structures, often no turbulent fluctuation of the free surface is possible. Because it has not yet been investigated in depth, it would be interesting to assess the importance of the turbulent fluctuations of the free surface for the turbulent structures, and for the flow prediction in general.

Quantitative assessment of the importance of the free surface
In this work, the importance of the free surface gradients within the confluence has been indicated. However, no rigorous direct quantitative analysis of the importance of the free surface gradient on the momentum exchange throughout the confluence has been carried out. Therefore, to even better appreciate the role of free surface gradients, it would be beneficial to initiate an analysis starting from the Navier-Stokes equations, and do a term-by-term analysis of the different processes. This will require a first analysis of the required quantities, followed by an extensive measurement campaign. The outcome could be very beneficial for numerical modellers, since it would give more direct insight into which processes are relevant, and which can be omitted.

Additional illustrations

Contour plots of the experimentally obtained surface velocity data.

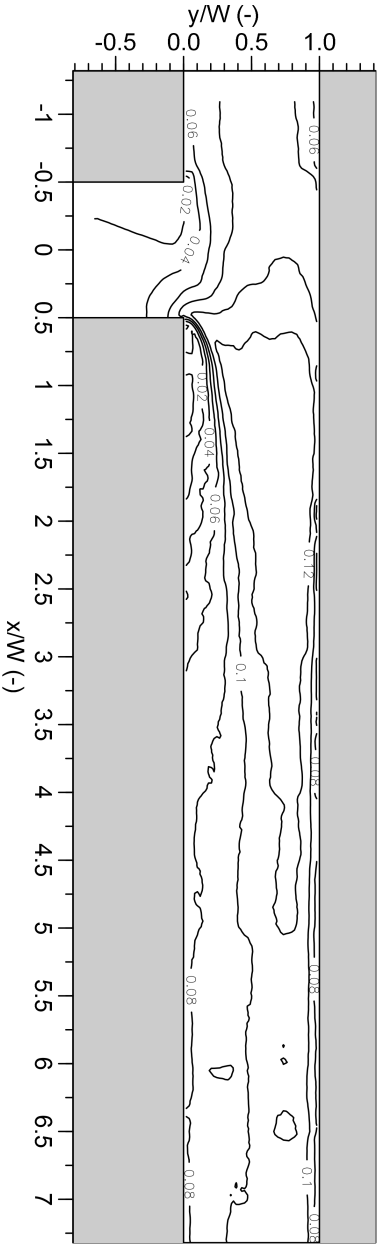

Figure 6.1: Contour plot of the experimentally obtained surface velocities in the large flume for q= 0.25.

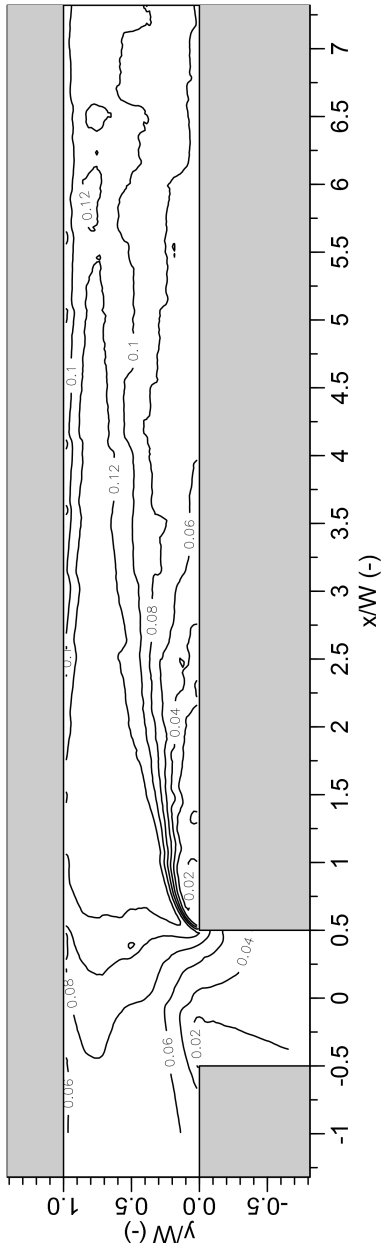

Figure 6.2: Contour plots of the experimentally obtained surface velocities in the large flume for q= 0.33.

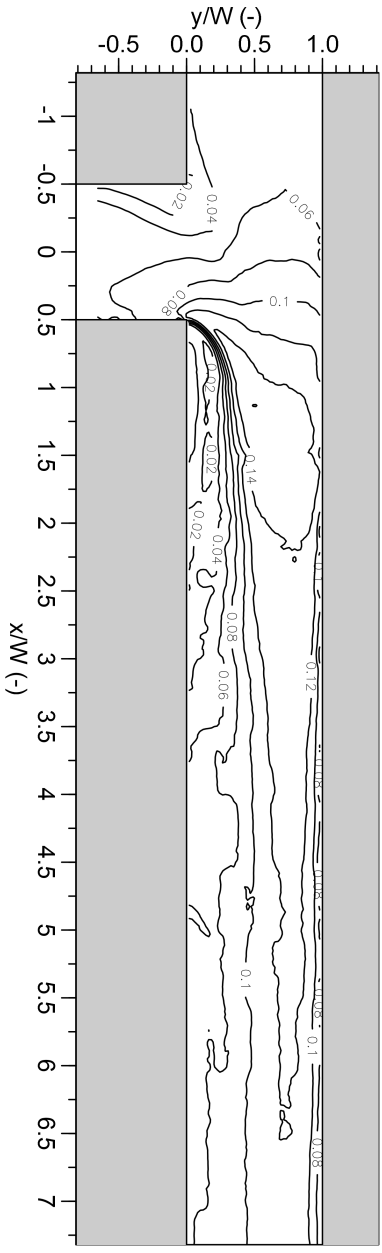

Figure 6.3: Contour plots of the experimentally obtained surface velocities in the large flume for q= 0.50.

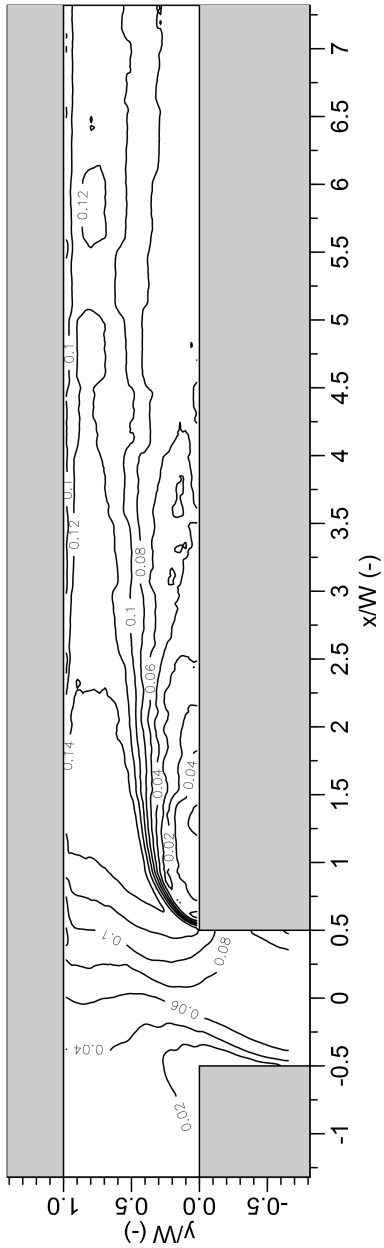

Figure 6.4: Contour plots of the experimentally obtained surface velocities in the large flume for q= 0.66.

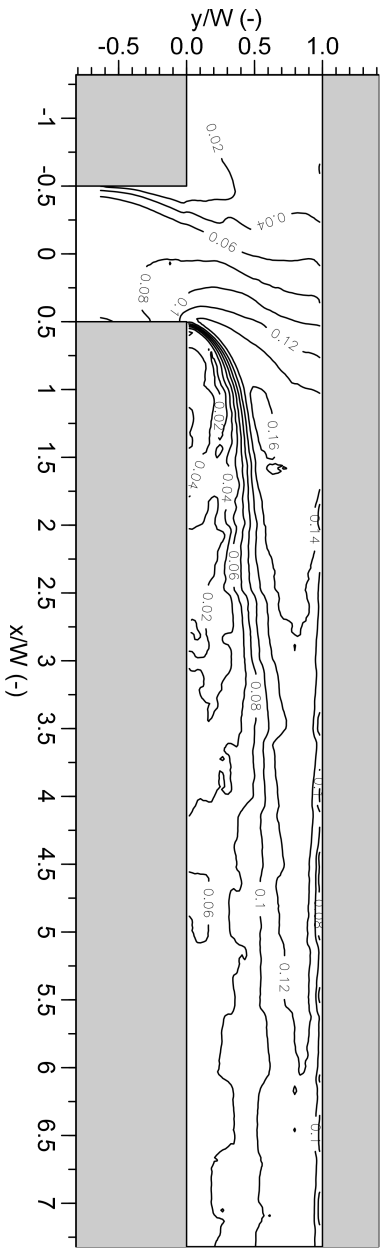

Figure 6.5: Contour plots of the experimentally obtained surface velocities in the large flume for q= 0.75.

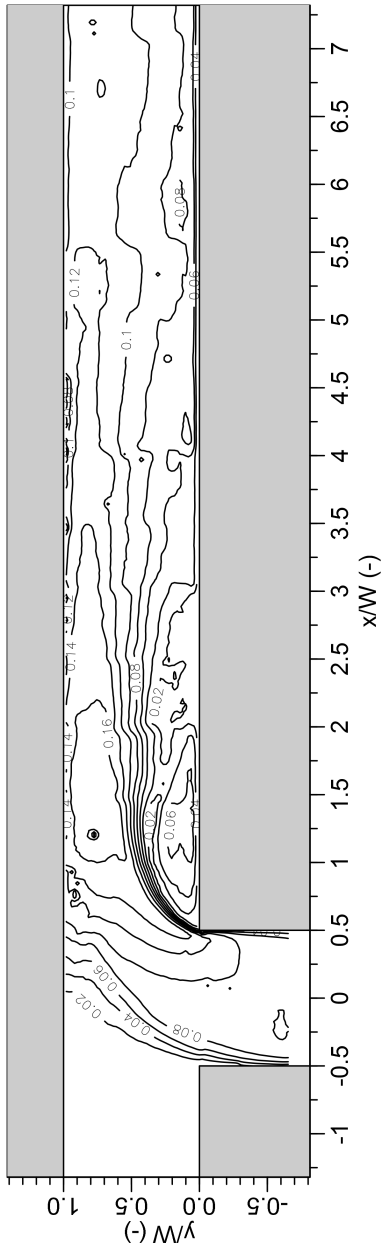

Figure 6.6: Contour plots of the experimentally obtained surface velocities in the large flume for q= 0.95.

Curriculum Vitae

Publications

Creëlle, S., Schindfessel, L. & De Mulder, T. (2017). "Modelling of the tributary momentum contribution to predict confluence head losses." *Journal of Hydraulic Research, 55(2)*. Taylor & Francis.

Creëlle, S., Roldán, R. , Herremans, A., Meire, D. , Buis, K. ,Meire, P. , Van Oyen , T., De Mulder , T. & Troch ,P. (2016). "Validation of large scale particle image velocimetry to acquire free-surface flow fields in vegetated rivers" *.Journal of Applied Water Engineering and Research* : Published online

Schindfessel, L. ,De Mulder, T. , **Creëlle, S.** & Schohl, G. A. (2016) "Closure to: On Analytical Formulae for Navigation Lock Filling-emptying and Overtravel by L. Schindfessel et al." Ed. Vladimir Nikora. *Journal of Hydraulic Research.* 54(2).

Schindfessel, L. , **Creëlle, S.** & De Mulder, T. (2016). "Dynamic Mode Decomposition Applied to the Shear Layer Flows in an Open Channel Confluence." In *River Flow 2016*, ed. George Constantinescu, Marcelo Garcia, and Dan Hanes, 1674–1682. Leiden : CRC press.

Creëlle, S., Schindfessel, L., Ramos, P. X. & De Mulder, T. (2016). "Experimental Investigation of the Flow Evolution in the Tributary of a 90° Open Channel Confluence." In *River Flow 2016*, ed. George Constantinescu, Marcelo Garcia, and Dan Hanes, 1667–1674. Leiden : CRC press.

Creëlle, S., Schindfessel, L. , De Mulder, T. (2016). "Discussion: Experimental Determination of Free Surface Levels at Open-channel Junctions." *Journal of Hydraulic Research,* 54 (2). Taylor & Francis.

Schindfessel, L. ,De Mulder, T. , **Creëlle, S.** & Schohl, G. A. (2015). "On Analytical Formulae for Navigation Lock Filling-emptying and Overtravel." Ed. Vladimir Nikora. *Journal of Hydraulic Research.* 53(1): 134–148.

Schindfessel, L. , **Creëlle**, **S.** & De Mulder, T. (2015). "Flow Patterns in an Open Channel Confluence with Increasingly Dominant Tributary Inflow." *Water* 7 (9): 4724–4751.

Creëlle, S., Schindfessel, L. & De Mulder, T. (2015). "Effect of Bed Roughness on the Mixing Layers in a 90° Asymmetrical Confluence." In *36th IAHR World Congress, Proceedings*. E-proceedings.

Schindfessel, L. , **Creëlle, S.** & De Mulder, T. (2015). "Influence of Cross-sectional Shape on Flow Patterns in an Open-channel Confluence." In *36th IAHR World Congress, Proceedings*. E-proceedings.

Visser, K. P., Ruys, B., Viaene, P., **Creëlle, S.**& De Mulder, T. (2015). " Assessment of the attraction flow in a fish passage." *5th IAHR International Junior Researcher and Engineer Workshop on Hydraulic Structures, Proceedings*.

Schindfessel, L. ,**Creëlle, S.**, Boelens, T. & De Mulder, T. (2014). "Flow Patterns in an Open Channel Confluence with a Small Ratio of Main Channel to Tributary Discharge." In *RIVER FLOW 2014*, ed. Anton Schleiss, Giovanni De Cesare, Mario Franca, and Michael Pfister, 989–996. London, UK: Taylor & Francis Group.

Creëlle, S., De Mulder, T., Schindfessel, L. & Van Oyen, T. (2014). "Influence of Hydraulic Resistance on Flow Features in an Open Channel Confluence." In *3rd Europe Congress, Proceedings*.

Roldán González, R., **Creëlle, S.**, Meire, D., Troch, P., Buis, K., Meire, P., & Van Oyen, T. (2014). "Validation of LSPIV to acquired 2D surface flow fields in vegetated lowland rivers". *11th International Conference on Hydroscience & Engineering, Proceedings* (pp. 1–6). (ICHE 2014).

Submitted:

Creëlle, S., Engelen, L., Ramos, Pedro, Schindfessel, L. & De Mulder, T. (submitted 2017) "Experimental study of the free surface slopes in the tributary branch of an asymmetrical 90◦ confluence". *Journal of Hydraulic Research*.(submitted)

Thomas, R. E. , Schindfessel, L. , McLelland, S. J. , **Creëlle, S.** &De Mulder, T. (submitted 2017). "Bias in mean velocities and noise in variances and covariances measured using a multistatic acoustic profiler: The Nortek Vectrino Profiler". *Measurement Science and Technology. (submitted)*

Schoelynck, J. , **Creëlle, S.** , Buis, K. , et. al. (submitted 2017). "What is a patch? Proposed protocols for patch identification and delineation". *Ecohydrology*. (submitted)

Creëlle, S., Engelen, L., Schindfessel, L. , Ramos, P. X. & De Mulder, T. (submitted 2017). "Experimental investigation of free surface gradients in a 90° angled asymmetrical open channel confluence". *Simhydro 2017*, Nice (accepted)

Schindfessel, L., **Creelle, S.**, De Mulder, T. (submitted 2017). "Dominant tributary flow in open channel confluences of different cross-sectional shapes". *Proc., 14th IWA/IAHR Int. Conf. on Urban Drainage*. (submitted)

Creëlle, S. , Mignot, E. , Schindfessel, L. De Mulder, T. (submitted 2016). "Experimental study of the free surface velocity field in an asymmetrical confluence". *EGU 2017* (accepted).

Schindfessel, L., **Creëlle, S.** & De Mulder & T. (submitted 2016). "How different cross-sectional shapes influence the separation zone of an open channel confluence." *Journal of Hydraulic Engineering*. ASCE. (accepted)

Varia

Coleman Award The publication Schindfessel et al. (2016) has received the Stephan E. Coleman Best Paper Award at the *Riverflow 2016* conference.

Research stay In February 2016 a one month stay at the *Laboratoire de Mécanique des Fluides et d' Acoustique (LMFA) - INSA - Lyon* was performed with prof. Mignot and Prof. Rivière.

Bibliography

Best, J. L. (1985). "Flow dynamics and sediment transport at river channel confluences.." Ph.D. thesis, Birkbeck (University of London), Birkbeck (University of London).

Best, J. L. and Reid, I. (1984). "Separation zone at open-channel junctions." *Journal of Hydraulic Engineering*, 110(11), 1588–1594.

Birjukova, O., Guillen, S., Alegria, F., and Cardoso, A. H. (2014). "Three dimensional flow field at confluent fixed-bed open channels." *River Flow 2014*, number EPFL-CONF-205193, Crc Press-Taylor & Francis Group, 1007–1014.

Biron, P., Best, J. L., and Roy, A. G. (1996). "Effects of bed discordance on flow dynamics at open channel confluences." *Journal of Hydraulic Engineering*, 122(12), 676–682.

Biron, P., Roy, A. G., Best, J. L., and Boyer, C. J. (1993). "Bed morphology and sedimentology at the confluence of unequal depth channels." *Geomorphology*, 8(2), 115–129.

Biron, P. M., Ramamurthy, A. S., and Han, S. (2004). "Three-dimensional numerical modeling of mixing at river confluences." *Journal of Hydraulic Engineering*, 130(3), 243–253.

Bradbrook, K., Lane, S., and Richards, K. (2000). "Numerical simulation of three-dimensional, time-averaged flow structure at river channel confluences." *Water Resources Research*, 36(9), 2731–2746.

Bradbrook, K., Lane, S., Richards, K., Biron, P., and Roy, A. (2001). "Role of bed discordance at asymmetrical river confluences." *Journal of Hydraulic Engineering*, 127(5), 351–368.

Constantinescu, G., Miyawaki, S., Rhoads, B., and Sukhodolov, A. (2016). "Influence of planform geometry and momentum ratio on thermal mixing at a stream confluence with a concordant bed." *Environ Fluid Mech*, 124(2), 1–29.

Constantinescu, G., Miyawaki, S., Rhoads, B., Sukhodolov, A., and Kirkil, G. (2011). "Structure of turbulent flow at a river confluence with momentum and velocity ratios close to 1: Insight provided by an eddy resolving numerical simulation." *Water Resour Res*, 47(5).

Creëlle, S., Roldan, R., Herremans, A., Meire, D., Buis, K., Meire, P., Oyen, T. V., Mulder, T. D., and Troch, P. (2016). "Validation of large-scale particle image velocimetry to acquire free-surface flow fields in vegetated rivers." *Journal of Applied Water Engineering and Research*, Published online(0), 1–12.

Creëlle, S., Schindfessel, L., and De Mulder, T. (2017). "Modelling of the tributary momentum contribution to predict confluence head losses." *Journal of Hydraulic Research*, 55(2), 175–189.

Creëlle, S., De Mulder, T., Schindfessel, L., and Van Oyen, T. (2014). "Influence of hydraulic resistance on flow features in an open channel confluence." *3rd IAHR Europe Congress.*

De Vriend, H. (1972). "Literatuuroverzicht bochtstroming." *Report no.*, TU Delft, Department of Hydraulic Engineering.

Dorđević, D. (2013). "Numerical study of 3D flow at right-angled confluences with and without upstream planform curvature." *Journal of Hydroinformatics*, 15(4), 1073–1088.

Dorđević, D. (2014). "Can a 3D-numerical models be a substitute to a physical model in estimating parameters of 1D-confluence models." *3rd IAHR-Europe Congress, Porto, Portugal*, 158–167.

Fujita, I. and Komura, S. (1989). "Visualization of the flow at a confluence." *Refined Flow Modelling and Turbulence Measurements. International Association of Hydraulic Research, Tokyo, Japan.*

Ghostine, R., Mose, R., Vazquez, J., Ghenaim, A., and Grégoire, C. (2010). "Two-dimensional simulation of subcritical flow at a combining junction: luxury or necessity?." *Journal of Hydraulic Engineering*, 136(10), 799–805.

Ghostine, R., Vazquez, J., Terfous, A., Mose, R., and Ghenaim, A. (2012). "Comparative study of 1D and 2D flow simulations at open-channel junctions." *Journal of Hydraulic Research*, 50(2), 164–170.

Gurram, S. K., Karki, K. S., and Hager, W. H. (1997). "Subcritical junction flow." *Journal of Hydraulic Engineering*, 123(5), 447–455.

Hager, W. H. (1989). "Transitional flow in channel junctions." *Journal of Hydraulic Engineering*, 115(2), 243–259.

Hsu, C.-C., Wu, F.-S., and Lee, W.-J. (1998). "Flow at 90° equal-width openchannel junction." *Journal of Hydraulic Engineering*, 124(2), 186–191.

Huang, J., Weber, L. J., and Lai, Y. G. (2002). "Three-dimensional numerical study of flows in open-channel junctions." *Journal of hydraulic engineering*, 128(3), 268–280.

Jaqaman, K., Loerke, D., Mettlen, M., Kuwata, H., Grinstein, S., Schmid, S. L., and Danuser, G. (2008). "Robust single-particle tracking in live-cell time-lapse sequences." *Nat methods*, 5(8), 695–702.

Kesserwani, G., Ghostine, R., Vazquez, J., Mosé, R., Abdallah, M., and Ghenaim, A. (2008). "Simulation of subcritical flow at open-channel junction." *Advances in Water Resources*, 31(2), 287–297.

Lane, S. N., Parsons, D. R., Best, J. L., Orfeo, O., Kostaschuk, R. A., and Hardy, R. J. (2008). "Causes of rapid mixing at a junction of two large rivers: Río Paraná and Río Paraguay,Argentina." *Journal of Geophysical Research: Earth Surface*, 113(F2), n/a–n/a F02024.

Laraque, A., Guyot, J. L., Filizola, N., et al. (2009). "Mixing processes in the Amazon River at the confluences of the Negro and Solimoes rivers, Encontro das Aguas, Manaus, Brazil." *Hydrological processes*, 23(22), 3131.

Lewis, Q. W. and Rhoads, B. L. (2015a). "Rates and patterns of thermal mixing at a small stream confluence under variable incoming flow conditions." *Hydrolog Process*, 29(20), 4442–4456.

Lewis, Q. W. and Rhoads, B. L. (2015b). "Resolving two-dimensional flow structure in rivers using large-scale particle image velocimetry: An example from a stream confluence." *Water Resour Res*, 51(10), 7977–7994.

Lin, J. and Soong, H. (1979). "Junction losses in open channel flows." *Water Resources Research*, 15(2), 414–418.

Mignot, E., Bonakdari, H., Knothe, P., Lipeme Kouyi, G., Bessette, A., Rivière, N., and Bertrand-Krajewski, J.-L. (2012). "Experiments and 3D simulations of flow structures in junctions and their influence on location of flowmeters." *Water Sci Technol*, 66(6), 1325–1332.

Mignot, E., Doppler, D., Riviere, N., Vinkovic, I., Gence, J.-N., and Simoens, S. (2014a). "Analysis of flow separation using a local frame axis: Application to the open-channel bifurcation." *Journal of Hydraulic Engineering*, 140(3), 280–290.

Mignot, E., Vinkovic, I., Doppler, D., and Riviere, N. (2014b). "Mixing layer in open-channel junction flows." *Environ Fluid Mech*, 14(5), 1027–1041.

Mockmore, C. (1944). "Flow around bends in stable channels." *Transactions of the American Society of Civil Engineers*, 109, 593–618.

Modi, P. N., Dandekar, M. M., and Ariel, P. D. (1981). "Conformal mapping for channel junction flow." *Journal of Hydraulic Engineering*, 107(12), 1713–1733.

Olesen, K. W. (1987). "Bed topography in shallow river bends." Ph.D. thesis, Delft University of Technology, Faculty of Civil Engineering, Delft University of Technology, Faculty of Civil Engineering.

Pandey, A. K. and Mishra, R. (2012). "Comparison of flow characteristics at rectangular and trapezoidal channel junctions." *Journal of Physics: Conference Series*, Vol. 364, IOP Publishing, 012141.

Pinto Coelho, M. M. L. (2015). "Experimental determination of free surface levels at open channel junctions." *Journal of Hydraulic Research*, 53(3), 394–399.

Ramamurthy, A. S., Carballada, L. B., and Tran, D. M. (1988). "Combining open channel flow at right angled junctions." *Journal of Hydraulic Engineering*, 114(12), 1449–1460.

Rhoads, B. L. and Kenworthy, S. T. (1995). "Flow structure at an asymmetrical stream confluence." *Geomorphology*, 11(4), 273–293.

Rhoads, B. L. and Kenworthy, S. T. (1998). "Time-averaged flow structure in the central region of a stream confluence." *Earth Surf Proc Land*, 23(2), 171–191.

Rhoads, B. L. and Sukhodolov, A. N. (2001). "Field investigation of three-dimensional flow structure at stream confluences: 1. thermal mixing and time-averaged velocities." *Water Resour Res*, 37(9), 2393–2410.

Rhoads, B. L. and Sukhodolov, A. N. (2008). "Lateral momentum flux and the spatial evolution of flow within a confluence mixing interface." *Water Resour Res*, 44(8).

Rodi, W., Constantinescu, G., and Stoesser, T. (2013). *Large-eddy simulation in hydraulics*. Crc Press.

Rozovskiĭ, I. L. (1957). *Flow of water in bends of open channels*. Academy of Sciences of the Ukrainian SSR.

Schindelin, J., Arganda-Carreras, I., Frise, E., Kaynig, V., Longair, M., Pietzsch, T., Preibisch, S., Rueden, C., Saalfeld, S., and Schmid, B. (2012). "Fiji an open-source platform for biological-image analysis." *Nat methods*, 9(7), 676–682.

Schindfessel, L. (2017). "Numerical and experimental modeling of the hydrodynamics of open channel confluences with dominant tributary inflow." Ph.D. thesis, Ghent University, Ghent University.

Schindfessel, L., Creëlle, S., Boelens, T., and De Mulder, T. (2014). "Flow patterns in an open channel confluence with a small ratio of main channel to tributary discharge." *Proc., Int. Conf. on Fluvial Hydraulics - River Flow 2014*, A. J. Schleiss, G. De Cesare, M. J. Franca, and M. Pfister, eds., Taylor & Francis Group, 989–996.

Schindfessel, L., Creëlle, S., and De Mulder, T. (2015a). "Flow patterns in an open channel confluence with increasingly dominant tributary inflow." *Water*, 7(9), 4724–4751.

Schindfessel, L., Creëlle, S., and De Mulder, T. (2015b). "Influence of cross-sectional shape on flow patterns in an open-channel confluence." *36th IAHR World Congress, Proceedings*, E-proceedings, 11, <http://app.iahr2015.info/>.

Schindfessel, L., Creëlle, S., and De Mulder, T. (2016). "Dynamic mode decomposition applied to the shear layer flows in an open channel confluence." *Proc., Int. Conf. on Fluvial Hydraulics - River Flow 2016*, G. Constantinescu, M. Garcia, and D. Hanes, eds., Taylor & Francis Group, 1674–1682.

Shabayek, S., Steffler, P., and Hicks, F. (2002). "Dynamic model for subcritical combining flows in channel junctions." *Journal of Hydraulic Engineering*, 128(9), 821–828.

Shakibainia, A., Tabatabai, M. R. M., and Zarrati, A. R. (2010). "Three-dimensional numerical study of flow structure in channel confluences." *Can J Civil Eng*, 37(5), 772–781.

Tancock, M. (2014). "The dynamics of upland river confluences." Ph.D. thesis, Durham University, Durham University.

Taylor, E. H. (1944). "Flow characteristics at rectangular open-channel junctions." *Trans. ASCE*, (107), 893–912.

Webber, N. B. and Greated, C. (1966). "An investigation of flow behaviour at the junction of rectangular channels.." *Proceedings of the Institution of Civil Engineers*, 34(3), 321–334.

Weber, L. J., Schumate, E. D., and Mawer, N. (2001). "Experiments on flow at a 90° open-channel junction." *Journal of Hydraulic Engineering*, 127(5), 340–350.

Zeng, C. and Li, C. (2010). "A hybrid RANS-LES model for combining flows in open-channel T-junctions." *Journal of Hydrodynamics, Ser. B*, 22(5), 154–159.

Zhang, T., XU, W.-l., and Chao, W. (2009). "Effect of discharge ratio on flow characteristics in 90° equal-width open-channel junction." *Journal of Hydrodynamics, Ser. B*, 21(4), 541–549.